ISSN 1408-7073

RMZ – MATERIALS AND GEOENVIRONMENT

PERIODICAL FOR MINING, METALLURGY AND GEOLOGY

RMZ – MATERIALI IN GEOOKOLJE

REVIJA ZA RUDARSTVO, METALURGIJO IN GEOLOGIJO

RMZ-M&G, Vol. 57, No. 3 pp. 295–440 (2010)

Ljubljana, September 2010

Historical Rewiev

More than 80 years have passed since in 1919 the University Ljubljana in Slovenia was founded. Technical fields were joint in the School of Engineering that included the Geologic and Mining Division while the Metallurgy Division was established in 1939 only. Today the Departments of Geology, Mining and Geotechnology, Materials and Metallurgy are part of the Faculty of Natural Sciences and Engineering, University of Ljubljana.

Before War II the members of the Mining Section together with the Association of Yugoslav Mining and Metallurgy Engineers began to publish the summaries of their research and studies in their technical periodical Rudarski zbornik (Mining Proceedings). Three volumes of Rudarski zbornik (1937, 1938 and 1939) were published. The War interrupted the publication and not untill 1952 the first number of the new journal Rudarsko-metalurški zbornik - RMZ (Mining and Metallurgy Quarterly) has been published by the Division of Mining and Metallurgy, University of Ljubljana. Later the journal has been regularly published quarterly by the Departments of Geology, Mining and Geotechnology, Materials and Metallurgy, and the Institute for Mining, Geotechnology and Environment.

On the meeting of the Advisory and the Editorial Board on May 22nd 1998 Rudarsko-metalurški zbornik has been renamed into "RMZ - Materials and Geoenvironment (RMZ -Materiali in Geookolje)" or shortly RMZ - M&G.

RMZ - M&G is managed by an international advisory and editorial board and is exchanged with other world-known periodicals. All the papers are reviewed by the corresponding professionals and experts.

RMZ - M&G is the only scientific and professional periodical in Slovenia, which is published in the same form nearly 50 years. It incorporates the scientific and professional topics in geology, mining, and geotechnology, in materials and in metallurgy.

The wide range of topics inside the geosciences are wellcome to be published in the RMZ -Materials and Geoenvironment. Research results in geology, hydrogeology, mining, geotechnology, materials, metallurgy, natural and antropogenic pollution of environment, biogeochemistry are proposed fields of work which the journal will handle. RMZ - M&G is co-issued and co-financed by the Faculty of Natural Sciences and Engineering Ljubljana, and the Institute for Mining, Geotechnology and Environment Ljubljana. In addition it is financially supported also by the Ministry of Higher Education, Science and Technology of Republic of Slovenia.

Editor in chief

Table of Contents – Kazalo

Original Scientific Papers – Izvirni znanstveni članki

Professional Papers – Strokovni članki

Short Papers – Kratki članki

Determination of precipitation sequence in Al-alloys using DSC method

Določitev sekvence izločanja v Al-zlitinah z DSC-metodo

Maja Vončina[1,*], Anton Smolej[1], Jožef Medved[1], Primož Mrvar[1] & Rok Barbič[2]

[1]University of Ljubljana, Faculty of Material Science and Engineering, Department of Materials and Metallurgy, Aškerčeva 12, 1000 Ljubljana, Slovenia
[2]Sistemska tehnika, d. d., Koroška cesta 14, 2390 Ravne na Koroškem, Slovenia

*Corresponding author. E-mail: maja.voncina@ntf.uni-lj.si

Received: January 19, 2010 **Accepted:** February 18, 2010

Abstract: The precipitation hardening of Al-5 % Cu based alloy was studied using the differential scanning calorimetry (DSC). Different transition phases were gained by the suitable temperature program. The microstructure was investigated using Scanning Electron Microscope (SEM) and Transmission Electron Microscope (TEM). The type of the precipitated phases was determined. The distribution, shape and size of investigated precipitates were determined.
The goal of this paper was to present how the DSC method can help to pursue the precipitation in to already known alloys or even to determine if the precipitation occurs in unknown alloys.

Izvleček: Izločevalno utrjevanje zlitine Al-5 % Cu je bilo preiskovano z diferenčno vrstično kalorimetrijo (DSC). Prehodne faze so bile v mikrostrukturi dosežene z uporabo ustreznega temperaturnega programa. Mikrostruktura je bila določena z uporabo vrstične elektronske mikroskopije (SEM) ter presevne elektronske mikroskopije (TEM). Tip, porazdelitev, oblika in velikost preiskovanih izločkov/prehodnih faz so bili tudi določeni.
Namen raziskav je bil predstaviti uporabnost DSC-metode pri spremljanju izločanja v poznanih ter nepoznanih zlitinah.

Key words: Al-Cu alloy, differential scanning calorimetry (DSC), precipi-

Original scientific paper

tation, precipitation kinetics, Scanning electron microscope (SEM), Transmission electron microscope (TEM)

Ključne besede: zlitina Al-Cu, diferenčna vrstična kalorimetrija (DSC), izločanje, kinetika izločanja, vrstična elektronska mikroskopija (SEM), presevni elektronski mikroskop (TEM)

Introduction

The formation and the distribution of various precipitates from supersaturated solid solution have a significant meaning of strengthening of many engineering alloys. The strength of the precipitation hardening alloy depends on the distribution, size and shape of the precipitated intermetallic phases. Regarding the type of the precipitates the corresponding hardness, tensile strength and ultimate tensile strength of the alloy is expected. [2]

Al-Cu alloys are widely known and discussed in many works. When the alloy of composition

Al-5 % Cu is heated to the temperature of about 530 °C the copper is dissolved in solid solution, and by quenching the alloy rapidly into water there is no time for any transformation to occur. The solid solution is then supersaturated with Cu and there is a driving force for precipitation of the equilibrium θ-phase, Al_2Cu.

The total precipitation process appears in followed sequence:

$$\alpha_0 \rightarrow \alpha_1 + \text{GP zone} \rightarrow \alpha_2 + \theta'' \rightarrow \alpha_3 + \theta' \rightarrow \alpha_4 + \theta$$

where α_0 is the original supersaturated solid solution, α_1 is the composition of the matrix in equilibrium with GP zones, α_2 the composition in equilibrium with θ'' phase, α_3 the composition in equilibrium with θ' phase and α_4 the composition in equilibrium with θ-Al_2Cu phase. [1, 2, 3, 4, 5, 10]

The total sequence of GP zones and transition phases takes place only if the alloy is aged under the solvus temperature of GP zones. For example, if ageing is carried out at temperature above the θ'' solvus but below θ' solvus, the first precipitate will be θ', heterogeneously nucleated on dislocations. If ageing is carried out above the θ' solvus, the only precipitate that is possible is θ which nucleates and grows at grain boundaries. Also, if an alloy containing GP zones is heated to above the GP zone solvus the zones will dissolve. [6, 7, 8]

Differential scanning calorimetry (DSC) is a popular technique which is often used to study the thermody-

namics and kinetics of phase changes in materials. It is particularly useful for precipitation reactions in light alloys used for structural applications, where successive solid-state reactions of precipitation and dissolution can be analysed at increasing temperatures. [15, 16] In this study the application of this method is presented.

Experimental

The Al-5 % Cu alloy with composition presented in Table 1 was prepared and melted in the induction furnace from aluminium (99.8 %) and refined copper (99.9 %). The alloy was cast into grey cast iron mould of a cylindrical shape of internal diameter 15 mm and length 123 mm. Furthermore the as-cast specimens were homogenized at temperature 520 °C for 8 h and then quenched in water to room temperature. The specimens for DSC analysis were turned to disks of 5 mm diameter and 3 mm high. The DSC analysis was performed in atmosphere of argon by the different temperature programs to reach different precipitates:

A. Heating up to 100 °C for 10 min with heating rate of 10 °C/min and cooling rate of 20 °C/min
B. Heating up to 200 °C for 10 min with heating rate of 10 °C/min and cooling rate of 20 °C/min
C. Heating up to 360 °C for 10 min with heating rate of 10 °C/min and cooling rate of 20 °C/min
D. Heating up to 500 °C for 10 min with heating rate of 10 °C/min and cooling rate of 20 °C/min

Whole experimental process is presented in Figure1.

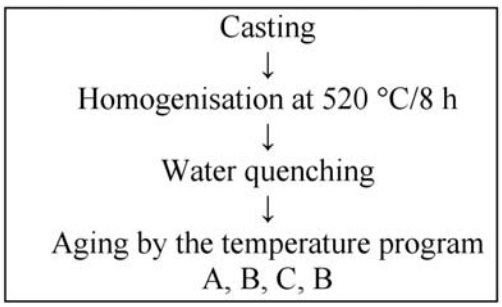

Figure 1. Schematically presentation of experimental process

The DSC instrument (Jupiter 449c of NETZSCH) was previously calibrated and the basic curves for individual temperature program were recorded. Furthermore DSC curves were plotted, temperatures of the precipitation were marked and the energies of a various precipitates were determined. In addition the specimens were observed with the scanning electron microscope (SEM) SIRIUM 400nc of a Fey Company equipped with the EDS analyzer INCA 350 and with transmission electron microscope JEM-2000FX. The shape, sizes and distribution of the precipitates were determined.

Table 1. Chemical composition of investigated alloy Al-5 % Cu

Element	**Si**	**Fe**	**Cu**	**Mn**	**Mg**	**Zn**	**Ti**	**Al**
mass fraction (*w*/%)	0.028	0.043	4.730	0.0012	0.004	0.001	0.003	Rest

Table 2. Temperature of the precipitation of different precipitates at two heating rates

Precipitate/transition phase	Heating rate 10 °C/min	Heating rate 20 °C/min
GP zone	58.0 °C	60.5 °C
Θ″	87.6 °C	106.8 °C
Θ’	210 °C	219.4 °C
Θ-Al_2Cu	419.1 °C	421.7 °C

Results and discussion

The first experiment was made to compare the influence of the heating/cooling rate on the precipitation intensity (temperature and precipitation energy/enthalpy). DSC curves are presented in Figures 2 and 3. Regarding the cooling rate it can be observed that with the increasing heating rate the starting temperature for the precipitation of various precipitates (precipitation sequence) increases (Table 2) as it was described by Gaber A. et. al. [13,14]

After the temperature and the precipitation energy of transition phases and Al_2Cu precipitates were determined, the purpose was also to prove which transition phase (precipitate) actually occurred. The DSC experiment was carried out with a suitable temperature program (A, B, C and D) to reach the desired precipitates in the microstructure.

Peak A on Figure 4 belongs to the formation of GP zones. The activation energy for the formation of GP zones at heating rate 10 °C/min was 0.392 J/g. At peak B the transformation from GP zone to the θ″ zone took place. This peak is an endothermic peak where enthalpy of –5.126 J/g is used. Precipitate θ’ usually nucleate at dislocations, [2, 3] what takes course in section C with the enthalpy of 13.97 J/g. Incoherent equilibrium θ phase of a approximate composition Al_2Cu precipitates in section D presented on Figure 4. For this transformation 4.029 J/g energy was relaxed.

The gained specimens were analysed using Scanning electron microscope and Transmission electron microscope (Figures 5–8). On Figure 5 bright-field TEM micrographs of specimen analysed by temperature program A is presented. Regarding the final heating temperature it can be expected, that these are GP zones that precipitated from supersatu-

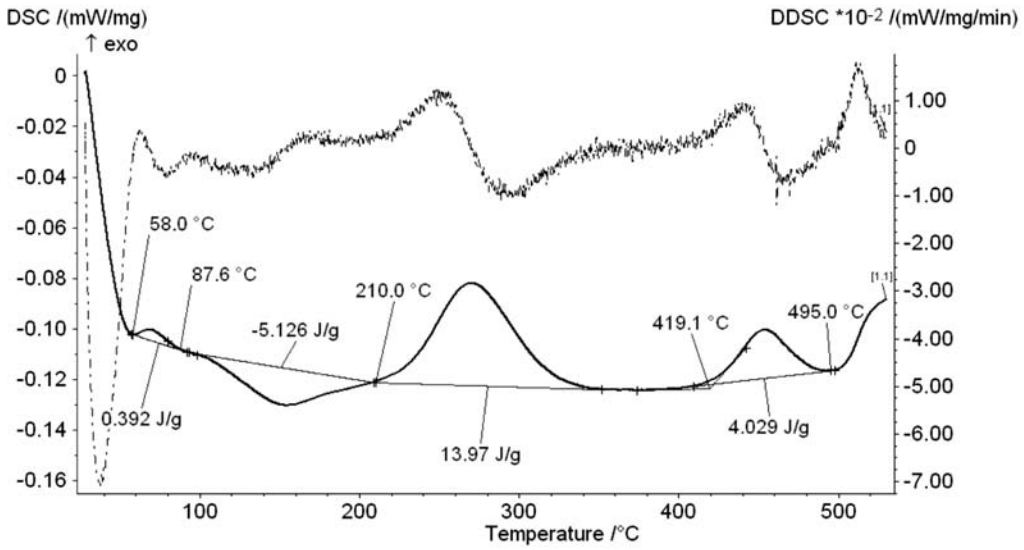

Figure 2. DSC curve obtained at heating and cooling rate 10 °C/min up to 530 °C for casted and homogenized Al-5 % Cu alloy

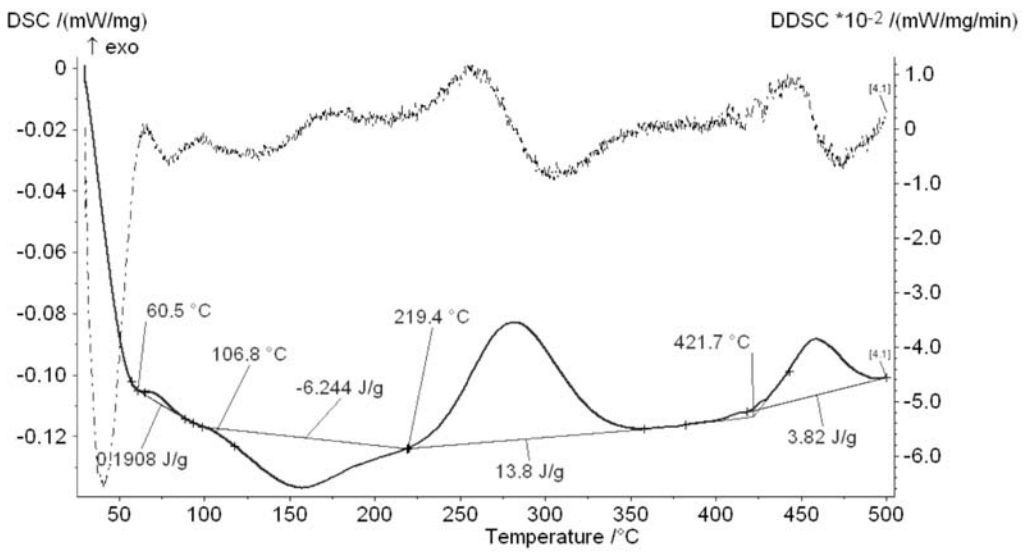

Figure 3. DSC curve obtained at heating and cooling rate 20 °C/min up to 500 °C for casted and homogenized Al-5 % Cu alloy

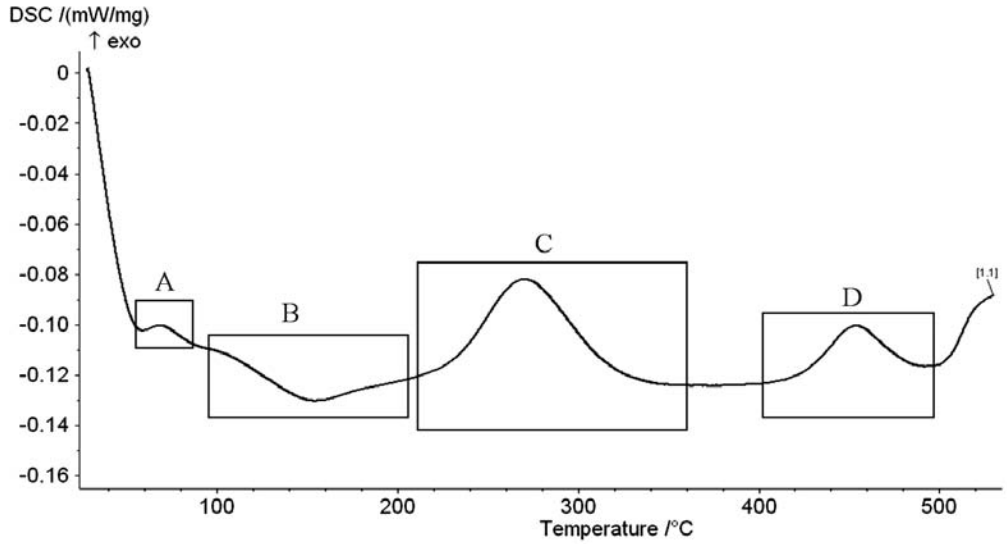

Figure 4. DSC curve analysed by the temperature program that provides desirable precipitate in the microstructure.

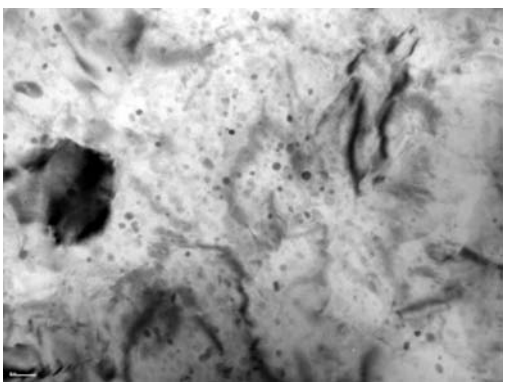

Figure 5. TEM micrographs of Al-5 % Cu specimen prepared by temperature program A (GP zone).

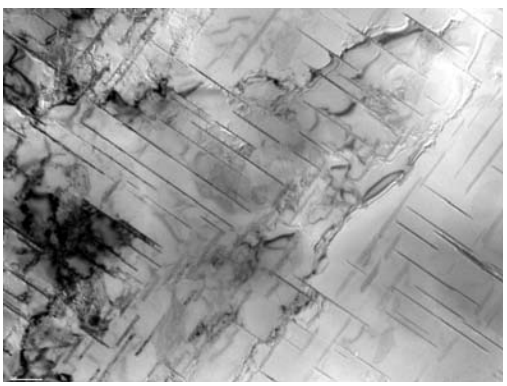

Figure 6. TEM micrographs of Al-5 % Cu specimen prepared by temperature program B (θ″ precipitates)

rated solid solution. Phases could not be analysed with EDS because the electron beam is too wide and the phases are too small (the error would be too large).

Figure 6 presents microstructure of a specimen analysed by DSC temperature program B. At heating to temperature 200 °C at most fully and semi-coherent

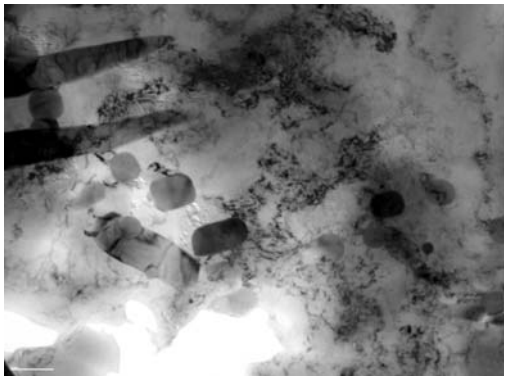

Figure 7. TEM micrograph of Al-5 % Cu specimen prepared by temperature program C (θ' precipitates)

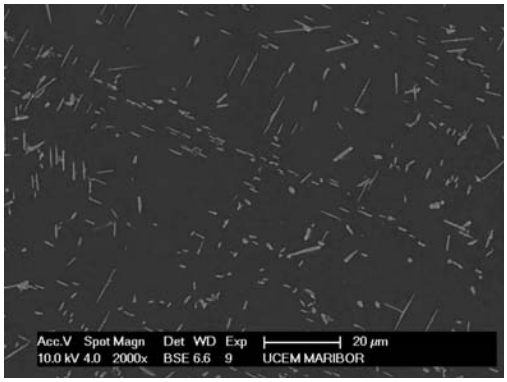

Figure 8. SEM microstructure of Al-5 % Cu specimen prepared by temperature program D (θ-Al_2Cu precipitates)

plate-like θ″ precipitates precipitate in the matrix beside GP zone. These precipitates also could not be analysed with EDS because of their small size however the length was measured and was 500–1500 μm and the tightness was 30–35 nm. TEM analysis confirmed two variants of precipitates, first θ″ precipitate which plane (001) is parallel to plane (100) of aluminium and second θ' precipitate which plane (100) is parallel with (100) plane of aluminium (Figure 6). The orientation of the specimens is also evident from Figure 6.

With heating to temperature 360 °C with heating rate of 10 °C/min and cooling rate of 20 °C/min (C) the specimen presented in Figure 7 was tested. Here θ' precipitates can be observed that grew bigger. It was found that they had approximate composition of stable Al_2Cu. On Figure 8 microstructure of specimen analysed by temperature program D is presented. Regarding the final heating temperature it can be expected to find equilibrium θ-Al_2Cu phase. EDS analyzer showed that it was combine from mole fractions 35–40 % of copper and 60–65 % of aluminium what corresponds to a composition of Al_2Cu phase. [7, 9, 10]

Conclusion

In this study the temperature of precipitation sequence and the precipitation energy was investigated. It can be seen that the DSC method is very useful when the precipitation or even the course of the precipitation in the alloy is to determine.

In this case the temperature of formation of transition phases and the influ-

ence of heating rate ware determined with the DSC analysis. It was shown that the precipitation temperature shift to a higher temperature when heating rate increases. At higher heating rate 20 °C/min the precipitation energies are a little smaller than at heating rate of 10 °C/min because of a shorter precipitation time. For the formation of GP zones, Θ' and Θ-Al_2Cu the exothermic peak occurs on heating DSC curve. However for the formation Θ″ precipitate the endothermic peak appears on the heating DSC curve. The aim was also to prove which transition phase or precipitate precipitated from supersaturated solid solution at defined temperature. TEM micrographs and convergent beam electron diffraction confirmed the sequence of the precipitation.

Differential scanning calorimetry (DSC) is a popular technique which is often used to study the thermodynamics and kinetics of phase changes in materials. It is particularly useful for precipitation reactions in light alloys, where successive solid-state reactions of precipitation and dissolution can be analysed at increasing temperatures.

Acknowledgements

The authors would like to thank to dr. Franc Zupanič, University of Maribor, Faculty of Mechanical Engineering and dr. Goran Dražić, Jožef Stefan Institute, Ljubljana, for technical assistance.

References

[1] Teixeira, J., Da Costa, Cram, D. G., Bourgeois, L., Bastow, T. J., Hill, A. J., Hutchinson, C. R. (2008): On the strengthening of aluminum alloys containing shear-resistant plate-shaped precipitates. *Acta Materialia*, Vol. 56, 6109–6122.

[2] Porter, D. A. (1992): Phase Transformation in Metals and Alloys; Chapman & Hall, 1992.

[3] Mondolfo, L. F. (1976): Aluminium Alloys: Structure and Properties; Butter worths, 1976, London.

[4] Ando, Y., MIHAMA, K., Takahashi, T., Kojima, Y. (1974): Growth of Guinier-Preston Zones and the θ"-phase in Al-4% Cu Alloys. *Journal o Crystal Groeth*, Vol. 24–25, 581–584.

[5] Altenpohl, D. (1965): Aluminium und Alminiumlegierungen, Reine und angewandte Metallkunde in Einzeldarstellungen, Springer-Verlag, Berlin/Göttingen/Heidelberg/New York, 1965.

[6] Karlik, M., Bigot, A., Jouffrey, B., Auger, P., Belliot, S., Hrem (2004): FIN and tomographic atom probe investigation of Guinier-Preston zones in an Al-1.54 at.% Cu alloy., *Ultramicroscopy*, Vol. 98, 219–230.

[7] Maio, W. F., Laughlin, D. E. (1999):

Precipitation Hardening in Aluminium Alloy 6022. *Scripta Materialia*, Vol. 40/7, 873–878.

[8] Gupta, A. K., Lloyd, D. J., Court, S. A. (2001): Precipitation hardening in Al-Mg-Si alloys with and without excess Si. *Material Science and Engineering*, A316, 11–17.

[9] Ovono, D., Guillot, I., Massinon, D. (2006): The microstructure and precipitation kinetics of a cast aluminium alloy. *Scripta Materialia*, Vol. 55, 259–262.

[10] Wang, S. Q., Schneider, M., Ye, H. Q., Gottstein, G. (2004): First-priciples study of the formation of Guinier-Preston zones in Al-Cu alloys. *Scripta Materialia*, Vol. 51, 665–669.

[11] Boyd, J. D., Nicholson, R. B. (1971): The Coarsening Behaviour of θ" and θ' Precipitates in Two Al-Cu Alloys. *Acta Metallurgica*, Vol. 19, 1379–1391.

[12] Han, J. (2005): Processing, microstructure evolution and properties of nanoscale aluminium alloys. Doctors dissertation, University of Cincinnati, July 2005.

[13] Gaber, A., Mossad Ali, A., Matsuda, K., Kawabata, T., Yamazaki, T., Ikeno, S. (2007): Study of the developed precipitates in Al–0.63Mg–0.37Si–0.5Cu (wt.%) alloy by using DSC and TEM techniques. *Journal of Alloys and Compounds*, Vol. 432, 149–155.

[14] Starink, M. J. & Zahra, A. M. (1998): β' AND β PRECIPITATION IN AN Al-Mg ALLOY STUDIED BY DSC AND TEM. *Acta mater*, Vol. 46/10, 3381–3397.

[15] Hersent, E., Driver, J. H., Piot, D. (2009): Modelling differential scanning calorimetry curves of precipitation in Al–Cu–Mg, S*cripta Materialia*.

[16] Son, S. K., Takeda, M., Mitome, M., Bando, Y., Endo, T. (2005): Precipitation behavior of an Al–Cu alloy during isothermal aging at low temperatures. *Materials Letters*, Vol. 59, 629–632.

Oxidation of dissolved iron in platinum

Oksidacija železa, raztopljenega v platini

Grega Klančnik,[1,]*, Jožef Medved[1]

[1]University of Ljubljana, Faculty of Natural Sciences and Engineering, Department of Materials and Metallurgy, Aškerčeva cesta 12, SI-1000 Ljubljana, Slovenia

*Corresponding author. E-mail: grega.klancnik@omm.ntf.uni-lj.si

Received: February 10, 2010 **Accepted:** July 20, 2010

Abstract: Platinum is used as material for high temperature applications as sensors and heating elements. For example, the most vital parts of the simultaneous thermal analysis device (STA) are commonly made of platinum: thermocouples and platinum sample holder. STA is a combination of two thermal analysis techniques: thermogravimetry (TG) and differential scanning calorimetry (DSC). An uncontaminated holder is needed in TG analysis by which mass change of examined sample is determined as function of temperature and time. When holder is exposed to various steels (especially low alloyed steels) at higher temperatures there exists some risk of contamination of measuring parts (made of platinum) with elements, especially if measurements take place without a proper protection of the sample holder (cover on crucible, protective atmosphere etc.). When a pure melt of elements like iron is in contact with platinum sample holder, local contamination occurs. Dissolved iron can oxidize in the platinum holder. Heat transfer from heating elements to platinum and further to examined sample is changed. Contamination also affects obtained termogravimetric curves.

Izvleček: Platina se večinoma uporablja v visokotemperaturnih aplikacijah, v senzorjih ali grelnih elementih. Večina vitalnih delov simultane termične analize (STA) je narejena iz platine: termoelementi in nosilec. STA je kombinacija dveh termičnih analiz: termogravimetrije (TG) in diferenčne vrstične kalorimetrije (DSC). Za ugotavljanje sprememb mase preiskovanega vzorca uporabljamo TG-analizo v odvisnosti od časa in temperature. Meritve se morajo izvajati s

Original scientific paper

čistim nosilcem. Izpostavljanje nosilca različnim jeklom (predvsem malolegiranim) pri višjih temperaturah lahko povzroči kontaminacijo merilnih (platinastih) delov, kadar zaščita platinastega nosilca ni ustrezna (pokrivanje lončkov, zaščitna atmosfera itd.). Taljenje železa v platinastem nosilcu povzroči lokalno kontaminacijo. Raztopljeno železo se lahko v platinskem nosilcu oksidira ter spremeni prenos toplote iz grelnih elementov na platino, obenem pa ima kontaminacija tudi vpliv na meritve termogravimetričnih krivulj.

Key words: thermodynamics, oxidation, platinum
Ključne besede: termodinamika, oksidacija, platina

INTRODUCTION

Knowing the activity of iron in the Pt-Fe binary system the calculation of equilibrium partial pressure of oxygen for metal oxides can be done. Calculation was done with the known data of iron activity a_{Fe} in the Fe-Pt binary phase system. Some data can be found in references (Gudmondsson and Holloway).[1] In this paper thermodynamic calculations were performed using a_{Fe}, at different temperatures, with the TCW4 software. Many authors were studying oxidation (of iron) and the importance of mass gain for protection of material itself by adding modificators.[2, 3] This paper deals with analysis of mass reduction of oxides due to oxide reduction process.

Phase diagram in Figure 1 represents the Fe-Pt binary phase diagram. If contamination of platinum holder with iron is rather high, some intermediate phases can be formed (Pt_3Fe, PtFe and Fe_3Pt). When mole fraction of iron is higher than $x_{Fe} = 0.2$, the liquidus temperatures are below 1550 °C which usually represents the maximum temperature for examination of steels with the STA device. Result is possible presence of iron in platinum sample holder.

THERMODYNAMIC CALCULATIONS

Thermodynamics of iron oxidation

Pourbaix diagrams are known as the high temperature oxidation temperature diagrams or the predominance diagrams with multivariate equilibria between elements and their oxides or between two oxides as a function of equilibrium partial pressure of oxygen and the temperature of system.[4] This diagram enables to study behavior of multivariate oxide system, in our case system of iron oxides (wüstite, hematite, magnetite) that are formed on contaminated platinum. Equilibrium of each reaction (oxidation) is determined by:

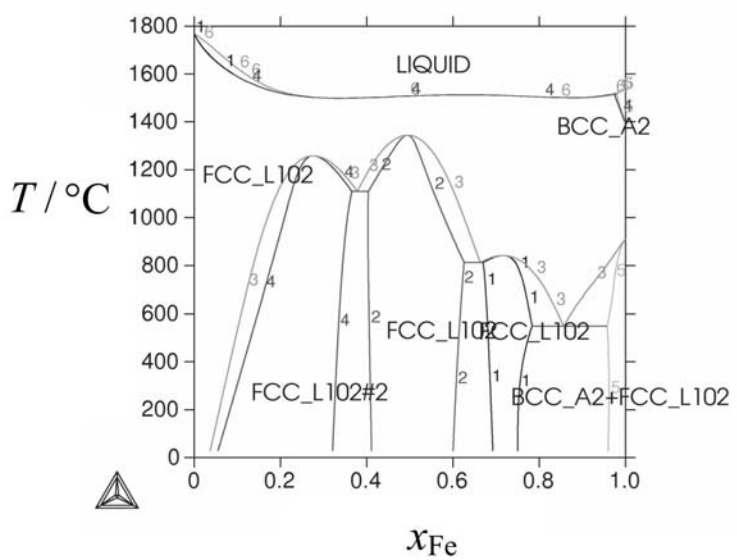

Figure 1. Binary phase diagram Fe-Pt

$$\Delta G^0 = -RT \ln K \quad (1)$$

where is:
R – gas constant (8.3144 J/mol K),
T – temperature (K),
K – equilibrium constant.

For the reaction of oxidation:

$$x\mathrm{R} + \mathrm{O}_2 = y\mathrm{P} \quad (2)$$

where:
R – reactant and
P – product,
equation 1 can be rewritten as:

$$\Delta G^0 = -RT \ln \frac{a_P^Y}{a_R^X} \frac{1}{p_{0_2}} \quad (3)$$

where are:
a_P^y, a_R^x – activity of product and reactant. Further:

$$\Delta G^0 = \Delta H^0 - T \cdot \Delta S^0 = -RT \ln f + RT \ln p_{0_2} \quad (4)$$

where $f = a_P^y / a_R^x$ is the predominance ratio. When the ratio is $f >> 1$ product component in the reaction predominates over equilibrium, if $f << 1$, reactant predominates. According to this information, eq. 4 can be rewritten:

$$\ln p_{0_2} = \frac{\Delta H^0}{RT} + \ln f - \frac{\Delta S^0}{R} \quad (5)$$

In our case the predominance ratio is 1 and the value of ln f is therefore 0. In this case the Pourbaix diagram is constructed with equal activity coefficients of product and reactant. This means that Pourbaix diagram is constructed only for oxidation of pure and un-dissolved iron. The construction of oxidation predominance diagram is done when all the possible reactions are col-

lected with known values of enthalpies and entropies of formation, ΔH^0 and ΔS^0 (BARIN & KNACKE[5]). In this case it can be assumed that ΔH^0 and ΔS^0 are temperature independent. Calculations of these two values are based on the following oxidation reaction:

$$x\mathrm{M_aO_b} + \mathrm{O_2} = y\mathrm{M_uO_v} \quad (6)$$

The enthalpy of formation ΔH^0 is calculated by applying the following equations:

$$\Delta H_j^0 = y \cdot \Delta H_{f,M_UO_V{}^0} - x \cdot \Delta H_{f,M_aO_b{}^0} \quad (7)$$

$$\Delta S_j^0 = y \cdot \Delta S_{f,M_UO_V{}^0} - x \cdot \Delta S_{f,M_aO_b{}^0} \quad (8)$$

Knowing data of enthalpies and entropies of formation based on the reaction of oxidation, calculation of p_{0_2} can be performed for the possible reactions of oxidation:

$$2Fe + O_2 \rightarrow 2FeO; \qquad K = \frac{a_{FeO}^2}{a_{Fe}^2 \cdot p_{o_2}} \quad (9)$$

$$\frac{4}{3}Fe + O_2 \rightarrow \frac{2}{3}Fe_2O_3; \quad K = \frac{a_{Fe_2O_3}^{2/3}}{a_{Fe}^{4/3} \cdot p_{o_2}} \quad (10)$$

$$\frac{3}{2}Fe + O_2 \rightarrow \frac{1}{2}Fe_3O_4; \quad K = \frac{a_{Fe_3O_4}^{1/2}}{a_{Fe}^{3/2} \cdot p_{o_2}} \quad (11)$$

$$4FeO + O_2 \rightarrow 2Fe_2O_3; \quad K = \frac{a_{Fe_2O_3}^2}{a_{FeO}^4 \cdot p_{0_2}} \quad (12)$$

$$6FeO + O_2 \rightarrow 2Fe_3O_4; \quad K = \frac{a_{Fe_3O_4}^2}{a_{FeO}^6 p_{0_2}} \quad (13)$$

where:
a_{Fe} – activity of iron,
$a_{\mathrm{MuOv}} = 1$ – activity of oxide,
p_{0_2} – partial pressure of oxygen.

The oxidation affinity in the platinum – iron system

Platinum may be treated as an inert component. Active component in this case is only the dissolved iron in platinum. For calculation of partial pressure of oxygen for formation of oxides from dissolved iron, the activity coefficients are needed (lower values than 1). In this case the predominance ratio f is no longer 1 and it depends on real values of activities of dissolved iron. With the known value of $\Delta G^0{}_T$ for separate reaction of oxidation, the equilibrium constant of corresponding oxidation condition can be calculated from the eq.1:

$$K = e^{-(\Delta G^0/RT)} = \frac{a_{M_uO_v}^Y}{a_{Fe}^X \cdot p_{0_2}} \quad (14)$$

Knowing activities the calculation of the partial pressure needed for formation of an oxide can be performed for different temperatures and concentrations of iron dissolved in platinum. The affinity (further A) for oxidation of dissolved iron is calculated from the chemical potential of oxygen which depends on partial pressure of the system (furnace):

$$\mu_{0_2} = \mu_{0_2}^0 + RT \ln a_{0_2} \quad (15)$$

where:
μ_{0_2} – chemical potential of oxygen (depends on partial pressure in the system),
μ_{0_2} – standard chemical potential of oxygen.

If the reference state is 1 bar the activity coefficient of oxygen is equal to the partial pressure $a_{0_2} = p_{0_2}$. The affinity is calculated from the difference of Gibbs free energies between equilibrium partial pressure of oxygen and the pressure in furnace (eq. 16). Negative affinity (A) indicates possible existence of an oxide. Positive affinity represents decomposition of oxide at existent partial pressure of oxygen in the system.

$$A = RT\ln(p_{0_2})_{eq} - RT\ln(p_{o_2}) = RT\ln\frac{(p_{o_2})_{eq}}{(p_{o_2})} \quad (16)$$

Experimental

Measurements of characteristic temperatures were performed with iron 99.8 % pure. The STA 449-C device of Netzsch Company was applied. The maximal temperature reached was 1550 °C at heating rate of 10 K/min, followed by 15 min of holding at 1480 °C. An empty crucible was used as reference. Crucible was made of highly pure Al_2O_3. After experiment, both crucibles (for sample and reference) were removed from the platinum sample holder, where contamination was detected. Another TG measurement was done without sample or crucibles. Heating rate was also 10 K/min under inert argon protective atmosphere was applied.

In the case when highly pure argon atmosphere was applied and content of oxygen was known, partial pressure of oxygen was determined to be $p_{o2} = 10^{-6}$ bar at the total pressure of $p = 1$ bar inside the furnace.[6]

The effect of contamination of platinum with iron / iron oxide visible on TG curve can be calculated if thermodynamic properties (activities) of the platinum – iron binary system are known. In order to determine the activity of iron in the platinum-iron system a Thermo Calc for Windows (TCW4) with the TC binary solutions database V1 was applied.

Thermodynamic calculation to construct Pourbaix high temperature diagram for un-dissolved iron and its oxides was performed by using equations 9–13. The oxygen affinities for dissolved iron in platinum were calculated by eq. 16 using equations 9–11.

Results and disscusion

DSC heating curve, Figure 2, of iron revealed that characteristic tempera-

tures slightly differ from the values listed in reference[1]. Additional peaks that appeared represented impurities in iron wire. TG heating curve shows drastic drop at the holding temperature 1480 °C which takes place also by further heating to temperature 1550 °C. Contamination of the platinum surface with iron is presented in Figure 3. Because of drastic mass decrease determined by TG curve it was expected that vapors could have contaminated the sample platinum holder. By analyzing TG curve and by removing the crucibles a local contamination was revealed (Figure 3).

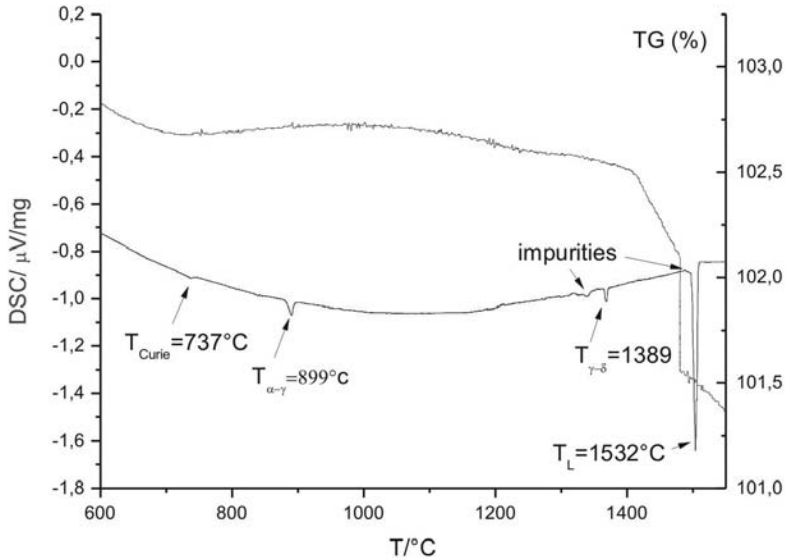

Figure 2. DSC and TG heating curves for iron sample

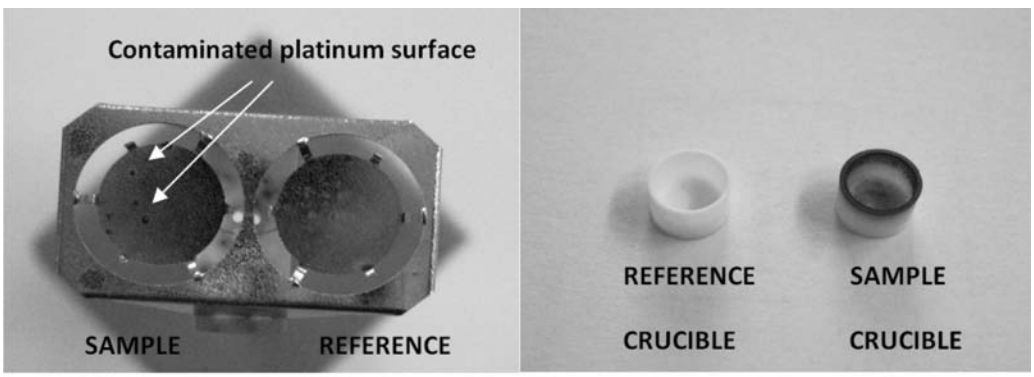

Figure 3. Contaminated platinum sample holder (a), Al_2O_3 crucible (b)

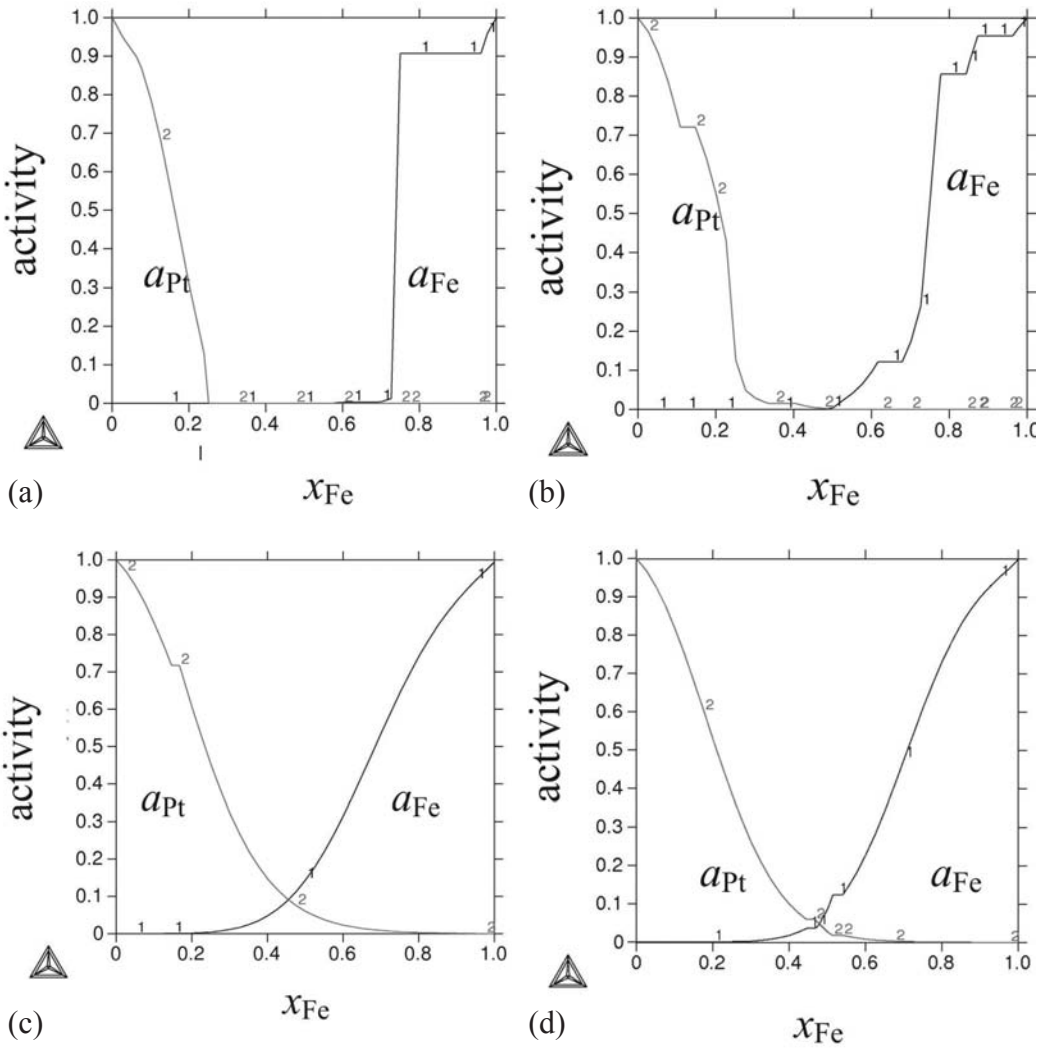

Figure 4. Activity of iron in the Pt-Fe binary system: at 50 °C (a), 600 °C (b), 1300 °C (c) and 1550 °C (d)

Values of iron activity coefficients vary with composition and temperature (Figure 4). The activity of iron in the temperature range from 50 °C to 1550 °C is mostly lower than that of ideal solution where ($a_{Fe} = x_{Fe}$), and typical for systems with intermediate phases.

Thermodynamic calculations indicate formation of oxides in the temperature range between 700 °C and 4000 °C, based on possible reactions of oxidation, Figure 5. Figure 5 shows that most probable reaction in oxidative atmosphere will take place by oxidation

of iron to hematite at lower temperatures (≈800 °C) and further oxidation of wüstite to hematite at higher temperatures (>≈800 °C). Decomposition of the formed oxide to elementary iron is not possible at the system's partial pressure of oxygen (p_{O2} = 10^{-6} bar) and the maximum temperature 1550 °C. At least 1700 °C is needed for decomposition of the high temperature oxide FeO. At the temperature around 1700 °C, FeO decomposes to elementary iron and oxygen that is swept off with argon purge gas. At higher temperatures (>1700 °C), the less stable reaction in this system is further oxidation of FeO to the higher oxide of Fe_2O_3. Temperature of decomposition will be different if iron is dissolved in platinum.

Partial pressure of oxygen that is needed for oxidation (colored regions) of dissolved iron in platinum is presented in Figure 6. The diagrams show that much lower partial (dissociation) pressures of oxygen in the system are needed for decomposition of formed oxides in pure iron and in the region of higher iron contamination. From Figure 6, the partial pressure of oxygen in the furnace, p_{O2} = 10^{-6} bar, is already low enough to achieve decomposition of formed iron oxide in the regions with small iron molar content. For complete decomposition of formed oxides in all concentration regions, at rather low temperatures, proper vacuum system should be used. The use of vacuum during heating has

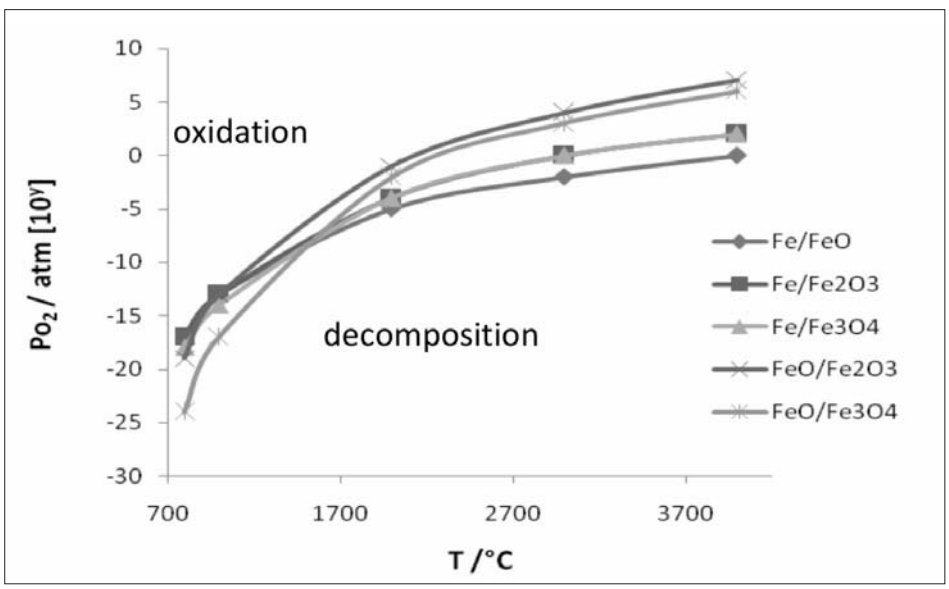

Figure 5. Pourbaix high temperature diagram for un-dissolved iron and its oxide

also effect on evaporation of other elements in the investigated samples and as consequence possible contamination with new elements and formation of new and more complex oxides with the existing one. Nevertheless, when system's temperature is increased high enough thermodynamically calculated partial pressure of oxygen in the Pt-Fe system shows that all the oxides are less stable in some point and eventually they decompose.

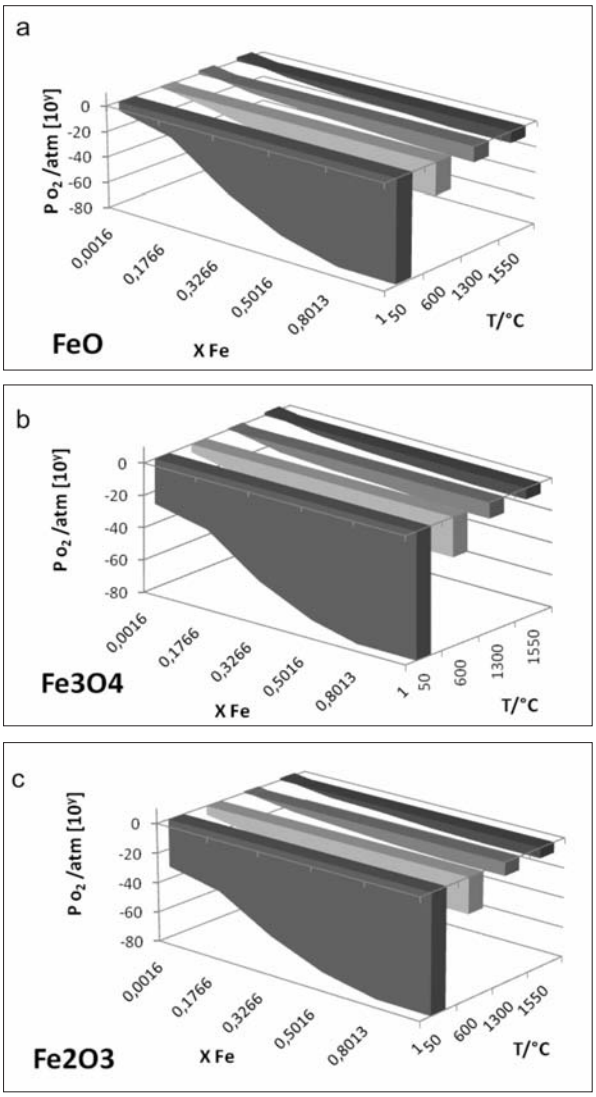

Figure 6. Pourbaix high temperature diagram for the Pt-Fe binary system at different temperatures: FeO (a), Fe_3O_4 (b) and Fe_2O_3 (c)

Oxygen affinities for dissolved iron were calculated with the eq. 16 and the results are presented in Figure 7 for four different temperatures of the system. At 50 °C, the calculated oxygen affinities are negative for all the three oxides formed according to eqs. 9, 10 and 11 and as that all thermodynamicly possible. Both formed oxides, Fe_2O_3 and Fe_3O_4 are thermodynamicly more possible as FeO. With increased system's temperature to 600 °C, Figure 7 b, the first dissociation can appear if FeO is present. From Figure 7 b, affinities of Fe_2O_3 is more negative than the affinity of Fe_3O_4 and FeO in regions of small iron content ($x_{Fe} < 0.05$). That means that the Fe_2O_3 oxide is most probable and will began to decompose at 600 °C. Neverthless, first mass decrease is expected at 600 °C regardles on the type of existed iron oxide. From Figure 7 c, d, the decomposition of iron oxides will take place in regions with higher iron contaminations if temperatures are higher than 600 °C. When riching the maximum temperature in furnace, 1550 °C, the absolute disociation of formed iron oxide FeO in regions of higher iron content is impossible as a consiquence of rather low temperature reached inside furnace and low partial pressure, seen also in Figure 5, 6.

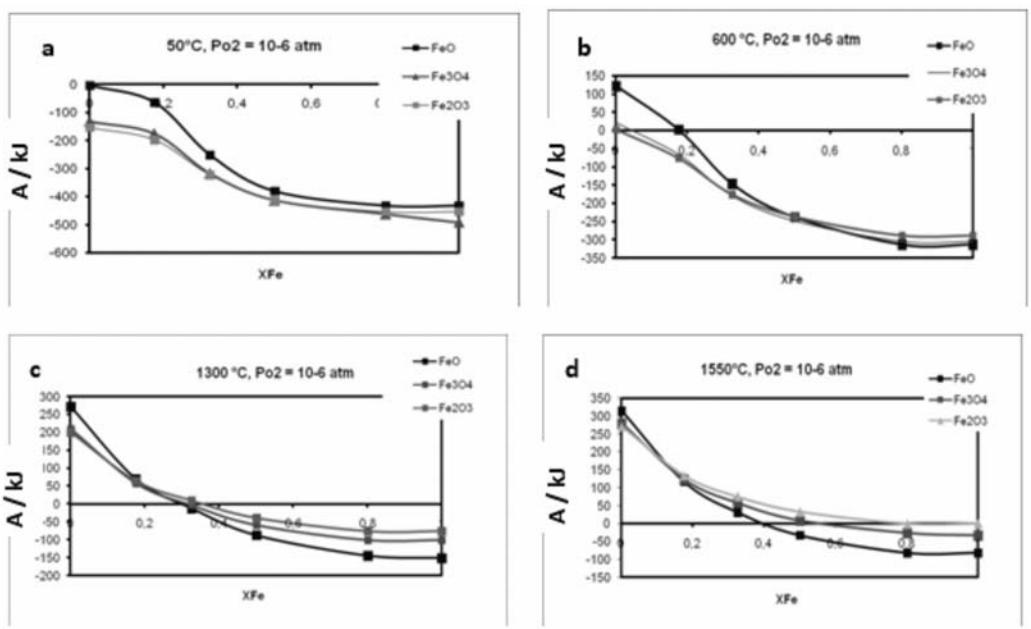

Figure 7. Diagram of oxygen affinities at various temperatures : 50 °C (a), 600 °C (b), 1300 °C (c) and 1550 °C (d)

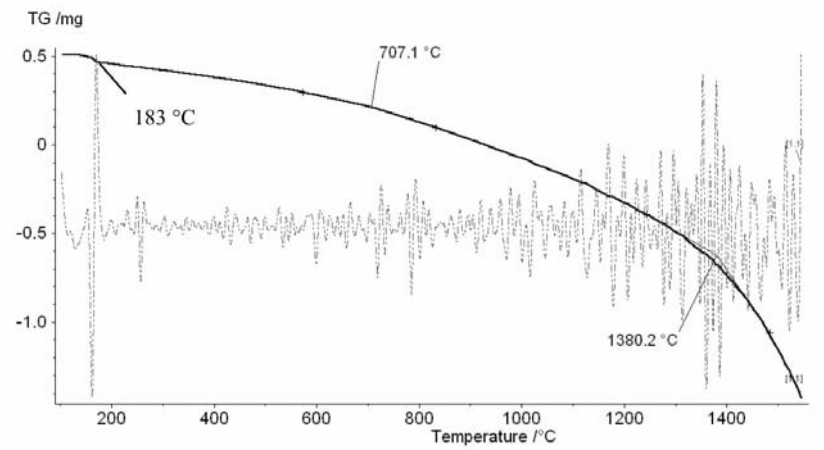

Figure 8. TG heating curve of an empty and of contaminated platinum sample holder

TG heating curve of an empty and of contaminated platinum sample holder after exposure to iron containing samples is presented in Figure 8. First peak appears at 183 °C as result of loss of humidity inside the furnace. At temperature 707 °C, the first reduction of mass was determined as a consequence of reduction of formed iron oxides. Figure 7b shows that most probable decomposition takes place with the hematite in concentrations under x_{Fe} = 0.1. The second reduction of mass, at 1380 °C, indicated a higher local contamination or longer reduction time of formed oxides. Figure 7 c shows that all three oxides can contribute to the mass decrease in TG curve. At higher temperatures, 1550 °C the most probable decomposition of wüstite takes place in the regions up to x_{Fe} = 0.4.

Conclusions

Process of oxide decomposition is complex and not sudden. The partial pressure of oxygen in the system is high enough, that oxides will not decompose to elementary iron in all concentration regions. The first change in the TG curve was expected to be at temperatures above 600 °C which is in good agreement with our experimental results. Plotted TG curve shows first visible mass decrease as a result of decomposition of hematite to elementary iron, at 707 °C, followed by continuous drop of the TG curve with decomposition of magnetite and wüstite. When contamination with other elements is present, the characteristic TG curve is changed again. And to eliminate phenomena that are not in relation to the

measured sample, basic curve should be recorded without a sample.

REFERENCES

[1] GUDMUNDSSON, G., HOLLOWAY, J. R. (1993): Activity-composition relationship in the system Fe-Pt at 1300 °C and 1400 °C and at 1 atm and 20 Kbar. American Mineralogist; Vol. 78; pp. 178–186.

[2] http://www.freepatentsonline.com/3811874.html

[3] BUSCAIL, H., COURTY, C. & LARPIN, J. P. (1995): Effects of Ceria Coatings on pure iron oxidation, comparison with extra low carbon steels. *Journal de physique IV*;Colloque C7, supplement au Journal de Physique III, Vol. 5.

[4] DEHOFF, R. (2006): Thermodynamics in material science; Taylor and Francis group.

[5] BARIN, I. & KNACKE, O. (1973): Thermochemical properties of inorganic substances; Springer-Verlag.

[6] http://www.aerogas.de/argon.html

[7] BARIN, I., KNACKE, O., KUBASCHEWSKI, O. (1977): Thermochemical properties of inorganic substances; Springer Verlag.

Simulation of multilayer coating growth in an industrial magnetron sputtering system

Simulacija rasti večplastnih prevlek v industrijski napravi za magnetronsko naprševanje

Matjaž Panjan[1,*], Miha Čekada[1], Peter Panjan[1]

[1]Jožef Stefan Institute, Jamova 39, SI-1000 Ljubljana, Slovenia

*Corresponding author. E-mail: matjaz.panjan@ijs.si

Received: July 23, 2010 **Accepted:** September 8, 2010

Abstract: Layered coatings are mainly prepared by physical vapor deposition such as magnetron sputtering. In industrial deposition systems layered coatings (e.g. multilayer or nanolayered coatings) are produced by the rotation of the substrates along the spatially separated targets. In order to assure uniform deposition on all parts of the substrate with complex geometry (e.g. tools), two- or three-fold rotation is typically applied. Such rotation is similar to the planetary rotation. A consequence of the planetary rotation are layered coatings whose structure depends on the type of the rotation. In this paper we describe a model of the sputter deposition in the deposition systems with the planetary rotation. Such model helps us understand the influence of the rotation on the layer structure of the coatings. Results of the model for different types of the substrate rotation are presented. In addition, we prepared TiAlN/CrN nanolayered coatings in an industrial magnetron sputtering system and compared their layered structures with the calculated ones. The comparison confirms the accuracy of the developed model.

Izvleček: Večplastne prevleke pripravljamo s fizikalnimi postopki nanašanja iz parne faze (PVD), kot je magnetronsko naprševanje. V industrijskih napravah večplastne prevleke pripravimo z vrtenjem podlag okoli prostorsko ločenih tarč. Podlage imajo v splošnem kompleksno geometrijo (npr. orodja), zato se morajo vrteti okrog dveh ali treh osi, pri čemer je vrtenje podobno planetarnemu vrtenju. Tako zagotovimo enakomeren nanos prevleke na vse dele

Original scientific paper

orodja. Rezultat planetarnega vrtenja so različne večplastne prevleke, katerih struktura je odvisna od načina vrtenja. V članku opisujemo model nanašanja večplastnih prevlek, ki smo ga razvili za magnetronsko napršev anje v industrijskih napravah s planetarnim vrtenjem. Model nam pomaga razumeti vpliv različnih parametrov na večplastno strukturo prevlek. V članku predstavljamo rezultate modela za različne vrste vrtenja. Za preverjanje natančnosti modela smo v industrijski napravi CC800/9 (CemeCon) pripravili nanoplastne prevleke TiAlN/CrN in njihove večplastne strukture primerjali z izračunanimi strukturami. Rezultati potrjujejo točnost modela.

Key words: modeling, layered structures, PVD, magnetron sputtering, TEM

Ključne besede: modeliranje, večplastne strukture, PVD, magnetronsko napršev anje, TEM

INTRODUCTION

Hard coatings are thin films, which are deposited on the tools and components in order to improve hardness, friction, wear and corrosion reistance of the surface. In this way the lifetime of the tools is prolonged, therefore the productivity is enhanced. Moreover, the use of hard coatings reduces the consumption of lubricants and often enables machining of new materials. Hard coatings are commonly prepared by physical vapor deposition (PVD), which offers an easy way of depositing coatings in a form of a single layer or multilayers. Layered structures are prepared by alternately depositing two or more different materials. They are composed of a few or up to several hundred layers. The thickness of the individual layers can vary from a few atomic layers up to micrometers, the structures can be periodic or aperiodic. When the thickness of the individual layers is in the nanometer range, the term nanolayered coatings is used.

Unique property of the nanolayered coatings is an extremely high hardness, which is much higher than the hardness of individual layers[1, 2]. In 1987, HELMERSSON et al.[3] published a paper in which they reported on drastic enhancement of hardness in TiN/VN nanolayered coatings. They showed that the hardness of the coating exceeded 50 GPa for the thickness of layers ≈2–4 nm, which is much more than the hardness of a single layer TiN (≈22 GPa) and VN (≈16 GPa) coatings. High hardness was interpreted as a consequence

of numerous interfaces between the individual layers and the small thickness of the layers[4]. Interfaces obstruct the movement of dislocations, while a few nanometers thick layers reduce the formation of new dislocations. Consequently, hardness of nanolayered coating can be higher than the hardness of the second hardest material, the cubic BN.

Nanolayered coatings are mainly prepared by magnetron sputtering or cathodic arc evaporation[5]. In laboratory deposition systems, nanolayered coatings are usually formed by sequential switching between two target sources[3], whereas in industrial deposition systems, nanolayered coatings are formed when the substrates rotate along spatially separated targets[6]. In the industrial deposition systems, the substrates have to rotate around two, three or even four axes in order to insure uniform coating on all parts of the substrates with complicated geometry such as tools. Rotation around different axes causes periodic and aperiodic layer structures. The layer structure depends on the number of rotational axes, revolution time around the individual axes, initial position of the substrates and on the target arrangement. The nanolayered coatings prepared in the same batch therefore have different layer structures.

The objective of our work was to develop a model of a sputtering process in an industrial deposition system with planetary rotation and to calculate the layer structure of the coatings for different parameters of the deposition. This is important because the parameters, such as planetary rotation, cause considerable variations in the thickness of individual layers and thus can influence the mechanical properties of nanolayered coatings. In this paper we are presenting the model and the results of the model for different types of the rotation. In addition, we prepared samples for transmission electron microscope and compared calculated layer structures with deposited TiAlN/CrN nanolayered coatings.

Industrial physical vapour deposition system

Nanolayered coatings are usually prepared by magnetron sputtering. A schematic top view of the industrial magnetron sputtering system CC800/9 from company CemeCon is shown in Figure 1. The deposition system has four planar magnetron sources with dimensions 500 mm × 88 mm. The sources are arranged in the corners of the rectangle. The substrates can be positioned at different heights. The turntable has the possibility of a 3-fold planetary rotation; the first axis of rotation

is in the centre of the turntable while the substrate towers rotate around the second axis, which is positioned 137 mm away from the first axis. The substrate towers rotate around the first and the second axis. The rotation around the third axis is not continuous but is achieved by a switch fixed on the rod. For every rotation of the substrate tower around the second axis, the switch turns the sample for a specific angle. The distance from the second axis to the third axis is 58 mm. The revolution time of the turntable can be adjusted from 38 s to 97 s, while the revolution time of the substrate towers is determined by the gear ratio between the turntable and the substrate tower; this ratio is 100/37.

For the experiments TiAlN/CrN nanolayered coatings were prepared by three types of the rotation; 1-, 2- and 3-fold. Coatings were deposited on D2 tool steel, hard metal and silicon substrates. Prior to deposition the samples were ground and polished, ultrasonically cleaned and ion-etched in deposition system. Substrate temperature during the deposition was ≈450 °C, power on the Cr targets was 4.5 kW and on the TiAl targets 9.5 kW. A mixture of nitrogen, argon and krypton gases was used with flow rates of (70, 150, 100) mL/min, respectively. Total gas pressure during deposition was 0.6 Pa and a DC bias of –100 V was applied to the substrates. One rotational cycle of the turntable was 97 s while the deposition time was 125 min.

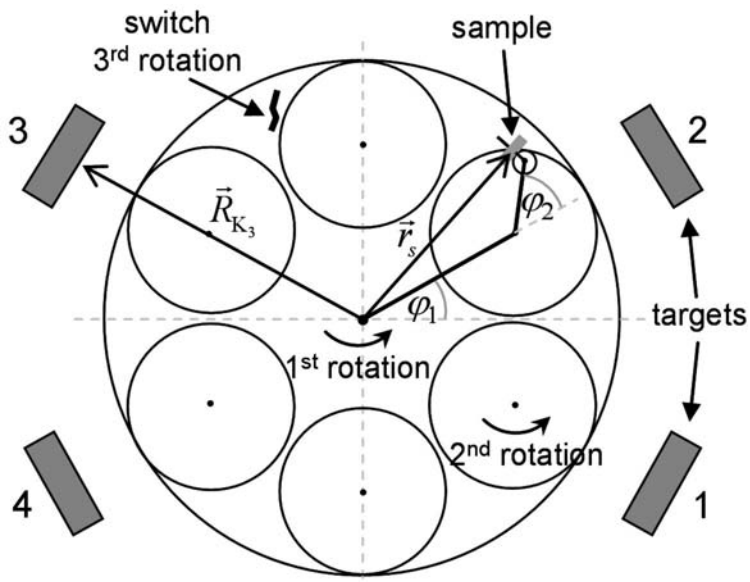

Figure 1. Schematic top view of the CC800/9 (CemeCon)

Nanolayered coatings were prepared in cross-section for the transmission electron microscopy. The samples were first cut into small pieces, glued face-to-face, fixed into brass disk holders, mechanically polished to ≈100 μm, thinned to 20 μm by dimpling and ion milled to electron transparency. Investigations were carried out on field-emission electron-source high-resolution transmission electron microscope JEOL 2010F operated at 200 keV.

Modeling of multilayer growth

The layer structure of the coating is obtained by calculating the deposition rate from a magnetron source on the surface of a rotating substrate. The deposition rate from a particular target depends on the distance from the target, the orientation between the target and the substrate and on the angular distribution of a particle flux from the target. The particle flux was modeled by two point sources where each source has a cosine angular distribution while the intensity falls with square of the distance. Similar model was introduced by Rother et al. [7–9]. In order to give a realistic description of the deposition process a shading of the particle flux by the batching material was also considered. The model assumes the following:

1. The deposition rate on the surface of the sample depends on the particular position and orientation of the substrate. The position and the orientation of the substrate (e.g. the trajectory) are defined by the planetary rotation.
2. The planetary rotation is described by the equations

$$\boldsymbol{r}_{\mathrm{s}}(t) = \sum_{i=1}^{N}\left(R_{\mathrm{i}} \cos\left(\sum_{j=1}^{i}\left(\frac{2\pi}{t_{\mathrm{j0}}} t + \varphi_{\mathrm{j}} \right)\right), R_{\mathrm{i}} \sin\left(\sum_{j=1}^{i}\left(\frac{2\pi}{t_{\mathrm{j0}}} t + \varphi_{\mathrm{j}} \right)\right), h_{\mathrm{s}} \right) \tag{1}$$

$$\boldsymbol{n}_{\mathrm{s}}(t) = \left(\sum_{j=1}^{N} \cos\left(\frac{2\pi}{t_{\mathrm{j0}}} t + \varphi_{\mathrm{j}} \right), \sum_{j=1}^{N} \sin\left(\frac{2\pi}{t_{\mathrm{j0}}} t + \varphi_{\mathrm{j}} \right), 0 \right) \tag{2}$$

where $\boldsymbol{r}_{\mathrm{s}}$ is a vector from the center of the turntable to the substrate, $\boldsymbol{n}_{\mathrm{s}}$ is orientation of the substrate, N is the number of the rotational axes, R_{i} are the radii around the individual axes, t_{j0} are time periods of one rotational cycle around the axis j, φ_{j} are initial angles around the individual axes and h_{s} is the height of the substrate (cf. Figure 1). The rotation around the third axis is not continuous. It is achieved by the switch, which turns the substrate for a certain angle when the sub-

strate makes one cycle around the second axis. This is also taken into account in equations (1) and (2).

3. The magnetron targets are considered as two point sources representing a racetrack. A particle flux j_p is modeled by the cosine angular distribution (Figure 2)

$$j_p = \frac{A}{r^2}(\cos\vartheta)^n \tag{3}$$

where r is the distance from the source to the substrate, ϑ is the angle between the sources' normal and the direction of the sputtered particles, A is the flux intensity, and n is the lateral particle distribution coefficient.

4. The surface of the substrate is coated only if it is in a direct view of the target otherwise the deposition rate is zero. Shaded areas are defined by the dot products of the following vectors (cf. Figure 3):

$$\frac{\boldsymbol{r}_s(t)-\boldsymbol{R}_h(t)}{\left|\boldsymbol{r}_s(t)-\boldsymbol{R}_h(t)\right|}\cdot\frac{\boldsymbol{R}_{K_i}(t)-\boldsymbol{R}_h(t)}{\left|\boldsymbol{R}_{K_i}(t)-\boldsymbol{R}_h(t)\right|}<\cos(90°) \tag{4}$$

$$\frac{\boldsymbol{r}_s(t)}{\left|\boldsymbol{r}_s(t)\right|}\cdot\frac{\boldsymbol{R}_{K_i}(t)}{\left|\boldsymbol{R}_{K_i}(t)\right|}<\cos(75°) \tag{5}$$

where $\boldsymbol{R}_h$ is the vector from the center of the turntable to the center of the substrate tower and $\boldsymbol{R}_{K_i}$ is the vector from the center of the turntable to the sputtering source i. The shading originates from two contributions. The substrates, which are in the shade of its own substrate tower, are described by the relation (4). The substrates, which are in the shade of other substrate towers, are described by the relation (5). The vector $\boldsymbol{R}_{K_i}$ is fixed and the vectors $\boldsymbol{r}_s(t)$ and $\boldsymbol{R}_h(t)$ change with the time.

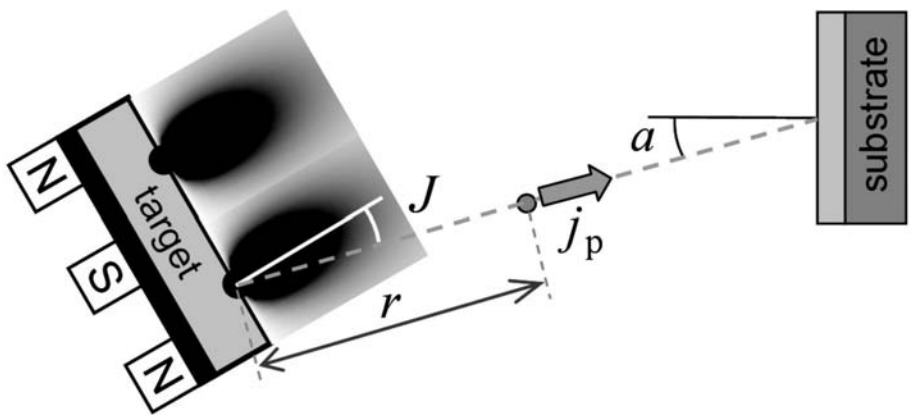

Figure 2. Particle flux from the magnetron target

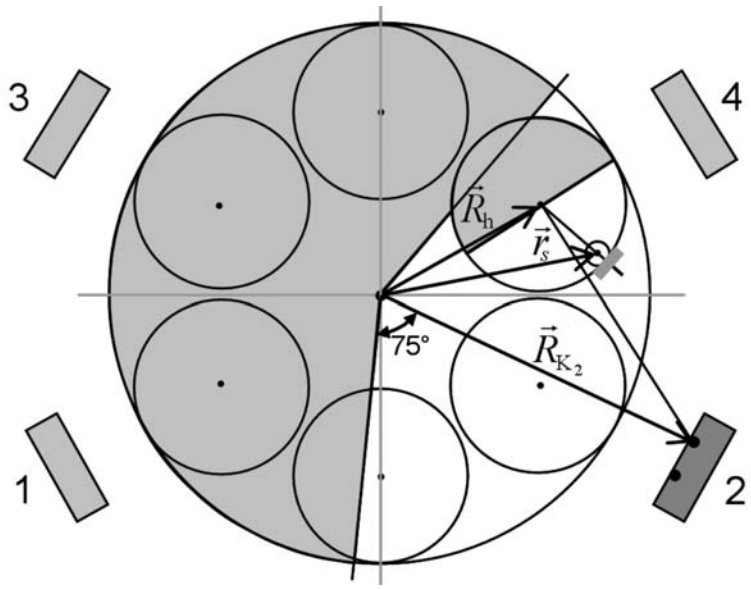

Figure 3. Shaded area (grey) of the particle flux coming from target 2

The deposition rate on the substrate changes due to rotation. When the substrate is close to the target and is fa-cing its direction, the deposition rate is high. If the substrate is far away from the target, the deposition rate is low, or zero if it is facing away from the target. The rotation is defined by equations (1) to (3). The distance between the target *i* and the substrate $|\boldsymbol{R}_{K_i} - \boldsymbol{r}_s(t)|$ changes with the rotation. The particle flux from all the targets at the position of the substrate is

$$j_p = \sum_{i=1}^{N} \frac{A_i}{(\boldsymbol{R}_{K_i} - \boldsymbol{r}_s)^2} (\cos\vartheta_i)^n \qquad (6)$$

where ϑ_i is the angle between the target *i* normal and the direction of the particle flux to the substrate, A_i is the flux intensity from the target *i*, and *n* determines the shape of the angular distribution.

The deposition rate (v) on the surface of the substrate is proportional to the particle flux from all targets (j_{pi}) and it depends on the particle flux angle of incidence α_i (see Figure 2)

$$v = \sum_{i=1}^{N} j_{pi} \cos\alpha_i \qquad (7)$$

In the simulation, it is considered that the growth of the coating is only possible if $-90° < \alpha_i < 90°$. In these positions, the surface of the substrate faces the target, for all other angels the surface is shaded and $v = 0$.

The equation (7) describes the variations of the deposition rate in dependence of the time. Integration of the deposition rate with respect to the time gives the thickness (h) of the individual layers

$$h = \int_0^t v(t)dt \tag{8}$$

In the final step of the simulation, the calculated thicknesses of individual layers are graphically represented in a form of a layered structure. An example of the calculated deposition rate and layer structure is shown on Figure 4a and Figure 4b, respectively. Calculations were made for 3-fold rotation with two targets of equal material on one side of the deposition chamber and two targets of other material on the other side.

RESULTS AND DISCUSSION

The model described above was used to analyze the influence of different parameters on the layered structures. The layer structure depends on the initial position of the sample, type of rotation, configuration of targets and on geometrical parameters of the deposition system. Here we will discuss only the influence of 1-, 2- and 3-fold rotation on the layer structures. In order to prove the accuracy of the model we have also compared the TiAlN/CrN nanolayered coatings prepared by all types of rotation to the calculated layer structures.

Figure 5 shows the calculated deposition rate and layer structures for 1-, 2- and 3-fold rotation. Calculations were made for the CC800/9 deposi-

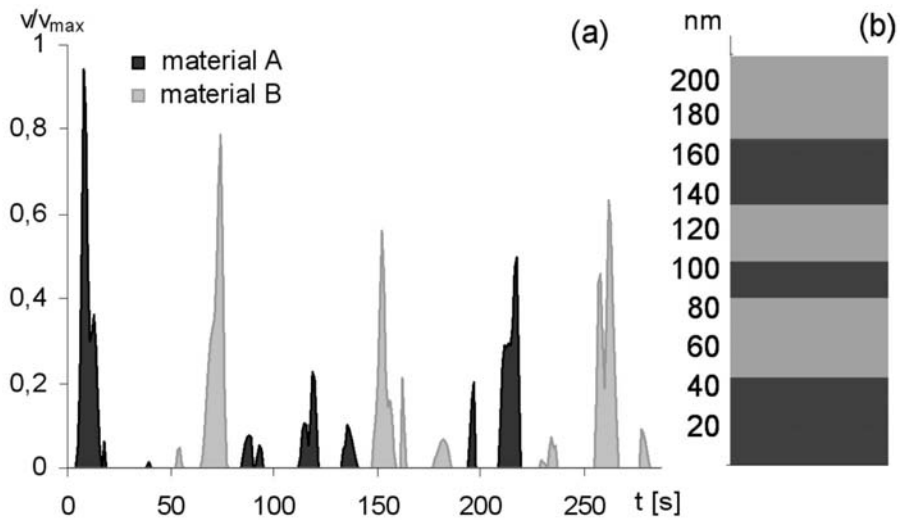

Figure 4. (a) The deposition rate as function of time and (b) the layered structure. Calculation was made for 3-fold rotation

tion system with two Cr targets on one side of the vacuum chamber and two TiAl targets on the opposite side. The deposition rates and the layered structures differ between three types of rotation quite considerably. In the case of a **1-fold rotation** (Figure 5a), the deposition rate and layered structure is periodic. The substrates travel on identical trajectory for each rotation of the turntable, thus, the deposition rate and the layer structure are periodic. In each rotation of the turntable, the substrate is equally exposed to the TiAl and the Cr targets, thus, the individual layers have the same thickness (≈100 nm).

The deposition rate and layered structure for **2-fold rotation** is shown on Figure 5b. Additional rotation around the second axis influences the periodicity of the layer structure. The periodicity of the layer structures prepared by 2-fold rotation depends on the gear ratio between the turntable and the substrate tower. In the CC800/9 deposition system, the gear ratio is 100 : 37, which means that the substrate returns into an identical position only after 37 rotations of the turntable. Therefore, the layer structure for the 2-fold rotation repeats after $2 \cdot 37 = 74$ deposited layers (in each rotational cycle, 2 layers are deposited). Although the periodicity is quite large the thickness of the individual layers is approximately the same because in each rotational cycle of the turntable the sample is almost equally exposed to the targets; hence, the thickness of the individual layers varies only slightly.

In the case of a **3-fold rotation**, the periodicity of the layer structure is the most complex (cf. Figure 5c) due to the non-continuous rotation of the switch which turns the sample for a certain angle for each rotation around the second axis. Rotation around the third axis affects only the orientation of the substrate and less its position. The reason is the small radius of rotation around the third axis (e.g. 5 mm for drills) compared to the radii of rotation around the first (137 mm) and the second axis (58 mm). Thus, 3-fold rotation is essentially 2-fold rotation superimposed on a non-continuous third rotation, which only changes the orientation of the substrate. The periodicity of the layer structure produced by 3-fold rotation depends both on the gear ratio and the switch angle. In principle, the planetary rotation always produces periodic layer structures if the periodicity is observed on a large scale. However, on the scale of the deposition time (≈1 h), the layer structures can be periodic or aperiodic. The layer structure is periodic if the substrate returns into an identical position after a particular number of the turntable rotations. If this does not happen during the deposition time, the layer structure of the coating is aperiodic. In practice, layered structures prepared by 3-fold rotation are usually aperiodic.

From the Figure 5 it can be seen that the total thickness of the coating strongly depends on the type of rotation. In the case of 1-fold rotation, the total thickness for 5 rotations of the turntable is ≈900 nm, for 2-fold rotation ≈400 nm

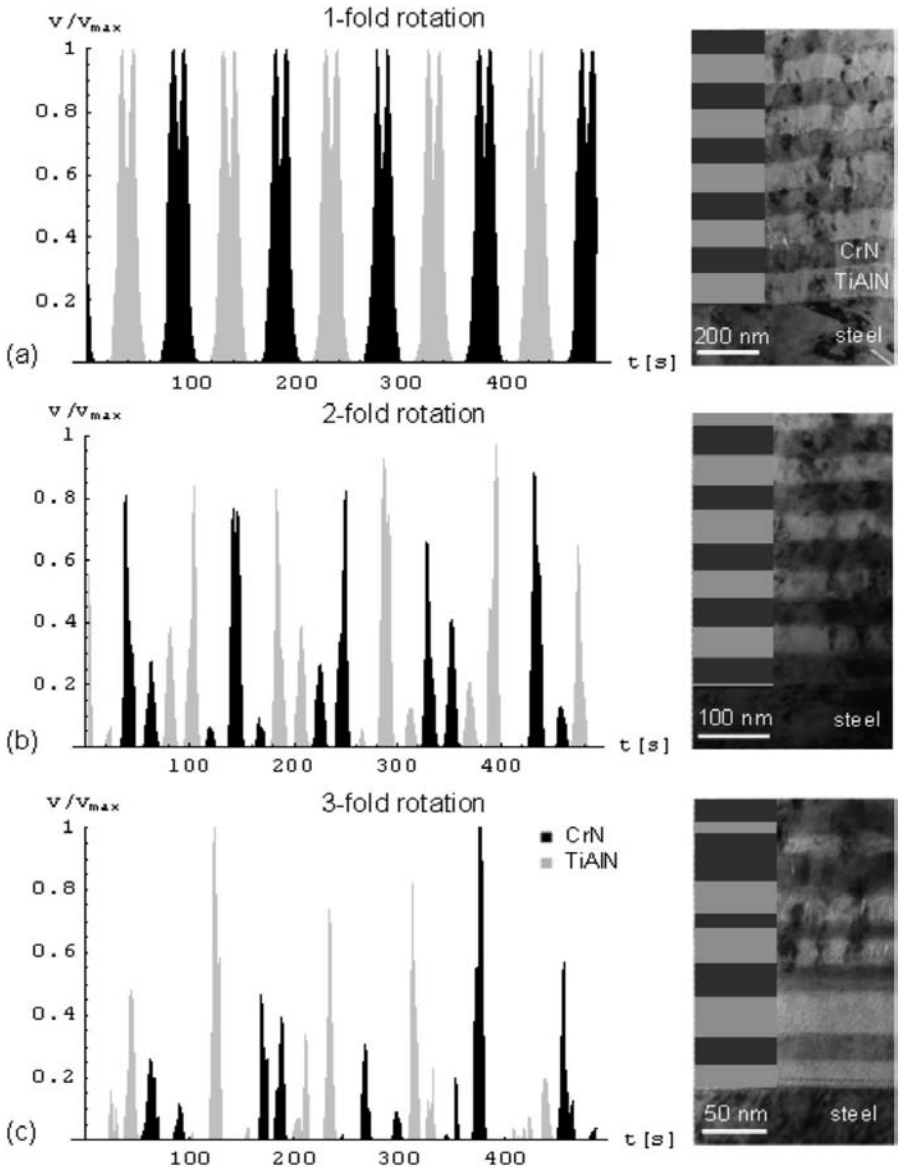

Figure 5. The deposition rate and the layer structure for (a) 1-, (b) 2-, and (c) 3-fold rotation. Calculated layered structures are compared to the TEM micrographs of the deposited TiAlN/CrN nanolayered coatings[10]

and for 3-fold rotation ≈220 nm. The corresponding average deposition rates are 1.8 nm/s, 0.8 nm/s, and 0.45 nm/s for the 1-, 2- and 3-fold rotation, respectively. Hence, the rotation around an additional axis considerably lowers the average deposition rate. Thus, if the coating in the same batch is deposited on the substrates with different types of the rotation, then the total thickness of the coatings will be considerably different.

On the right side of the Figure 5, the calculated layer structures are compared to the deposited TiAlN/CrN nanolayered coatings. The coatings were prepared by the three types of the rotation; 1-, 2- and 3-fold. The bright layers correspond to TiAlN and the dark layers to CrN. Comparison between the calculated and the deposited layer structures shows good overlap between the structures in the case of 1- and 2-fold rotations. In the case of the 3-fold rotation the agreement is less accurate although still satisfactory. Nevertheless, the discrepancy is mainly caused by the experimental difficulties during the deposition.

The accuracy of the model used for calculating the layer structure is influenced by different factors. The simulation is only an approximation of the deposition process. In the model, the angular particle flux from the target was approximated by the cosine law. Different distributions were also tested (e.g. a cosine square distribution); however, this did not influence the layer structure considerably. A more important source of error in the model is a contribution of ionized particles to the deposition of the coating (ionization of the target material is ≈10 %). In the simulation, only particles (atoms) which travel in a straight line were considered. Ions whose path is determined by the electrical field (bias on the substrates) are neglected. The scattering of the particles and resputtering effects are also not considered in the model. However, these effects probably have only a minor influence on the accuracy of the model.

The most important source of error is probably the switch. The switch does not always turn the sample for the same angle. However, the simulations have shown that already a small change in the switch angle (e.g. 5°) produces considerable variations in the layer structure. Such stochastic rotational causes an increase of the error with every rotational cycle. This is seen, for example, in Figure 5c, where after a few deposited layers the agreement between the calculated and the deposited layer structure is lost.

Despite the approximations used in the model and the experimental difficulties it can be concluded that the model

quite accurately describes the deposition process of layered structures. Therefore, we believe that this model can be used to explain various layer structures which are obtained by different parameters of the deposition. Thus, such simulations would be a benefit to the engineers who design industrial deposition systems.

CONCLUSIONS

A model of a sputtering process in an industrial magnetron sputtering system with the planetary rotation was developed in order to understand the influence of the rotation on the layered structures. Layered structures prepared by 1-, 2- or 3-fold rotation were analyzed by the model. The results of the model show that the periodicity of the deposition rate and consequently of the layer structure significantly depends on the type of rotation as well as on the other parameters. To verify the accuracy of the model we prepared TiAlN/CrN nanolayered coatings by the three types of rotation in the industrial magnetron sputtering system CC800/9 from CemeCon. The results show good agreement between the prepared and calculated layer structures. Thus, we can conclude that the model correctly describes the deposition process and therefore it could be used to predict the layer structures for different parameters of the process.

Acknowledgments

This work was supported by the Slovenian Research Agency (project L2-9189).

REFERENCES

[1] M. STUEBER, H. HOLLECK, H. LEISTE, K. SEEMANN, S. ULRICH, C. ZIEBERT (2009): Concepts for the design of advanced nanoscale PVD multilayer protective thin films. *J. Alloys Compd.*, *483*, pp. 321–333.

[2] A. CAVALEIRO, J. T. M. DE HOSSON (2006): Nanostructured Coatings. (*Springer Science, New York*).

[3] U. HELMERSSON, S. TODOROVA, S. A. BARNETT, J. E. SUNDGREN, L. C. MARKERT, J. E. GREENE (1987): Growth of single-crystal TiN/VN strained-layer superlattices with extremely high mechanical hardness. *Journal of Applied Physics*, *62*, pp. 481–484.

[4] P. C. YASHAR, W. D. SPROUL (1999): Nanometer scale multilayered hard coatings. *Vacuum*, *55*, pp. 179–190.

[5] D. MATTOX (1998): Handbook of Physical Vapor Deposition Processing. (*Noyes Publications, Westwood*).

[6] W.-D. MUNZ (2003): Large-Scale Manufacturing of Nanoscale Multilayered Hard Coatings Deposited by Cathodic Arc/Unbalanced Magnetron Sputtering. *MRS Bulletin*, *28*, pp. 173.

[7] B. Rother (1994): *Surf. Coat. Technol.*, *64*, pp. 155.

[8] B. Rother, H. A. Jehn, H. M. Gabriel (1996): *Surf. Coat. Technol.*, 86–87, pp. 207.

[9] B. Rother, G. Ebersbach, H. M. Gabriel (1999): *Surf. Coat. Technol.*, *116–119*, pp. 694.

[10] M. Panjan, T. Peterman, M. Cekada, P. Panjan (2009): Simulation of a multilayer structure in coatings prepared by magnetron sputtering. *Surf. Coat. Technol.*, *204*, pp. 850–853.

Durability evaluation of some Slovenian building limestones

Vrednotenje obstojnosti izbranih slovenskih apnencev kot naravnega kamna

Sabina Kramar[1, *], Ana Mladenović[2], Mitja Kozamernik[3] & Breda Mirtič[4]

[1]Institute for the Protection of Cultural Heritage of Slovenia, Conservation Centre, Restoration Centre, Poljanska 40, SI-1000 Ljubljana, Slovenia
[2]Slovenian National Building and Civil Engineering Institute, Dimičeva 12, SI-1000 Ljubljana, Slovenia
[3]IGMAT d. d., Building Materials Institute, Polje 351c, 1260 Ljubljana
[4]University of Ljubljana, Faculty of Natural Sciences and Engineering, Department of Geology, Aškerčeva 12, SI-1000 Ljubljana, Slovenia

*Corresponding author. E-mail: sabina.kramar@rescen.si

Received: June 1, 2010 **Accepted:** July 23, 2010

Abstract This study deals with the characterisation of two limestones widely used in the construction of Slovenian historical monuments as well as modern buildings. In order to estimate their durability, samples of the selected limestones were subjected to salt crystallisation and frost resistance tests. Changes in the structure of the limestones after these ageing tests were determined using SEM-EDS and USV measurements. In addition, their splitting tensile strength was also determined. Results showed that despite having good mechanical characteristics, the limestones exhibited several forms of deterioration when exposed to the deleterious agents.

Izvleček V prispevku sta obravnavana dva slovenska apnenca, ki sta bila široko uporabljena pri gradnji številnih objektov kulturne dediščine, eden od njiju je še vedno aktualen pri gradnji modernih objektov. Za oceno obstojnostne lastnosti so bili vzorci izbranih apnencev izpostavljeni preizkusom odpornosti proti kristalizaciji soli in odpornosti proti zmrzovanju. Spremembe v strukturi kamnine po preizkusih staranja so bile preverjene z uporabo SEM-EDS-metode in z USV-meritvami. Določena je bila tudi natezna razcepna trdnost preiskovanih apnencev. Rezultati kažejo, da kjub dobrim mehan-

Original scientific paper

skim karakteristikam preiskovanih apnencev le-ti propadajo, ko so izpostavljeni škodljivim dejavnikom.

Key words: limestone, durability, deterioration, salt crystallisation, natural stone
Kjučne besede: apnenec, obstojnost, propadanje, kristalizacija soli, naravni kamen

INTRODUCTION

Since prehistoric times, limestone has been one of the most popular types of building stone and is today used in both the construction of modern buildings and in conservation as a replacement material for the reconstruction of monuments. All stone used in these applications eventually changes due to their interaction with the various environmental conditions to which they are subjected. Although limestone consists mainly of calcite, it can show significant variation in composition in terms of minor minerals, as well as structure and texture, resulting in complex and contrasting weathering behaviours (WARKE et al., 2006). Among the decay factors, soluble salt crystallisation is considered to be one of the most powerful affecting the weathering of carbonate stone (CHAROLA, 2000; DOEHNE, 2002). These salts are known to cause damage to porous materials through a variety of mechanisms, such as the production of physical stress resulting from their crystallisation in the pores, differential thermal expansion, hydration pressure and enhanced wet/dry cycling caused by deliquescent salts (CHAROLA, 2000; DOEHNE, 2002).

As many Slovenian monuments and modern buildings are built of limestones, estimation of their durability is necessary for their successful maintenance, protection and proper restoration/conservation. Two Slovenian limestones were selected for study: Lesno Brdo and Drenov Grič. Lesno Brdo limestone is characterised by a variety of colours: red, pink and numerous shades of light to dark grey. It has been frequently employed in the construction of Slovenian historical monuments (MIRTIČ et al., 1999; RAMOVŠ, 2000; JARC, 2000), as well as in modern buildings. In the past, the limestone was also used in many churches in Ljubljana, for portals or fountains (RAMOVŠ, 2000). In modern buildings it is used for cladding and flooring, or as a replacement material in the conservation and restoration of historical monuments. Drenov Grič limestone on the other hand, is dense and as such can produce a highly polished finish. As a

result it was considered as popular as marble, being widely used particularly in baroque architecture not only in Ljubljana, but also in other regions of Slovenia. Many interior and exterior architectural elements and monuments, especially the portals of houses and altars, were made of this limestone (Ramovš, 2000). However, both limestones are at risk when exposed to certain climatic conditions, with chromatic and salt weathering recognised as the phenomena most responsible for their deterioration (Kramar et al., 2010a; Kramar et al., 2010b).

In order to estimate the weathering behaviour of the selected limestones, samples were subjected to the salt crystallisation test and freeze/thaw cycles. Changes in the mechanical-physical properties of the limestones after these ageing tests were estimated via ultrasonic velocity measurements and SEM examination. In addition, the splitting tensile strength of the fresh limestones was also determined.

Materials and methods

Materials

For the study, two Slovenian limestones were selected; Lesno Brdo and Drenov Grič. Samples of Drenov Grič limestone (DG) were collected from the main quarry in Drenov Grič near Ljubljana (Figure 1a), which historically had a leading role in supplying building material to central parts of Slovenia (Ramovš, 2000). This Triassic well-stratified limestone occurs in 10–80 cm thick beds, which alternate with thin sheets of marls. The Drenov Grič limestone is considered one of the most beautiful Slovenian natural stones due to its typical black colour interwoven with white veins (Figure 1b). Fragments of fossil bivalvia, gastropoda, algae, foraminifera, ostracods and corals are also occasionally found (Ramovš, 2000). Samples of Lesno Brdo limestone were taken from the still active local quarry of Lesno Brdo near Ljubljana (Figure 2a). Two lithotypes of this Triassic reef limestone were selected: the dark grey lithotype – SLB (Figure 2b) and the light red lithotype - PLB (Figure 2c). Lesno Brdo limestone is heterogeneous, composed of intraclasts, pellets and fossil fragments. Coloured (violet, red, green and white) veins and styloliths filled with phyllosilicates or iron oxides/hydroxides are also present, along with large yellow or violet dolomite crystals (Ramovš, 2000).

Analytical methods

Analysis of the limestones' splitting tensile strength was performed according to SIST EN 12390-6, using a ZWICK apparatus b24, type Z 400 E. Samples took the form of (50 × 50 × 50) mm cubes,

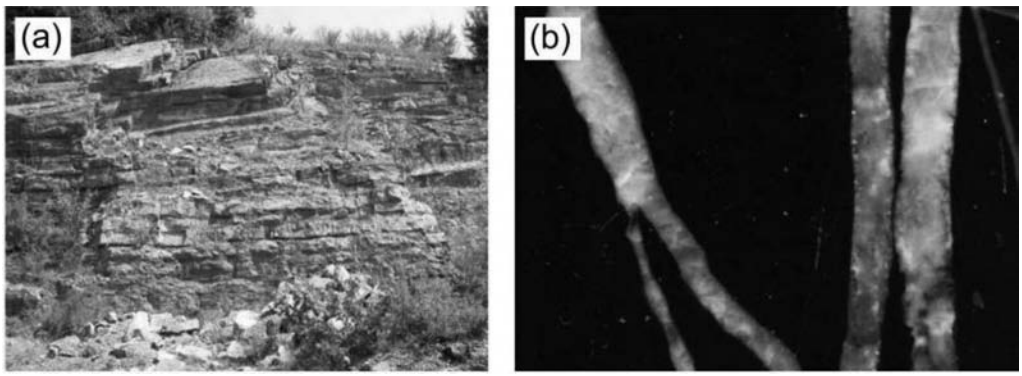

Figure 1. a) Historical Drenov Grič limestone quarry. b) Polished surface of Drenov Grič limestone. Image is about 4 cm in size.

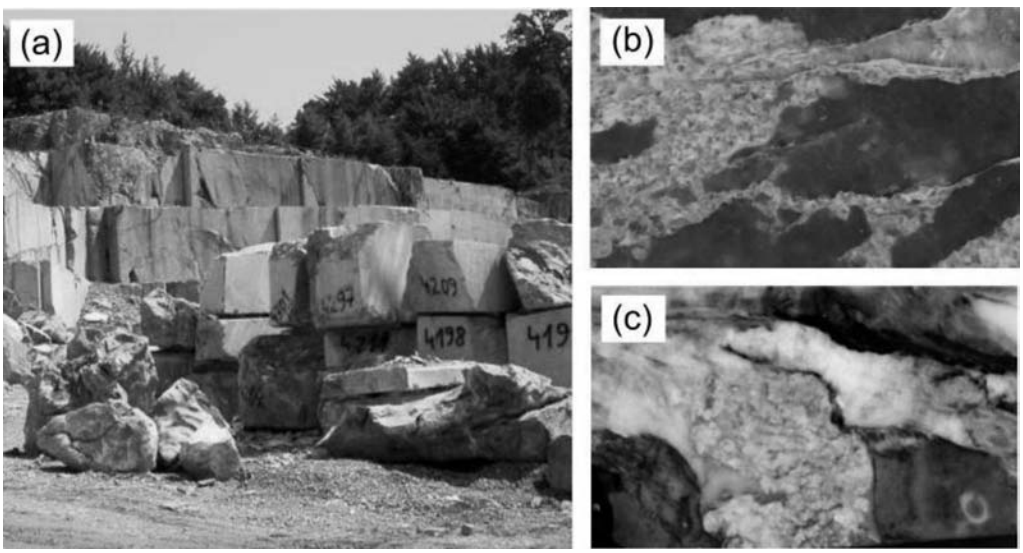

Figure 2. a) Active Lesno Brdo limestone quarry. b) Polished surface of the grey lithotype of Lesno Brdo limestone. Image is about 4 cm in size. c) Polished surface of the red lithotype of Lesno Brdo limestone. Image is about 4 cm in size.

with three taken from each limestone lithotype. Measurements were performed on dry as well as water-saturated samples (water immersion undertaken according to SIST EN 1936).

The salt crystallisation test (SIST EN 12370) and the determination of frost resistance (SIST EN 12371) were carried out on (50 × 50 × 50) mm cubes in order to provide information as to

their damaging effect. After the frost resistance test, limestone loss of mass Vb48 was determined. Changes in microstructure were observed using SEM-EDX and USV after 15 immersions in Na-sulphate and 48 freeze-thaw cycles.

Cross-sections of the weathered limestone samples were examined under a Scanning Electron Microscope (JEOL 5600 LV), using the low vacuum back-scattered electrons (BSE) imaging mode. Some areas of the samples were analysed for chemical composition using the energy dispersive X-ray technique (EDS).

In order to determine changes in the mechanical-physical properties of the samples after the ageing procedures were carried out, ultrasonic velocity measurements were performed in three directions using an AU 2000 Ultrasonic Tester (CEBTP) with a transmission frequency of 60 kHz. Speed of sound wave propagation was undertaken according to standard procedure EN 14579. Three measurements were performed in each of the three orthogonal directions. Additionally, the total structural anisotropy coefficient ΔM/% and relative anisotropy coefficient Δm/% of the samples were obtained from the mathematical relationship between the ultrasonic propagation velocities, following the equations of Guydader & Denis (1986):

a) total anisotropy:

$$\Delta M/\% = 100\,[1 - (2\,V_{L1}/V_{L2} + V_{L3})] \quad (1)$$

b) relative anisotropy:

$$\Delta m\% = 100\,[2\,(V_{L2} - V_{L3})/V_{L2} + V_{L3}] \quad (2)$$

where V_{L1} is the lowest and V_{L2} the highest measured velocity.

The degree of weathering can be calculated through the reduction of longitudinal wave velocity (Zezza & Veinale, 1988) from unweathered (V_0) to weathered (V_w) stone samples:

$$K = (V_0 - V_w)/V_0 \text{ or } \Delta V(\mathrm{L})\% = 100\,(V_0 - V_w)/V_0 \quad (3)$$

USV measurements were carried out both before and after the salt crystallisation (on unwashed and washed specimens) and frost resistance tests.

Results and discussion

Splitting tensile strength

As can be seen from Table 1, all three limestones exhibited high values of splitting tensile strength, although levels slightly differed between each one. The highest strength was observed in the grey lithotype of the Lesno Brdo limestone, followed by Drenov Grič limestone and the red Lesno Brdo lithotype. There were no significant differences observed between the different orientations of bedding planes

Table 1. Splitting tensile strength of the investigated limestones. Results represent three sample mean values ± standard deviation.

Sample	Splitting tensile strength (MPa)	
Drenov Grič limestone (DG)	dry	water-saturated
⊥ bedding	11.70 ± 4.72	11.13 ± 3.91
// bedding	13.43 ± 3.12	
Lesno Brdo limestone		
Grey lithotype (SLB)	14.22 ± 1.85	14.40 ± 4.85
Red lithotype (PLB)	11.62 ± 4.57	12.72 ± 5.63

in Drenov Grič limestone. Using the system of BELL (1992), all three investigated limestones can be classified as very high (3–10 MPa) to extremely high strength rock (>10 MPa). There was also no difference in splitting tensile strength between the corresponding dry and water-saturated samples of each of the limestones.

Analysis of the results suggests that the higher the content of clay mineral-filled discontinuities, as observed in the red Lesno Brdo lithotype (KRAMAR et al., 2010a) and the higher the porosity, the lower the splitting tensile strength of the limestone. In addition, the results also reveal that splitting tensile strength values are much lower than those of the salt crystallisation or ice formation pressures. Salt crystallisation is accompanied by an increase in pressure due to the formation of new mineral phases. Whereas the splitting tensile strength of the investigated limestones does not exceed 20 MPa, the crystallisation pressures of the most soluble salts range from more than 100 MPa (GOUDIE & VILES, 1997). As a result, the occurrence of crystallisation or hydration within these rocks would lead to the disruption of the material.

USV measurements

Results of the ultrasonic velocity analysis are presented in Table 2. The fresh SLB samples revealed faster ultrasonic wave propagation, suggesting a greater compactness and higher mechanical resistance with respect to the PLB and DG samples. In contrast, total structural anisotropy - ΔM and relative structural anisotropy - Δm values are lower in SLB than PLB samples. The large difference between the total and relative anisotropy in the DG samples is due to the presence of bedding planes within the limestone. As ultrasound velocity increases with density, compressive strength and water saturation,

but decreases with porosity (Bouineau, 1978), the results indicate the higher compactness and homogeneity of the SLB samples, followed by PLB and DG.

Durability

Limestone samples were subjected to salt crystallisation and frost resistance tests, before subsequently being observed by SEM and undergoing sound wave propagation (USV) measurements. After these ageing tests were carried out, some changes in microstructure were observed.

SEM examination of samples revealed that post-ageing test limestone deterioration was expressed as granular disintegration, fissuring or flaking. These features were observed in both lithotypes of the Lesno Brdo limestone

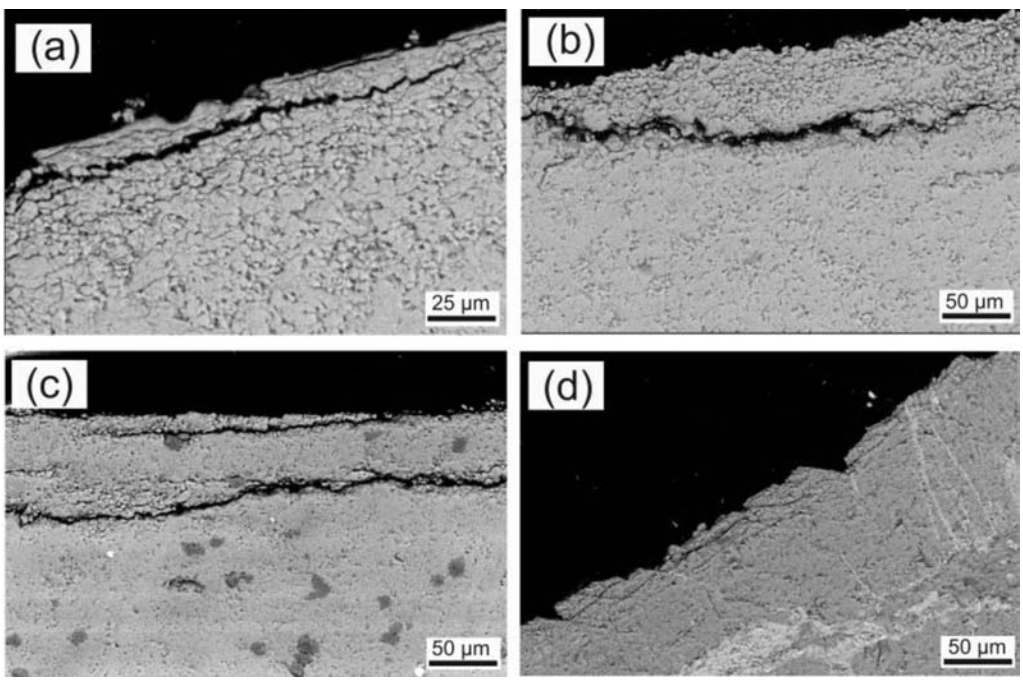

Figure 3. SEM-BSE images of investigated limestones after the ageing tests. a) Flaking of the grey Lesno Brdo limestone lithotype after salt crystallisation. b) Flaking of the red Lesno Brdo limestone lithotype after salt crystallisation is associated with the presence of phyllosilicate-filled discontinuities. Granular disintegration can also be observed at the surface. c) Flaking of the Drenov Grič limestone after salt crystallisation. d) Deterioration along cleavage planes of the grey Lesno Brdo limestone lithotype after the frost resistance test.

after salt crystallisation (Figure 3a). Fissuring and granular disintegration were limited to the upper 50 μm or so beyond the limestone surface, whereas flakes occurred up to a depth of around 25 μm. Flaking was in some cases related to the presence of phyllosilicate-filled discontinuities, as can be seen in Figure 3b. Some samples also displayed an etched surface, probably the result of dissolution caused by the salt solutions. The coarse grained dolomite was deteriorated along cleavage planes. The area of deterioration in Drenov Grič limestone after salt crystallisation was rather deeper than that observed in both Lesno Brdo lithotypes. Flaking (Figure 3c) was observed to a depth of 50 μm to 100 μm from the surface, in some areas up to 200 μm. Granular disintegration was restricted to the upper 20 μm of the samples.

Analysis of the frost resistance test results revealed no measurable loss of limestone mass, except in one DGb sample, where a small loss was observed (V_{b48} = –0.06). Thus according to the general criteria, the limestones can be considered to be highly resistant to frost action. In contrast however, SEM examination of samples revealed several deterioration phenomena. Both lithotypes of Lesno Brdo limestone were affected, with granular disintegration observed 25–80 μm under the surface, although in most cases decohesion was restricted to a depth of about 50 μm. Coarse-grained dolomite degraded along cleavage planes up to 25 μm below the surface (Figure 3d). In addition, Drenov Grič limestone showed a system of fissures occurring parallel to the surface at depths of up to 200 μm. Decohesion between grains was observed at depths of up to 50 μm, while sparitic vein decohesion occurred even deeper, up to 200 μm below the sample surface.

As seen from Table 2, there were measurable reductions in ultrasound velocity in the majority of samples before and after the crystallisation (15 immersions in Na_2SO_4) and frost resistance tests (48 cycles). A decrease in ultrasound velocity indicates the occurrence of deterioration, corroborating the observations made by SEM examination. It is also widely known that a decrease in ultrasound velocity suggests the presence of discontinuities or other obstacles within stone (FASSINA et al., 1993).

An increase in total structural anisotropy after the salt crystallisation and frost resistance tests was observed for all investigated limestones. Furthermore, the total structural anisotropy was always lower in unwashed compared with washed samples, suggesting that salt crystals filled the discontinuities and pores in the limestone, resulting in a temporary reduction in anisotropy (PAPIDA et al., 2000). In general, the samples' relative anisotropy increased

after undergoing the ageing tests. In PLB and DG samples, a decrease in relative structural anisotropy was observed in unwashed samples, probably for the same reason as described above for total structural anisotropy. These results correlate with the findings of other studies (Cultrone et al., 2008; Cardell et al., 2008), who have also reported an increase in velocity and structural anisotropy after the salt crystallisation test. The degree of weathering *V*/% of the samples was always higher after the salt crystallisation test compared to the frost resistance test for all investigated limestones. This is in agreement with SEM observations, where the samples always demonstrated higher damage after salt crystallisation. In terms of the salt crystallisation test alone, the degree of weathering was always higher in washed than unwashed samples.

Table 2. Results of USV measurements: v1-3 = average values± standard deviation of ultrasound velocities in all three orthogonal directions of the investigated limestones, ΔM (%) = total anisotropy, Δm (%) =relative anisotropy, ΔV_L (%) = degree of weathering.

Samples		Salt crystallisation SIST EN 12370			Frost resistance SIST EN 12371	
Drenov Grič limestone		unweathered	weathered		unweathered	weathered
			unwashed	washed		
DG	v1 (km/s)	4.76 ± 0.36	4.76 ± 0.46	4.77 ± 0.46	4.78 ± 0.22	4.67 ± 0.42
	v2 (km/s)	4.63 ± 0.54	4.58 ± 0.51	4.11 ± 0.77	4.69 ± 0.27	4.61 ± 0.26
	v3 (km/s)	4.22 ± 0.82	4.77 ± 0.69	4.09 ± 1.19	4.49 ± 0.06	4.54 ± 0.11
	ΔM_p/%	10.29 ± 8.45	10.27 ± 6.91	14.09 ± 12.32	5.05 ± 3.00	6.17 ± 1.98
	Δm_p/%	2.42 ± 3.68	7.16 ± 4.12	12.33 ± 12.33	2.08 ± 2.25	3.75 ± 2.58
	ΔV_L/%		(-) 3.98 ± 7.86	4.70 ± 5.85		0.96 ± 1.82
Lesno Brdo limestone						
Grey lithotype						
SLB	v1 (km/s)	5.23 ± 0.29	4.71 ± 0.49	4.73 ± 0.53	5.21±0.21	4.95 ± 0.17
	v2 (km/s)	5.16 ± 0.33	4.89 ± 0.55	4.98 ± 0.78	5.04±0.17	4.99 ± 0.12
	v3 (km/s)	5.04 ± 0.33	4.84 ± 0.27	4.69 ± 0.57	4.99±0.08	4.74 ± 0.12
	ΔM_p/%	3.19 ± 1.96	4.71 ± 3.00	4.10 ± 2.59	2.57 ± 2.29	4.65 ± 4.27
	Δm_p/%	1.39 ± 1.28	5.03 ± 2.17	7.26 ± 6.18	3.22 ± 2.45	2.93 ±1.52
	ΔV_L/%		6.38 ± 3.15	6.65 ± 3.05		3.66 ± 2.31
Red lithotype						
PLB	v1 (km/s)	5.19 ± 0.21	4.42 ± 0.35	4.74 ± 0.13	4.82±0.25	4.65 ± 0.14
	v2 (km/s)	4.88 ± 0.39	4.73 ± 0.57	4.76 ± 0.36	4.61±0.22	4.51 ± 0.28
	v3 (km/s)	4.53 ± 0.64	4.66 ± 0.13	4.11 ± 0.56	4.35±0.03	4.35 ± 0.04
	ΔM_p/%	10.29 ± 8.80	7.02 ± 5.90	15.55 ± 7.58	6.67 ± 4.93	7.18 ± 2.36
	Δm_p/%	6.32 ± 6.80	1.42 ± 0.82	3.19 ± 2.47	4.61 ± 3.70	9.98 ± 1.17
	ΔV_L/%		5.01 ± 9.01	6.80 ± 3.77		1.90 ± 1.78

A negative trend was observed in the Drenov Grič limestone, suggesting that salt filled the pores and resulted in increased limestone compactness. In general, USV data reveal that the DG samples experienced the least amount of change after undergoing ageing.

Sodium sulphate is one of the most important salts responsible for the damage of natural stone (Goudie and Viles, 1997). At room temperature, sodium sulphate has two stable phases: thenardite (Na_2SO_4) and mirabilite ($Na_2SO_4x10H_2O$), with a metastable phase represented by sodium sulphate heptahydrate ($Na_2SO_4x7H_2O$). The high damage potential of sodium sulphate has been studied by several authors (Schaffer, 1932; Evans, 1970; Marschner, 1978; Sperling & Cooke, 1985; Goudie & Viles, 1997), with the salt also contributing to tests studying the durability of building materials (ASTM C88-90, RILEM PEM/25, SIST EN 12370). Tests involving sodium sulphate were first carried out by Brard (1828), who used a saturated solution of sodium sulphate for simulation of the frost resistance of natural stone. Since then, a similar procedure has been used in several types of accelerated ageing test, with the aim of simulating the deterioration of natural stone, concrete and other building materials (Sperling & Cooke, 1985; Kwaad, 1970; Fahey, 1986; Rodríguez-Navarro et al., 2000; Benavente et al., 1999; Benavente et al., 2001; Flatt, 2002; Benavente et al., 2004; Benavente et al., 2007; Ruiz-Agudo et al., 2007; Rothert et al., 2007; Cardell et al., 2008). The choice of sodium sulphate is based mainly on two factors: (i) its frequent occurrence in objects or environments (Arnold & Zehnder, 1988; Tuncoku et al., 1993; Bromblet, 1993; Fassina et al., 1996; Laue et al., 1996) and (ii) its high damage potential.

Ruiz–Agudo et al. (2007) described the occurrence of Na-sulphate crystallisation up to 3 mm under the surface of samples, resulting in flaking. A decrease in stone porosity was also reported. However, it should be emphasised that the stones analysed in that study were highly porous, with levels of more than 30 %. In this investigation on the other hand, deterioration of the Slovenian limestones was restricted to a much smaller area. This fact could be ascribed to their extremely low porosity of less than 5 % (Kramar et al., 2010a). In addition, due to their high compactness, deterioration was observed only to a depth of around 200 μm below the surface. Deterioration of these limestones could be a result of the crystallisation pressure of thenardite, which ranges from 29.2 to 196.5 MPa (Winkler & Singer, 1972) and exceeds the splitting tensile strengths of the investigated limestones which are not higher than 15 MPa. With repeated cycles of salt crystallisation,

hydration pressure also develops. The crystallisation pressure of thenardite is higher than that of mirabilite (Winker & Singer, 1972), resulting in greater damage. The transition of mirabilite to thenardite is also accompanied by an increase in volume of 300 % (Price & Brimblecombe, 1994).

One factor which could have influenced the smaller amount of stone deterioration caused by the frost resistance test could be the lower pressures which occur during ice formation with respect to salt crystallisation. Pressure caused by the former ranges from 14 to 138 MPa with a decrease in temperature of between –1.1 and –12.5 °C (Goudie & Viles, 1997). During the ageing test performed in this study, the temperature fell by up to –10 °C. The temperature range considered critical for the deterioration of natural stone is from about –4 to –15 °C (Goudie & Viles, 1997). Stone with a higher quantity of smaller pores is more prone to frost deterioration as well as salt crystallisation, although stone damage is more specifically influenced by nanopores in the case of salt crystallisation and by micropores in the case of frost damage (Lindquist et al., 2007). Since the investigated limestones have low capillary kinetics (Kramar et al., 2010a), they can be considered as more prone to frost damage, as slow water transfer may prevent water movement, resulting in higher pressures (Thomachot & Matsouka, 2007).

Conclusions

The limestones investigated in this study were recognised as high strength rocks. The highest strength was observed in the grey lithotype of the Lesno Brdo limestone, followed by Drenov Grič limestone and the red Lesno Brdo lithotype, which suggests that the higher the content of phillosilicate-filled discontinuities, the lower the splitting tensile strength. There were no significant differences observed between the bedding planes of different orientations in the Drenov Grič limestone. Furthermore, there was also no difference in observed tensile strength between the dry and water-saturated samples.

There were, however, measurable differences in USV values between the studied limestones. Faster ultrasonic wave propagation was seen in fresh SLB samples, suggesting a greater compactness and mechanical resistance than the PLB and DG samples. In contrast, total structural anisotropy (ΔM) and relative structural anisotropy (Δm) were lower in SLB than PLB samples.

After ageing tests were carried out, some changes in microstructure occurred, as observed via SEM-EDS examination and USV measurement. Deterioration of the studied limestones took place in the form of granular disintegration, fissuring and flaking. A much higher level of damage was apparent

after the salt crystallisation test than the frost resistance test, with the area damaged area also larger. Deterioration was slightly higher in the Drenov Grič and thus this limestone can be considered as more prone to deterioration than either Lesno Brdo lithotype. Of the two lithotypes of Lesno Brdo limestone, the grey lithotype possessed better durability characteristics. In general, the durability of the studied limestones is mostly affected by their porosity and the presence of phyllosilicate-filled discontinuities.

Acknowledgements

This research has been supported financially by the Slovenian Research Agency, under contract number 3211-05-000545. The Slovenian National Building and Civil Engineering Institute is gratefully acknowledged for providing experimental support, while the authors would also like to thank Mr. Janko Čretnik for performing the ageing tests.

References

Arnold, A., Zehnder, K. (1988): Decay of stony materials by salts in humid atmosphere. In: *Proceedings, 6th International Congress on the Deterioration and Conservation of Stone*. Torun: Nicolas Copernicus University Press Department, 138–148.

Bell, F. G. (1992): *Engineering in Rock Masses*. Oxford : Butterworth-Heinemann, 580 p.

Benavente, D., García del Cura, M. A., Fort, R., Ordóñez, S. (1999): Thermodinamic modelling of changes induced by salt pressure crystallisation in porous media of stone. *Journal of Crystal Growth*, 204, 168–178.

Benavente, D., García del Cura, M. A., Bernabéu, A., Ordóñez, S. (2001): Quantification of salt weathering in porous stone using an experimental continuous partial immersion method. *Engineering geology*, 59, 313–325.

Benavente, D., García del Cura, M. A., García-guinea, J., Sánchez-moral, S., Ordóñez, S. (2004): Role of pore structure in salt crystallization in unsaturated porous stone. *Journal of Crystal Growth*, 260, 532–544.

Benavente, D., Martínez-Martínez, J., Cueto, N., García del Cura, M. A. (2007): Salt weathering in dual-porosity building dolostones. *Engineering geology*, 94, 215–226.

Bouineau, A. (1978): *L´interet des essais non-destructifs utilises pour l´etude de la restauration des monuments et sculptures. Alteration et protection des monuments en pierres*. Pariz: RILEM, 1–29.

Brard (1828): On the method proposed by Mr Brard for the imediate detection of stone unable to resist the action of frost. *Héricrt de Thury:*

Annales de Chemie et de Physique, 38, 160–192.

Bromblet, P. (1993): Relations entre les variations des conditions environmentales et les processus de dégradation successive des temples de Karnak (Egypt). In: *Conservation of Stone and Other Materials* (ed. M.J. Thiel). London : Spon, 91–98.

Cardell, C., Benavente, D., Rodríguez-Gordillo, J. (2008): Weathering of limestone building material by mixed sulfate solutions. Characterization of stone microstructure, reaction products and decay forms. *Materials characterization*, 59, 1371–1385.

Charola, E. A. (2000): Salts in the deterioration of porous materials: an overview. *Journal of the Institute of American Conservators,* 39, 327–343.

Cultrone, G., Russo, L. G., Calabró, C., Urosevic, M., Pezzino, A. (2008): Influence of pore system characteristics on limestone vulnerability: a laboratory study. *Environmental Geology*, 54, 1271–1281

Doehne, E. (2002): Salt weathering: a selective review. In: *Natural stone, weathering phenomena, conservation strategies and case studies* (eds. S. Siegesmund, T. Weiss, A. Vollbrecht). London: Geological Society, Special Publication, 205, 51–64.

Evans, I. S. (1970): Salt crystallization and rock weathering: A review. *Revue Géomorphologie Dynamique,* 19, 153–177.

Fahey, B. D. (1986): A comparative laboratory study of salt crystallization and salt hydration as potential weathering agents in deserts. *Geogr Ann Ser A: Phys Geogr*, 68, 107–111.

Fassina, V., Rosseti, M., Fumo, G., Zezza, F., Macri, F. (1993): The marble decay of Pilastri Acritani and problems of conservation. In: *Conservation of stone and other Materials* (ed. M.J. Thiel). Proceedings of the International RILEM/UNESCO congress, Paris, 75–82.

Fassina, V., Arbizzani, R., Naccari, A. (1996): Salt efflorescence on the marble slabs of S. Maria dei Miracoli Church: A Survey on their origin and on the methodology of their removal. In. Proccedings, 8th International Congress on Deterioration and Conservation of Stone, (ed. J., Reiderer). Berlin: Ernst und Sohn, 523–534.

Flatt, R. J. (2002): Salt damage in porous materials: how high supersaturations are generated. *Journal of Crystal Growth*, 242, 435–454.

Goudie, A., Viles, H. (1997): *Salt weathering hazards.* Chichester: J. Wiley and Sons, 235 p.

Guydader, J., Denis, J. A. (1986): Propagation des ondes dans les roches anisotropes sous contrainte évaluation de la qualité des schistes ardoisiers. *Bulletin of the Engineering Geology*, 33, 49–55.

Jarc, S. (2000): *Vrednotenje kemične in mineralne sestave apnencev kot naravnega kamna*, Masters Thesis, University of Ljubljana, Fac-

ulty of Natural Sciences and Engineering, Department of Geology, Ljubljana.

KRAMAR, S., MLADENOVIĆ, A., UROSEVIC, M., MAUKO, A., PRISTACZ, H., MIRTIČ, B. (2010): Deterioration of Lesno Brdo limestone on monuments (Ljubljana, Slovenia) = Propadanje lesnobrdskega apnenca na objektih kulturne dediščine (Ljubljana, Slovenia). *RMZ - mater. geoenviron.*, 2010a: 57, 53–73.

KRAMAR, S., UROSEVIC, M., PRISTACZ, H., MIRTIČ, B. (2010): Assessment of limestone deterioration due to salt formation by micro-Raman spectroscopy: application to architectural heritage. *Journal of Raman spectroscopy*, 2010b, in press, doi: 10.1002/jrs.2700.

KWAAD, F. J. P. M. (1970): Experiments on the granular disintegration of granite by salt action. *Fys Georg en odemkundig Lab 16*, 67–80. Amsterdam University.

LAUE, S., BLÄUER-BÖHM, C., JEANETTE, D. (1996): Salt weathering and porosity-examples from the Crypt of St. Maria in Kapitol, Cologne, In: *Proceedings, 8th International Congress on Deterioration and Conservation of Stone* (ed. J. Reiderer). Berlin: Ernst und Sohn, 513–522.

LINDQUIST, J. E., MALAGA, K., MIDDENDORF, B., SAVUKOSKI, M., PÉTURSSON, P. (2007): *Frost resistance of Natural stone, the importance of micro- and nano-porosity*. Geological Survey of Sweden External research project report, published online at: http://www.sgu.se/dokument/fou_extern/Lindqvist-et-al_2007.pdf.

MARCHNER, H. (1978): Application of salt crystallization test to impregnated stones. V *Symposium on Deterioration and Protection of Stone Monuments*, Paris: UNESCO-RILEM, 16 p.

MIRTIČ, B., MLADENOVIĆ, A., RAMOVŠ, A., SENEGAČNIK, A., VESEL, J., VIŽINTIN, N. (1999): *Slovenski naravni kamen*. Ljubljana: Geological Survey of Slovenia, 131 p.

PAPIDA, S., MURPHY, W., MAY, E. (2000): The use of sound velocity determination for the non-destructive estimation of physical and microbial weathering of limestones and dolomites. In: *Proceedings, 9th International Congress on Deterioration and Conservation of Stone* (ed. V. Fassina). Venice: Elsevier Science, 609–617.

PRICE, C., BRIMBLECOMBE, P. (1994): Preventing salt damage in porous materials. In: *Preprints of the Contributions to the Ottawa Congress, Preventive conservation-Practise, Theory and Research* (eds. A. Roy, P. Smith). London: IIC, 90–93.

RAMOVŠ, A. (2000): *Podpeški in črni ter pisani lesnobrdski apnenec skozi čas*. Mineral; Ljubljana, p. 115.

RODRIGUEZ-NAVARRO, C., DOEHNE, E., SEBASTIAN, E. (2000): How does sodium sulfate crystallize? Implications for the decay and testing of building materials. *Cement and Concrete Research*, 30, 1527–1534.

Rothert, E., Eggers, T., Cassar, J., Ruedrich, J., Fitzner, Siegesmund, S. (2007): Stone properties and weathering indiced by salt crystallization of Maltese Globigerina Limestone. In: *Building stone decay: From diagnosis to conservation* (eds. R. Přikryl, B. J. Smith). London: Geological Society, Special Publications, 271, 189–198.

Ruiz-Agudo, E., Mees, F., Jacobs, P., Rodriguez-Navarro, C. (2007): The role of saline solution properties on porous limestone salt weathering by magnesium and sodium sulfates. *Environmental Geology,* 52, 269.

Schaffer, R. J. (1932): *The weathering of Natural Building Stones*. DSIR, Building Research Special Report No. 18. London: HMSO, 34 p.

Sperling, C. H. B., Cooke, R. U. (1985): Laboratory simulation of rock weathering by salt crystallization and hydration processes in hot, arid environments. *Earth Surface Processes Landforms*, 10 541–555.

Thomachot, C., Matsouka, N. (2007): Dilation of building materials submitted to frost action. In: *Building stone decay: From diagnosis to conservation* (eds. R. Přikryl, B. J. Smith). London: Geological Society, Special Publications, 271, 167–177.

Tuncoku, S. S., Calner-Saltik, E. N., Böke, H. (1993): Definition of the material and related problems of a XIIIth century Anatolian Seljuk »Mescid«: a case study in Konya City. In: *Conservation of Stone and other Materials* (ed. M.J. Thiel). London: Spon, 368–375.

Warke, P. A., McKinley, J., Smith, B. J. (2006): Weathering of building stone: approaches to assessment, prediction and modelling. In: *Fracture and Failure of Natural Building Stones* (ed. S. K. Kourkoulis). Dorddrecht: Springer; 313–327.

Winkler, E. M., Singer, P. C. (1972): Crystallization pressure of salt in stone and concrete. *Geological Society of America Bulletin*, 83, 3509–3513.

Zezza, U. & Vienale, F. (1988): Ultrasonic investigations on quarry- and freestones of historical monuments in Lombardy, Italy. V *Proceedings of the Vth International Congress on Deterioration and Conservation of Stone.* Lausanne: Presses Polytechniques Romandes, vol. 2, p. 303–312.

Standards:

ASTM C88-90, Standard test method for soundness of aggregate by use of sodum sulfate or magnesium sulfate, Annu Book ASTM Stand 4.2., 1997, 37–42.

RILEM PEM/25, Essais recomndees pour l´alteration des pierres et evaluer l´efficacite des methodes de traitement, Mater constr 17, 1980, 216–220.

SIST EN 12390-6:2001: Preskušanje strjenega betona - 6. del: Natezna razcepna trdnost preskušancev.

SIST EN 12370:2000: Preskušanje nara-

vnega kamna - Ugotavljanje odpornosti proti kristalizaciji soli.
SIST EN 12371:2002: Preskušanje naravnega kamna - Ugotavljanje odpornosti proti zmrzovanju.
SIST EN 14579:2004: Preskušanje naravnega kamna - Ugotavljanje hitrosti širjenja zvoka.
SIST EN 1936:2000: Ugotavljanje prostorninske mase brez por in votlin in prostorninske mase s porami in votlinami ter skupne in odprte poroznosti.

Status of salinity in aquifers of Ghataprabha Command Area, Karnataka, India

Slanostne razmere v vodonosnikih upravljalnega območja Ghataprabha v Karnataki (Indija)

N. Varadarajan[1,*], B. K. Purandara[1], Bhism Kumar[2]

[1]National Institute of Hydrology, Belgaum – 590001, Karnataka, India
[2]National Institute of Hydrology, Roorkee – 247667, Uttaranchal, India

*Corresponding author. E-mail: nvarad@yahoo.com

Received: July 27, 2009 **Accepted:** October 5, 2009

Abstract: The present study aims to understand the salinity status of Gokak, Mudhol, Biligi and Bagalkot taluks of Ghataprabha command area, Karnataka, India. The command area falls under semi-arid and drought hit areas. The samples were collected from 25 open wells and 41 bore wells during pre-monsoon and post-monsoon of the year 2007. From the chemical analysis, the open well shows more EC than deep bore wells. The EC is a useful parameter for indicating salinity hazard. In the present study area the EC values varies between 280 μS/cm and 6500 μS/cm during pre-monsoon and 290 μS/cm and 9020 μS/cm during post-monsoon. As per the classification of natural water based on EC concentration clearly shows that, water belongs to medium salinity to very high salinity. The factor analysis was carried out for both the seasons. The set of first five factors for pre-monsoon and first six factors for post-monsoon were identified for further analysis. The factor 1 of both pre-monsoon and post-monsoon seasons shows 38.70 % and 33.35 % variance with high positive loadings of EC, Na, Mg, Cl, Ca, and SO_4 as representing salinity that could be due to combination of various hydrogeochemical processes that contribute more mineralized water, rock weathering and agricultural activities.

Povzetek: Ta študija je namenjena razumevanju slanostnih razmer v talukih Gokak, Mudhol, Biligi in Bagalkot v upravljalnem območju Ghataprabha v Karnataki v Indiji. Omenjeno območje leži v semi-

Original scientific paper

aridnih in sušnih področjih. Vzorci so bili zbrani iz 25 odprtih vodnjakov in 41 vrtin v pred- in pomonsunskem obdobju v letu 2007. Iz geokemičnih analiz je razvidno, da imajo vode iz odprtih vodnjakov višjo elektroprevodnost (EC) kot iz globljih vrtin. EC je uporaben parameter za ugotavljanje povišane slanosti. V predstavljeni študiji se vrednosti EC gibljejo med 280 µS/cm in 6500 µS/cm v predmonsunski in med 290 µS/cm in 9020 µS/cm v pomonsunski dobi. Razvrstitev naravnih vod glede na koncentracijo EC kaže, da imajo vode slanost od srednje stopnje do zelo visoke. Za obe obdobji je bila napravljena faktorska analiza. Za nadaljnje analize je bil izbran nabor prvih pet faktorjev za predmonsunsko in prvih šest faktorjev za pomonsunsko obdobje. Faktor 1 za obe obdobji (pred- in pomonsunsko) kaže 38,70-odstotno in 33,35-odstotno varianco z visoko pozitivno obremenjenimi spremenljivkami EC, Na, Mg, Cl, Ca in SO_4, kar kaže na slanost, ki je lahko posledica kombinacije različnih hidrogeokemičnih procesov, ki zajemajo bolj mineralizirane vode, preperevanje kamnin in agrikulturne dejavnosti.

Key words: salinity, EC, factor analysis, weathering, agricultural activities
Ključne besede: slanost, EC, faktorska analiza, preperevanje, agrikulturne dejavnosti

INTRODUCTION

Groundwater is becoming an important source of water supply in many regions due to rapid growth of population, which is placing an increasing demand upon fresh water supplies. Water logging is a common feature associated with many of the irrigation commands leading to rise in the water table. The irrigation command areas are recharged not only by the rainfall infiltration, but also by seepage from reservoirs, canals, distributaries and field channels and return circulation of irrigation water. The rising salinity of groundwater used for water supply and irrigation is a major problem. The impact of various management activities on groundwater quality is closely related with the quality of water applied for irrigation. Fertilizers are normally applied to agricultural fields to increase the crop yields. However, a part of the chemical constituents present in the fertilizer may percolate down to reach the ground water table thereby polluting the fresh water aquifers.

Central Ground Water Board, (1997) carried out studies on Conjunctive use of surface and groundwater of Ghataprabha irrigation command and chemical analysis of the water samples

of shallow wells which indicated pockets of salinity in certain parts of the command area. The study carried out by Water and Power Consultancy Services Limited (1997) on reclamation of affected areas in Ghataprabha irrigation projects, reported water logging and salinity problems in Kalloli, Yedahalli and Bisnal villages of the command. The remedial measures such as proper drainage plans, control of seepage in canals, cropping patterns and conjunctive use of surface and groundwater were also suggested. Purandara et al., (1996) carried out a study on optimal use of land and water resources in Ghataprabha command and suggested proper cropping pattern to control water logging. Purandara et al., (1997) carried out a study on water logging problems in canal commands of hard rock region of Ghataprabha command and highlighted the problems of water logging and salinity in the selected patches of the command area. Further studies were carried out to estimate the solute transport characteristics in different types of soils, particularly in salinity affected soils of Biligi and Bagalkot taluks of Ghataprabha command by using SWIM (Soil Water Infiltration and Movement) and VLEACH (Vadose Zone Leaching) models (Purandara et al, 2002).

Durbude et.al, (2002) analyzed groundwater characters of Ghataprabha command under GIS environment and reported the acute problem of ground water salinity. The NIH, Roorkee and Remote sensing directorate, Central Water Commission, New Delhi also carried out a study of Ghataprabha Command area using remote sensing and GIS (2003) and delineated the water logged and salt affected areas in the command. They estimated the total water logged area as 1 %. It is also reported that the salt affected area is distributed in the command area during premonsoon season is about 5.5 %. According to the study water logging is more in Bijapur than in Belgaum district. Hiremath (2005) carried out a study on water logging and salinity and impact of major irrigation projects on agriculture land and reclamation of affected areas in Bagalkot and Biligi taluks of Ghataprabha command area. Based on the study, it is suggested that the problem of rising of water table may be achieved by adopting conjunctive use of surface and groundwater by providing proper drainage and following appropriate cropping pattern.

The command area of Ghataprabha reservoir is located between 16°0’8” N–16°48’9” N latitudes and 74°26’43” E–75°56’33” E longitudes covering an area of 317,430 hectares covering parts of Belgaum and Bijapur districts of Karnataka. The index map of the study area is shown in Figure 1. The study area is bound by the Krishna River in the north, Maharashtra state to the west,

the confluence of Krishna River and Malaprabha River in the east and the basin boundary between Ghataprabha and Malaprabha rivers in the south. The existing canal command area (net command area is 161,871 ha) is served by the Ghataprabha Left Bank Canal and six branch canals with a number of major and minor distributaries. The proposed right bank canal is expected to irrigate an area of about 155,000 ha.

The topography of the area is undulating with table lands and hillocks typical of Deccan trap. General topographic elevation varies between 500

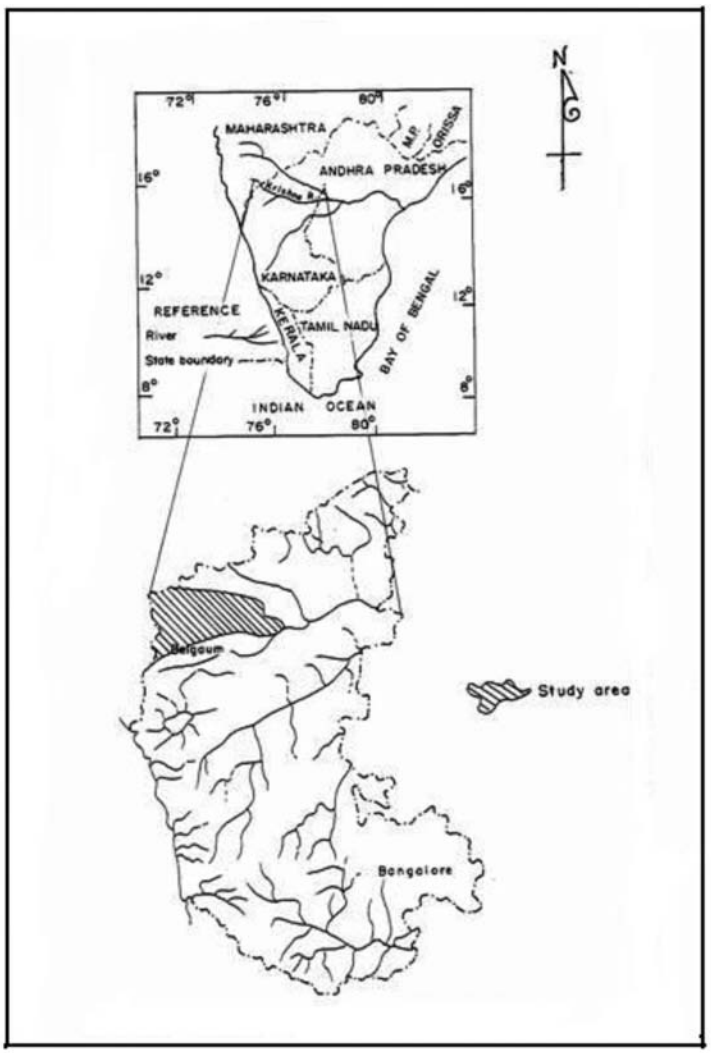

Figure 1. Index map of the Study Area

m to 900 m above msl with a gradual fall from West to East. The catchment boundary between rivers Krishna and Ghataprabha follows the Ghataprabha Left Bank Canal up to Biligi. The command area essentially lies within the Krishna river basin and is drained by the Ghataprabha River. Ghataprabha River is one of the right bank tributary of the river Krishna in its upper reaches. The river originates from the Western Ghats in Maharashtra at an altitude of 884 m and flows westwards for about 60 km through the Ratnagiri and Kolhapur districts of Maharashtra. In Karnataka, the river flows for about 216 km through Belgaum district.

The command area falls in the semi-arid zone and falls under drought hit areas. Average annual rainfall is about 700 mm with wide variation in time and space. The command area is underlain predominantly by sedimentary rocks of Deccan trap. Soils in the left bank canal command area are rich in clay and bases due to hydrolysis, oxidation and carbonation. However soils in the right bank canal command area is developed due to weathering of sedimentary rocks. Soils in the area can be classified based on the geological formations. Soil depth varies from 25 cm to 30 cm in the case of shallow soils with high permeability. Deep soils with dark grey colour are found between 45 cm to 90 cm depth. Black cotton soils with an average pH of 8–8.5 generally occupy the low-lying areas. These soils exhibit high water holding capacity but poor permeability.

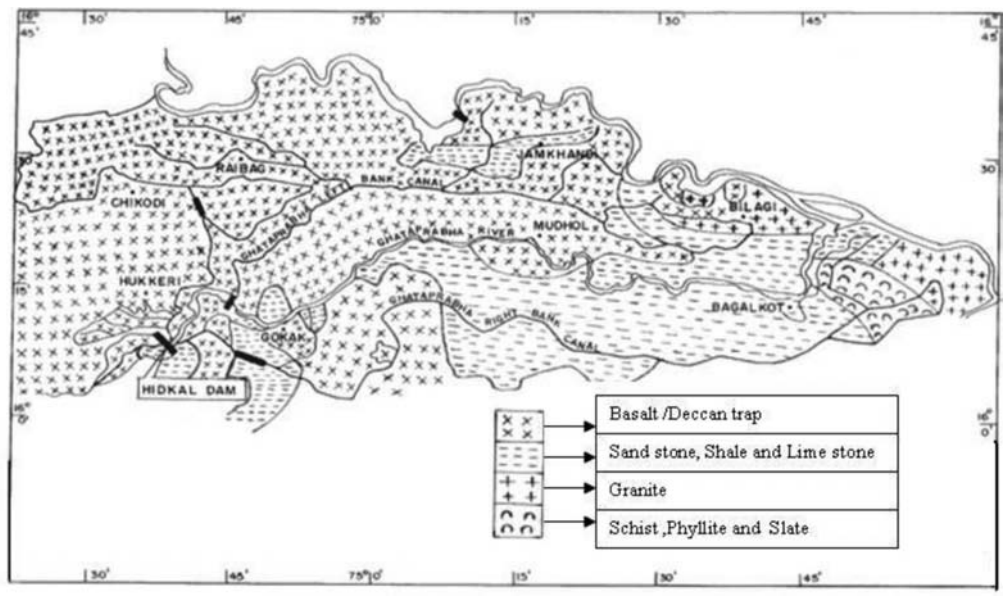

Figure 2. Hydrogeological map of Ghataprabha Command Area

The hydrogeology is complex, as Deccan traps occupy major portions of the study area (CGWB, 1997). The hydrogeological map of the Ghataprabha Command area is shown in Figure 2. River alluvium is found only along the course of rivers. Groundwater occurs in the weathered and fractured hard rocks as well as in the vesicular horizons in the traps. Unconfined to semi confined conditions are observed in weathered/ semi weathered rocks. Confined conditions can be encountered when the fractures are deep seated or in vesicular horizons underlain by massive traps.

MATERIALS AND METHODS

The area selected for the proposed study is left and right bank canal commands of Gokak, Mudhol, Biligi and Bagalkot taluks of Ghataprabha irrigation command. Major classification for sampling is based on reconnaissance survey and also based on interaction held with farmers. To achieve the objectives of the study samples were collected from both open shallow and deep bore wells including hand pumps, which are being extensively used for agricultural, drinking and other domestic purposes. The samples were collected from 25 open wells and 41 bore wells. Location of these wells is shown in Figure 3.

The depth of open wells from where samples being collected are from 6.00 m to 25.00 m and bore wells from 25.00 m to 122.00 m. The samples were collected

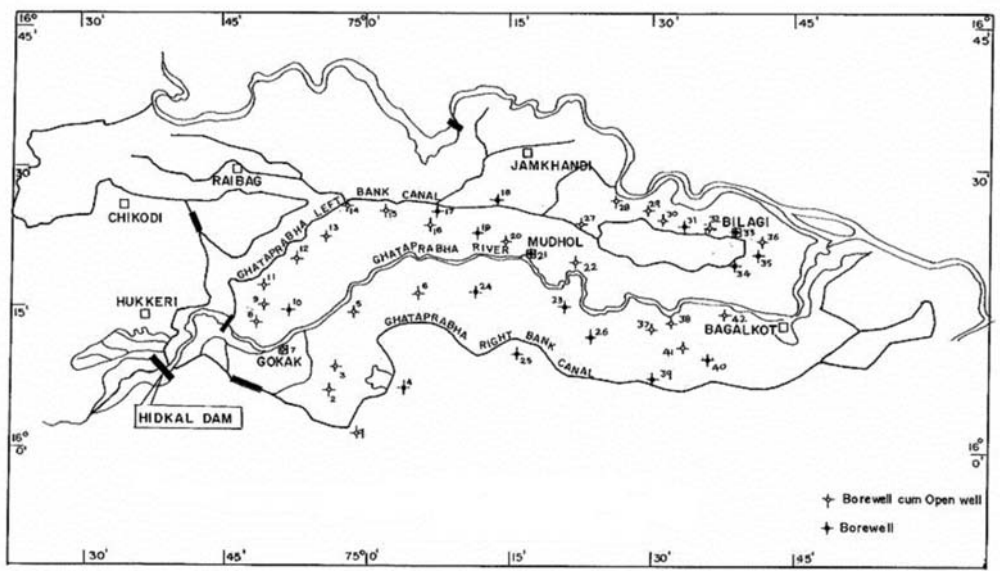

Figure 3. Location map of Groundwater sampling stations

by grab sampling method during pre-monsoon and post-monsoon of the year 2007. In this method a sample collected at a particular time and place can represent only composition of the source at that time and place. Depth integrated samples were collected by lowering the container in the open wells. Depth to water levels and total depth were measured for open wells and only total depth was measured for bore wells. The chemical parameters of the samples were analyzed in the laboratory by standard methods recommended in the manuals (APHA). In the present study the chemical parameters were analyzed are pH, Electrical Conductivity (EC), TDS, Temperature, carbonate, bicarbonate, alkalinity, chloride, sulphate, total hardness calcium, magnesium, sodium, potassium, phosphate, nitrate, fluoride and iron.

In the present study, the basic statistical analysis of the chemical parameters was done by using SYSTATW5 software package. The effect of salinity is one of the most important water quality considerations for agricultural purposes. Generally, salinity is measured in terms of Electrical Conductivity concentration. The EC is a useful parameter of water quality for indicating salinity hazards. The total salinity is a measure of the concentration of salts in water and as such is related to the usability of water for irrigation of crops. Water used for irrigation always contains some amounts of dissolved substances; in general they are called salts. The salts present in the water, besides affecting the growth of the plants, also affect the soil structure, permeability and aeration, which indirectly affect the plant growth. Based on EC and TDS in natural water, the classification of salinity of water (Jain et al. 1997) shown in Table 1.

Factor analysis is a technique of quantitative multivariate analysis with the goal of representing the inter-relationship among a set of variables or objects. Factor analysis gives a simple interpretation of a given body of data and affords fundamental description of particular set of variables related to hydro chemical processes beyond strict litho logical controls (Lawrence & Upchurch, 1982). Factors are con-

Table 1. Classification of Salinity of Natural Water (Richards, 1954)

Zone	Electrical Conductivity (μS/cm)	Total Dissolved Salts (mg/L)
Low Salinity Zone	< 250	< 200
Medium Salinity Zone	250–750	200–500
High Salinity Zone	750–2250	500–1500
Very High Salinity Zone	2250–5000	1500–3000

structed in such a way that they reduce the overall complexity of the data by taking advantage of inherent interdependencies. To reduce the data to an easily interpretable form, factor analysis was undertaken using the routine Factor of DAVIS (1973). Prior to the analysis, the data were standardized according to criteria presented by DAVIS (1973). This is necessary since the first step in factor analysis is computation of a correlation coefficient matrix, which requires normal distribution of all variables (LAWRENCE & UPCHURCH, 1982). The correlation matrix gives the inter-correlation among the set of variables. The Eigen value has been computed for all the principal axes. The Eigen values are helpful in deciding the number of components required to explain the variation in data.

The factor extraction has been done with a minimum acceptable eigen value as greater than 1 (KAISER, 1958; HARMAN, 1960). The factor loading matrix is rotated to an orthogonal simple structure, according to varimax rotation, which results in the maximization of the variance of the factor loading of the variables. The objective of varimax rotation is moving of each factor axis to positions so that projections from each variable on to the factor axes are either near the extremities or near the origin. Factor loading is the measure of the degree of closeness between the variables and the factor. The largest loading, either positive or negative, suggests the variance of the factor loading of the variables; positive loading indicates that the contribution of the variables increases with the increasing loading in a dimension; and negative loading indicates a decrease (LAWRENCE & UPCHURCH, 1982). The R – mode factor analysis provides several positive features that allow interpretation of the data set.

RESULTS AND DISCUSSION

The summary statistics of the chemical parameters for pre-monsoon and post-monsoon seasons of the year 2007 are presented in the Table 2 & 3. The EC is a useful parameter of water quality for indicating salinity hazards. In the present study area, the EC values varies between 280 μS/cm and 6500 μS/cm during pre-monsoon and 290 μS/cm and 9020 μS/cm during post-monsoon. The variation of EC values for both the seasons are shown in Figure 4 & 5. It is observed that waters of high EC values are predominant with sodium and chloride ions. In the present study, the sodium varies from 16.00 mg/L to 680 mg/L during pre-monsoon and from 32.00 mg/L to 550 mg/L during post-monsoon. Soils in the left bank canal

command area are rich in clay and bases due to hydrolysis, oxidation and carbonation. Under suitable conditions clay minerals may release exchangeable sodium ions. This causes higher concentration of sodium in areas where clays are found. The chloride content of groundwater may be due to the presence of soluble chlorides from rocks. It is observed that concentration of chloride varies from 17.70 mg/L to 1348.90 mg/L during pre-monsoon and from 30 mg/L to 1960 mg/L during post-monsoon. Further, chloride is a common element distributed in some types of rocks in one or the other form. Its affinity towards sodium is high. Therefore, its concentration is high in groundwater's where the temperature is high and rainfall is less. Soil porosity and permeability also has a key role in building up the chloride concentration.

Table 2. Statistical summary of Chemical parameters May 2007 (Pre-monsoon)

Parameter	Units	Minimum		Maximum		Mean		Std. dev.		Range	
		BW	OW	BW	OW	BW	OW	BW	OW	BW	OW
pH	-	6.90	7.16	7.85	8.20	7.29	7.50	0.22	0.23	0.95	1.04
EC	µS/cm @25˚C	460	280	5740	6500	1809	2692	1160	2058	5280	6220
TDS	mg/L	300	170	3810	4270	1167	1749	763	1341	3510	4100
Hardness	mg/L	50	70	750	760	239	253	151	194	700	690
Carbonate	mg/L	0.00	0.00	22	40	2.36	3.80	5.28	10.50	22	40
Bicarbonate	mg/L	146	61.00	545	585	292	354	109	141	399	524
Alkalinity	mg/L	150	61.00	562	605	294	357	110	145	412	544
Chloride	mg/L	17.72	23.00	1349	892	220	327	252	335	1331	869
Sulphate	mg/L	6.00	8.00	110	100	56	54	26	30	104	92
Calcium	mg/L	12	20.80	115	111	47	47	26	28	103	90
Magnesium	mg/L	2	3.90	113	117	30	35	24	32	111	114
Sodium	mg/L	28	16.00	650	680	165	248	136	199	622	664
Potassium	mg/L	0.50	1.00	180	205	24	27	44	54	179	204
Nitrate	mg/L	1.00	1.00	19	20	5.80	5.40	3.67	4.70	18	19
Iron	mg/L	0.20	0.30	2.00	3.00	0.45	0.67	0.33	0.72	1.80	2.70
Phosphate	mg/L	0.00	0.00	0.35	1.25	0.025	0.17	0.07	0.37	0.35	1.25
Fluoride	mg/L	0.70	0.80	1.65	1.55	1.08	0.95	0.18	0.19	0.95	0.8

Table 3. Statistical summary of Chemical parameters Nov. 2007 (Post-monsoon)

Parameter	Units	Minimum		Maximum		Mean		Std. dev.		Range	
		BW	OW	BW	OW	BW	OW	BW	OW	BW	OW
pH	-	6.65	7.05	7.95	8.15	7.27	7.54	0.27	0.27	1.30	1.10
EC	µS/cm @25˚C	360	290	9020	6650	1669	2027	1528	1654	8660	6360
TDS	mg/L	230	180	6150	3900	1113	1318	1041	1034	5920	3720
Hardness	mg/L	78	108	2220	554	289	235	339	112	2142	446
Carbonate	mg/L	0.00	0.00	24	30	1.76	2.42	5.32	6.70	24	30
Bicarbonate	mg/L	165	110	512	542	290	313	89	115	347	432
Alkalinity	mg/L	165	110	512	542	291	315	90	117	347	432
Chloride	mg/L	30	30	1960	975	222	231	333	247	1930	945
Sulphate	mg/L	19	10	220	190	57	68	36	40	201	180
Calcium	mg/L	12.80	20	528	96	63	46	81	21	515	76
Magnesium	mg/L	6.70	10.60	215	80	32	29	34	17	208	69
Sodium	mg/L	41.00	32	398	550	158	191	102	141	357	518
Potassium	mg/L	1.00	2.00	205	110	17	20	36	26	204	108
Nitrate	mg/L	2.50	3.00	20.50	20.90	10.50	9.70	5.40	5.80	18	17.90
Iron	mg/L	0.30	0.4	2.00	3.00	0.83	0.84	0.44	0.56	1.70	2.60
Phosphate	mg/L	0.00	0.00	0.75	4.00	0.066	0.36	0.16	0.85	0.75	4.00
Fluoride	mg/L	0.80	0.60	1.45	1.10	1.08	0.92	0.14	0.11	0.65	0.50

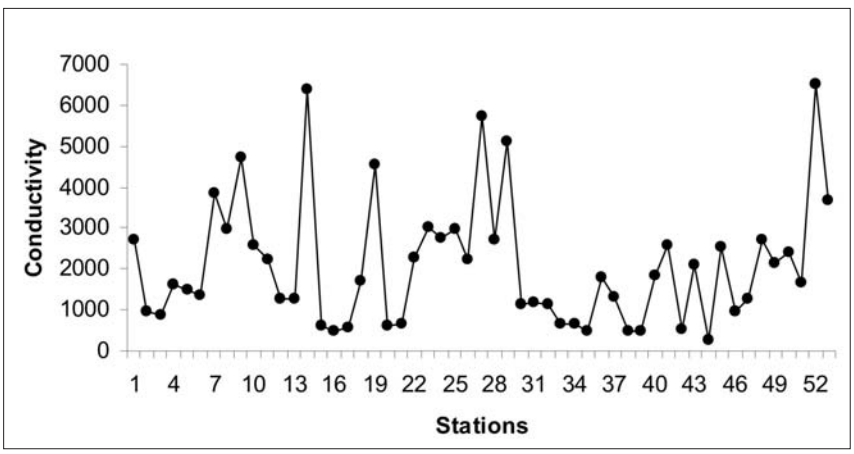

Figure 4. Distribution of EC for May 2007

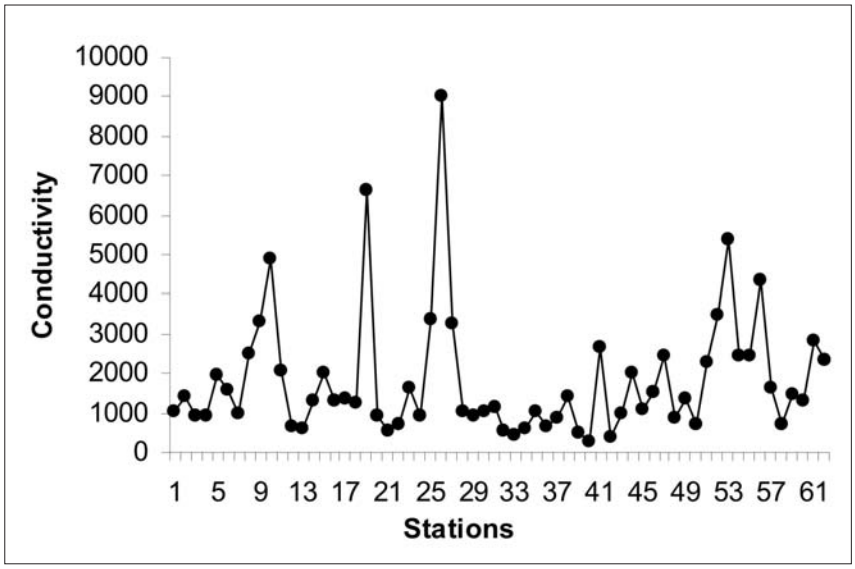

Figure 5. Distribution of EC for November 2007

Table 4. Percentage classification of salinity in wells

Zone	Pre-monsoon	Post-monsoon
Low Salinity Zone	-	-
Medium Salinity Zone	23 %	21 %
High Salinity Zone	35 %	52 %
Very High Salinity Zone	42 %	27 %

The TDS value varies between 170 mg/L and 4270 mg/L during pre-monsoon and 180 mg/L and 6150 mg/L during post-monsoon. The higher values are observed for post-monsoon samples. This indicates the effect of overland flow. From the chemical analysis, the open well shows more EC than deep bore wells and it indicates open wells are more saline than bore wells. Among the anions the dominating ions are bicarbonate and chloride and in the case cations sodium is dominating the other ions as Na > Ca > Mg > K. The classification of natural water based on EC concentration clearly shows that, water of medium to very high salinity zone. Based on the concentration of EC, the results of percentage classification of wells in the study area are shown in Table 4.

The groundwater quality data showed that there is a considerable quality variation in the study area. There is an increase in the Electrical Conductivity

and chloride concentration particularly in open wells. This is attributed to the local conditions such as irrigation return flow and excessive agricultural activities. The non-systematic increase of high salinity zone during post-monsoon is basically due to two reasons. The Biligi taluk in the study area is covered by low permeable clayey soils and rainfall is less than 600 mm. Therefore due to rainfall infiltration the top saline soils are leached into open wells due to which an increase in salinity was noticed during post-monsoon.

Factor Analysis

For pre-monsoon season, the first five factors show eigen value more than 1, thus these five factors were chosen for further analysis. Factor 1 of the pre-monsoon season shows 38.70 % variance. This factor has high positive loadings and strongly associated with EC and ions such as Mg, Cl, Na, Ca, and SO_4. These ions contribute more salinity to the water. This factor may therefore be salinity factor and indicates saline water in the study area. Factor 2 of pre-monsoon season shows 14.60 % variance. This factor has high loading and strongly associated with ions CO_3, PO_4, and HCO_3. Factor 3 of pre-monsoon season shows 10.80 % variance. This factor has high loading and strongly associated with ions Potassium and Nitrate. Factor 4 of pre-monsoon season shows 9 % variance. This factor has high positive loading on fluoride indicating possible leaching of soil fluoride and weathering of fluoride bearing rocks. Factor 5 of pre-monsoon season shows 7.10 % variance and there is no significance contribution of any ions.

For post-monsoon season, first six factors show eigen value more than 1, thus these six factors were chosen for further analysis. Factor 1 of the post-monsoon season shows 33.35 % variance and strongly associated with EC, Cl, Ca, Mg, and Na. Factor 2 of the post-monsoon season shows 15.40 % variance. Factor 3 of the post-monsoon season shows 10.20 % variance and strongly associated with SO_4 and PO_4 ions. Factor 4 of the post-monsoon season shows 10.10 % variance and there is no significant contribution of any ions. Factor 5 of the post-monsoon season shows 7.75 % variance and strongly associated with PO_4 and NO_3 ions. Factor 6 of the post-monsoon season shows 6.60 % variance and there is no significant contribution of any ions.

Table 5 and 6 represents the factor loading which were used to measure the correlation between variable and factors. The components with larger variance are more desirable since they give more information about the data. The components with higher loading of hardness and magnesium are 0.936 and 0.920 respectively indicating the source of hardness is through magne-

sium. The concentration of chloride, Electrical Conductivity, TDS and Calcium also showed high positive loading (0.807–0.883). The sodium and sulphate showed a moderate positive loading (0.738–0.744). Based on the factor loading, it is clear that one of the major problems in the study area is the hardness of water which is indicated by highest loading of magnesium with hardness. This is further associated with the higher loading of EC and TDS accompanied by calcium ions. This could be due to the process of salinization taking place due to rock weathering and agricultural activities. Similar case is observed during the post-monsoon, however, with higher loading factors than the pre-monsoon. The grouping of factor 1 could be due to the combination of various hydrogeochemical processes that contribute more mineralized water (high value of EC and TDS).

Table 5. Rotated factor loading matrix (Pre-monsoon, May 2007)

Sl.No.	Parameter	Factor 1	Factor 2	Factor 3	Factor 4	Factor 5
1	pH	–0.366	0.509	0.225	0.250	–0.070
2	EC	0.877	0.125	0.349	0.188	–0.064
3	TDS	0.881	0.122	0.342	0.180	–0.069
4	Carbonate	–0.111	0.790	0.010	–0.039	0.159
5	Bicarbonate	0.474	0.616	–0.092	0.361	–0.360
6	Alkalinity	0.458	0.650	–0.090	0.352	–0.344
7	Chloride	0.883	0.063	0.261	0.181	0.004
8	Sulphate	0.744	–0.263	0.007	0.051	–0.048
9	Hardness	0.936	–0.197	–0.010	–0.045	0.147
10	Calcium	0.807	–0.117	–0.221	–0.025	0.278
11	Magnesium	0.920	–0.154	0.066	–0.094	0.069
12	Sodium	0.738	0.274	0.296	0.397	–0.169
13	Potassium	0.020	0.088	0.886	–0.066	0.102
14	Phosphate	–0.197	0.710	0.001	–0.308	0.115
15	Nitrate	0.361	–0.102	0.711	0.030	0.070
16	Iron	–0.165	–0.117	–0.150	–0.157	–0.854
17	Fluoride	0.065	–0.063	–0.042	0.907	0.163
Eigen Value		7.031	2.725	1.663	1.162	1.053
Fraction of variance, %		38.70	14.60	10.80	9.00	7.10
Cumulative fraction of variance, %		38.70	53.30	64.10	73.10	80.2

Table 6. Rotated factor loading matrix (Post-monsoon, Nov. 2007)

Sl.No.	Parameter	Factor 1	Factor 2	Factor 3	Factor 4	Factor 5	Factor 6
1	pH	–0.071	–0.030	0.247	–0.820	–0.057	0.252
2	EC	0.861	0.351	0.211	0.016	0.112	0.056
3	TDS	0.881	0.341	0.202	0.025	0.096	0.035
4	Carbonate	–0.014	0.128	–0.112	–0.798	–0.088	–0.113
5	Bicarbonate	0.103	0.970	0.006	–0.067	0.005	–0.105
6	Alkalinity	0.101	0.965	0.000	–0.112	–0.000	–0.110
7	Chloride	0.927	0.187	0.191	0.057	0.101	0.018
8	Sulphate	0.297	–0.057	0.788	–0.020	0.155	0.125
9	Hardness	0.966	–0.056	–0.079	0.132	0.033	–0.045
10	Calcium	0.944	–0.079	–0.088	0.163	–0.014	0.003
11	Magnesium	0.945	–0.013	–0.059	0.079	0.105	–0.109
12	Sodium	0.560	0.565	0.476	–0.041	0.165	0.058
13	Potassium	0.057	–0.115	0.147	0.053	0.855	–0.238
14	Phosphate	–0.107	0.079	0.769	0.019	–0.126	–0.105
15	Nitrate	0.241	0.274	–0.245	0.041	0.675	0.291
16	Iron	0.078	0.170	0.005	–0.075	0.058	–0.884
17	Fluoride	0.260	–0.073	0.084	0.574	–0.074	0.232
Eigen Value		6.385	2.595	1.635	1.357	1.175	1.053
Fraction of variance, %		33.35	15.40	10.20	10.10	7.75	6.60
Cumulative fraction of variance, %		33.35	48.75	58.95	69.05	76.80	83.40

The factor 2 shows a moderate loading of carbonate and bicarbonate (Alkalinity). Apart from carbonate ions, phosphate also showed higher positive loading (0.710). The enrichment of carbonate and bicarbonate is the result of underlying carbonaceous rocks such as limestone and dolomite. The phosphate is the result of excessive use of fertilizers in the canal command area. The higher loading of the above ions during post-monsoon season also shows the dissolution of carbonate rock during the monsoon season and get enriched in groundwater. Factor 3 shows the loading of potassium (0.886) and nitrate (0.711). This grouping clearly indicates that these processes are associated with anthropogenic disturbances. This is further indicated by the post-monsoon analysis which shows a negative loading of nitrate. Due to the rainfall recharge there could be flushing of nitrate ions out of the monitoring wells. The loadings of factor 5 and 6 during post-monsoon also an indication of different sources for potassium and nitrates.

Conclusions

Groundwater quality analysis of Ghataprabha command shows that water is highly saline both during pre-monsoon and post-monsoon. However, the salinity is confined to certain patches of the study area particularly in parts of Gokak and Biligi taluks. Excessive salinity zones are also reported from Mudhol and Jamkhandi taluks. In the present study area the EC values widely varies between 280 μS/cm and 6500 μS/cm during pre-monsoon and 290 μS/cm and 9020 μS/cm during post-monsoon. It is observed that waters of high EC values are predominant with sodium and chloride ions. From the chemical analysis, the open well shows more EC than deep bore wells and it indicates open wells are more saline than bore wells. As per the classification of natural water based on EC concentration clearly shows that, water belongs to medium salinity to very high salinity. It is also observed that the open wells are highly prone to salinity hazards due to the leaching of chemicals through the overlying soil layers.

The problem of salinity hazard is further substantiated through factor analysis. Based on the results obtained by the factor analysis, factor 1 of both pre-monsoon and post-monsoon seasons shows 38.70 % and 33.35 % variance with high positive loadings of EC, Na, Mg, Cl, Ca, and SO_4. This indicates that groundwater is affected by salinity factor that could be due to combination of various hydrogeochemical processes that contribute more mineralized water, rock weathering and agricultural activities. The enrichment of carbonate and bicarbonate is the result of underlying carbonaceous rocks such as limestone and dolomite. The higher loading of the above ions during post-monsoon season also shows the dissolution of carbonate rock during the monsoon season and get enriched in groundwater. The phosphate is the result of excessive use of fertilizers in the canal command area. The potassium and nitrate grouping clearly indicates that these processes are associated with anthropogenic disturbances.

Acknowledgements

The authors acknowledge the National Institute of Hydrology for carrying out this study as a part of doctoral programme and providing laboratory facilities at Regional Centre, NIH, Belgaum. The first author is thankful to the Director, National Institute of Hydrology, Roorkee, India for granting permission to undertake doctoral programme under Visvesvaraya Technological University, Belgaum, India.

References

Central Ground Water Board (CGWB), Ministry of Water Resources, Govt.of India, (1997): Report on

Studies on Conjunctive Use of Surface and Groundwater Resources in Ghataprabha Irrigation Project, Karnataka.

DAVIS, J. C. (1973): Statistics and data analysis in Geology, John Wiley and Sons Inc., New York, pp. 550.

DILIP G. DURBUDE, VARADARAJAN, N. & PURANDARA. B. K. (2002): Mapping of Groundwater Quality Parameters in GIS Environment – Proceedings on International Conference on Hydrology and Watershed Management held at Jawaharlal Nehru Technological University, Hyderabad during 18–20 December, 2002, pp. 568–577.

HARMAN, H. H. (1960): Modern Factor Analysis, University of Chicago Press, Chicago.

HIREMATH, C. B. (2005): Water Logging and Salinity-Impact of Major Irrigation Projects on Agriculture Land and Reclamation of Affected Areas – A case study; M. Tech. Thesis unpublished, Visvesvaraya Technological University, Belgaum.

JAIN, C. K., BHATIA, K. K. S. & VIJAY, T. (1997): Groundwater Quality in a Coastal Region of Andhra Pradesh, Indian Journal of Environmental Health, 39, No. 3, pp. 182–192.

KAISER, H. F. (1958): The varimax criteria for analytical rotation in factor analysis, Psychometrika, 23, pp. 187–200.

LAWRENCE, F. W. & UPCHURCH, B. (1982): Identification of recharge areas using geochemical factor analysis, Ground Water, 20(6), pp. 680–687.

National Institute of Hydrology and Central Water Commission (2003): Study of Ghataprabha Command Area using Remote Sensing and GIS, September 2003.

PURANDARA, B. K., VENKATESH, B. & VARADARAJAN, N. (1996): Optimal use of Land and Water Resources in Ghataprabha command – a case study, proceedings of International Seminar on Disasters and Mitigation Management during 19–22 January, 1996 held at Anna University, Chennai, pp. B3 45– 47.

PURANDARA, B. K., VENKATESH. B. & VARADARAJAN, N. (1997): Water Logging problems in canal commands of Hard Rock region – proceedings of Brain Storming Session on Hydrological problems of Hard Rock Region, organized by Regional Center, NIH at Belgaum on 15th March, 1997.

PURANDARA, B. K, VARADARAJAN, N. & KUMAR, C. P. (2002): Simulation of solute transport in Bagalkot and Biligi taluks of Ghataprabha Command, Technical Report, National Institute of Hydrology, Roorkee.

RICHARDS, L. A. (1954): Diagnosis and improvement of Saline and Alkali Soils, Agric. Handbook 60, U.S. Dept. Agriculture, Washington DC, pp. 160.

Water and Power Consultancy Services (India) Ltd. New Delhi, (1997): Reclamation of Affected Areas in Malaprabha and Ghataprabha Irrigation Projects, Volume.1, Government of Karnataka CADA, M&G Project, August.

Petrochemistry and genetic indicators of talcose rock of Esie area, southwestern Nigeria

Petrokemija in pokazatelji geneze lojevčevih kamnin (skrilavcev) območja Esie, jugozahodna Nigerija

Olorunfemi, A. O.[1], Olarewaju, V. O.[1] & Okunlola, O. A.[2,*]

[1]Department of Geology, Obafemi Awolowo University, Ile-Ife, Nigeria
[2]Department of Geology, University of Ibadan, Ibadan, Nigeria

*Corresponding author. E-mail: gbengaokunlola@yahoo.co.uk

Received: October 25, 2009 **Accepted:** February 11, 2010

Abstract: Field, petrographic and geochemical data have been employed in appraising the compositional and the petrogenetic nature of the talc schist of Esie and environs, southwestern Nigeria. The rock unit occurs as low-lying lensoidal outcrops and in some places as massive or weakly foliated exposures. The main mineral assemblage of the rock is talc + anthophyllite and talc + chlorite + anthophyllite. Accessory minerals are ilmenite, hematite and spinel.

The variation plots of major oxides MgO, Al_2O_3, TiO_2 and SiO_2 on one hand and trace elements Ni, and Sc on the other, confirm komatiitic nature of the rock. Also, Petrogenetic inferences based on the rare earth elements (REE) and transition trace elements abundances, notably Ni and Cr, reveal almost flat heavy REE and enriched light REE (LREE) [$(La : Sm)_n$ = 1.53–5.06 and $(Ce : Yb)_n$ = 3.62–124.91] patterns. Ni (637–1870 μg/g) and Cr contents (1330–3440 μg/g) are consistent with the ultramafic parentage and komatiitic character of the rock.

A partial melting of upper mantle with variable post magmatic alteration/modification evolutionary model is proposed for the rock unit.

Original scientific paper

Povzetek: Za oceno sestave in petrogenetskih lastnosti lojevčevih skrilavcev širšega območja Esie v jugovzhodni Nigeriji smo uporabili podatke terenskih, petrografskih in geokemičnih raziskav. Litološka enota se pojavlja kot lečasti in ponekod masivni ali šibko foliirani izdanki. Glavna mineralna parageneza kamnine so lojevec + antofilit in lojevec + klorit + antofilit. Akcesorni minerali so ilmenit, hematit in spinel. Variacijski diagrami glavnih oksidov MgO, Al_2O_3, TiO_2 in SiO_2 na eni strani in slednih prvin Ni in Sc na drugi potrjujejo komatiitno naravo kamnine. Z geokemičnimi raziskavami elementov redkih zemelj (REE) smo dobili skoraj raven vzorec težkih REE in obogatene lahke REE (LREE) [$(La : Sm)_n$ = 1.53–5.06 in $(Ce : Yb)_n$ = 3.62–124.91]. Vsebnosti prehodnih slednih prvin, predvsem Ni in Cr [Ni (637–1870 µg/g) in Cr (1330–3440 µg/g)], se ujemajo z ultramafičnim poreklom in komatiitnim značajem kamnine.

Na tej osnovi je predlagan model nastanka litološke enote z delnim taljenjem zgornjega plašča, ki je bila postmagmatsko izpostavljena različni stopnji sprememb.

Key words: komatiite, petrogenesis, talcose rocks, trace elements, REE, Esie, Nigeria

Ključne besede: komatiit, petrogeneza, lojevčeve kamnine (skrilavci), sledne prvine, REE, Esie, Nigerija

Introduction

The Nigerian basement complex (Figure 1) consists of Precambrian gneisses and migmatitic rocks into which belts of N-S trending low to medium grade supracrustal rocks are infolded (Ajibade et al., 1987). This supracrustal rocks, otherwise called the schists, consist of low to medium-grade metasediments of pelitic to semi-pelitic compositions, belonging to carbonates, psammitic rocks as well as mafic and ultramafic (talcose) rocks.These occur as lenticular to ovoid shaped bodies intercalated within the metasediments. Both basement and supracrustal cover sequence have suffered polyphase deformation and metamorphism and are Intruded in some places by Pan-African granitoids.

The schist belts include those of Ilesha, Kusheriki, Maru, Wonaka and Anka. (Olade & Elueze, 1979; Ajayi,

1981; Kayode, 1981; Elueze, 1982; Klemm et al, 1984; Ige & Asubiojo, 1991;Truswell & Cope, 1963; Elueze, 1982; Ogezi, 1977) (Figure 1). Previous researchers attributed pre-metamorphic parent rocks to peridotite (Elueze, 1982), to magmatic origin (Ige & Asubiojo, 1991) or to tectonically emplaced slices of upper mantle material (Ogezi, 1977). The rocks in these areas are hardly preserved in their original state. Many bodies have suffered varying degrees of alteration and are extensively steatitized. Meta-utramafites are minor components of the Nigerian schist belts.

The Esie schistose rocks have been considered by some workers in the past to lie within the Egbe-Isanlu schist belt exposed in southwestern Nigeria (Annor, 1981, Ige & Onabajo, 2005). However, the Esie talcose rock actually is a northern extension of Ife-Ilesha schist belt. It lies within latitudes of $4^0$45'–$5^0$00' North and longitudes $8^0$00'–$8^0$15' East (Figure 1). The previous studies on the Ife Ilesha schistose rocks have generally focused on tectonic modeling (Rahaman, 1976; Olade & Elueze, 1979; Ajayi, 1981) and stratigraphic correlation (Klemm et al, 1983) with interpretations being based on major and trace element data. The Esie talcose rock have been studied mainly for their economic potential (Olorunfemi, 2007; Olorunfemi et al., 2009) and archaeological features (Olabanji et al., 1989; Ige & Onabajo, 2005).

The present study therefore, focuses on elucidating the origin and petrochemical characteristics of the talcose rock of Esie area in the northern part of Ife-Ilesha schist belt, and is expected to contribute to the knowledge of the geodynamic evolution of the schist belt in Nigeria.

Materials and Methods

For this purpose a systematic geological mapping was undertaken on a scale of 1 : 25,000. Optical (thin section) and X Ray Diffraction studies were carried out in order to understand the mineralogical composition. For the XRD determinations, powders of representative samples of six of the talc bodies were examined using a Philips–PW1011 model diffractometer. The diffractograms were recorded using a scanning rate 2^o $min^{-1}cm^{-1}$ with a Ni-filtered Fe K-alpha radiation.

Twelve pulverized samples of the rock unit were also chemically analyzed for major, trace and rare earth element composition by inductively coupled plasma–mass spectrometry (ICP-MS) instrumentation method at the Activation Laboratory Ontario, Canada. The detailed analytical procedure is described in Olorunfemi (2007).

Geological Setting and Petrography

The study area belongs to the Nigerian Basement Complex, which forms part of the mobile belt (Figure 1) that lies between the Archean to Early Proterozoic West African and Congo Cratons (KENNEDY, 1964). The dominant N-S trending structures and extensive areas of igneous rejuvenation of this basement are attributed to the Pan African Orogenic events (MCCURRY 1976, VAN BREEMAN et.al 1977).

In Esie, this unit occurs as low-lying boulders, massive or weakly foliated outcrops and also as lensoid bodies within country rocks (Figure 2). The low lying nature of the outcrops imposes a kind of flat to gently undulating terrain in some areas. Most outcrops of the talc deposits body are located around the southwestern end of the area. The boulder like and the massive varieties are whitish to grey in colour. However, some masses are brownish in colour probably due to iron

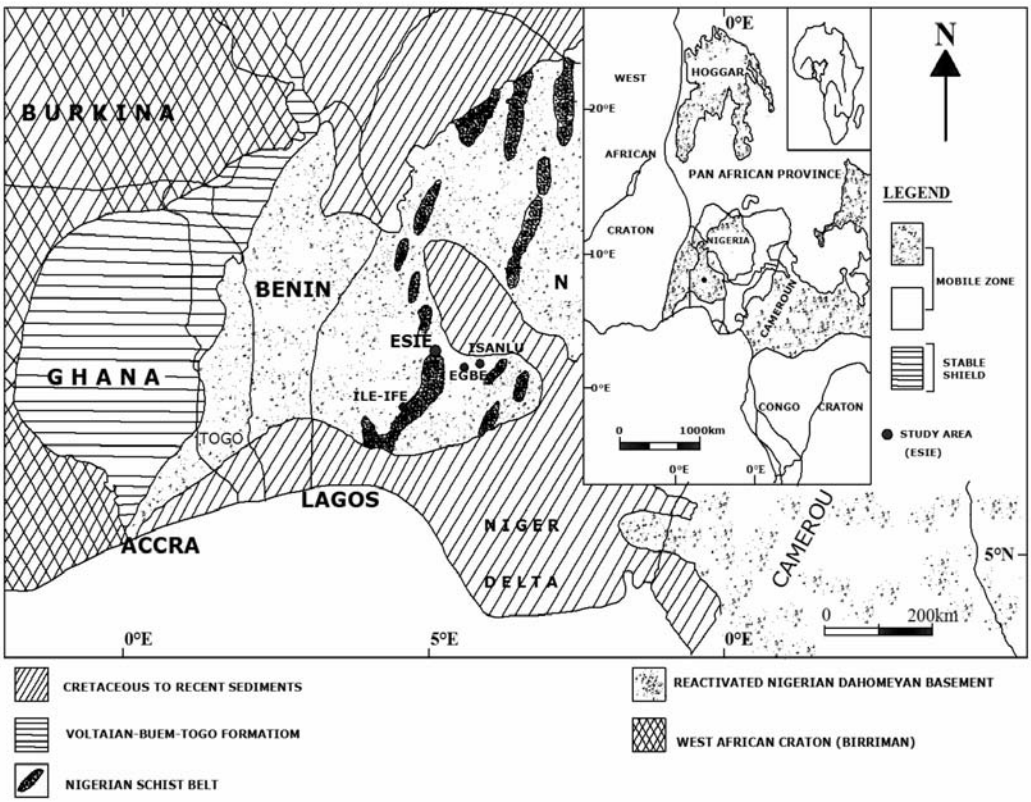

Figure 1. Map of Nigeria showing the location of Esie in the northern part of Ife-Ilesa schist belt. Inset: Map showing the location of the Nigerian basement within the Pan-African

percolation and pigmentation. Most of the samples are medium to fine-grained in texture with a characteristic soapy touch. The total extent along a NNE-SSW strike is about 10 km although the outcrops are not continuous.

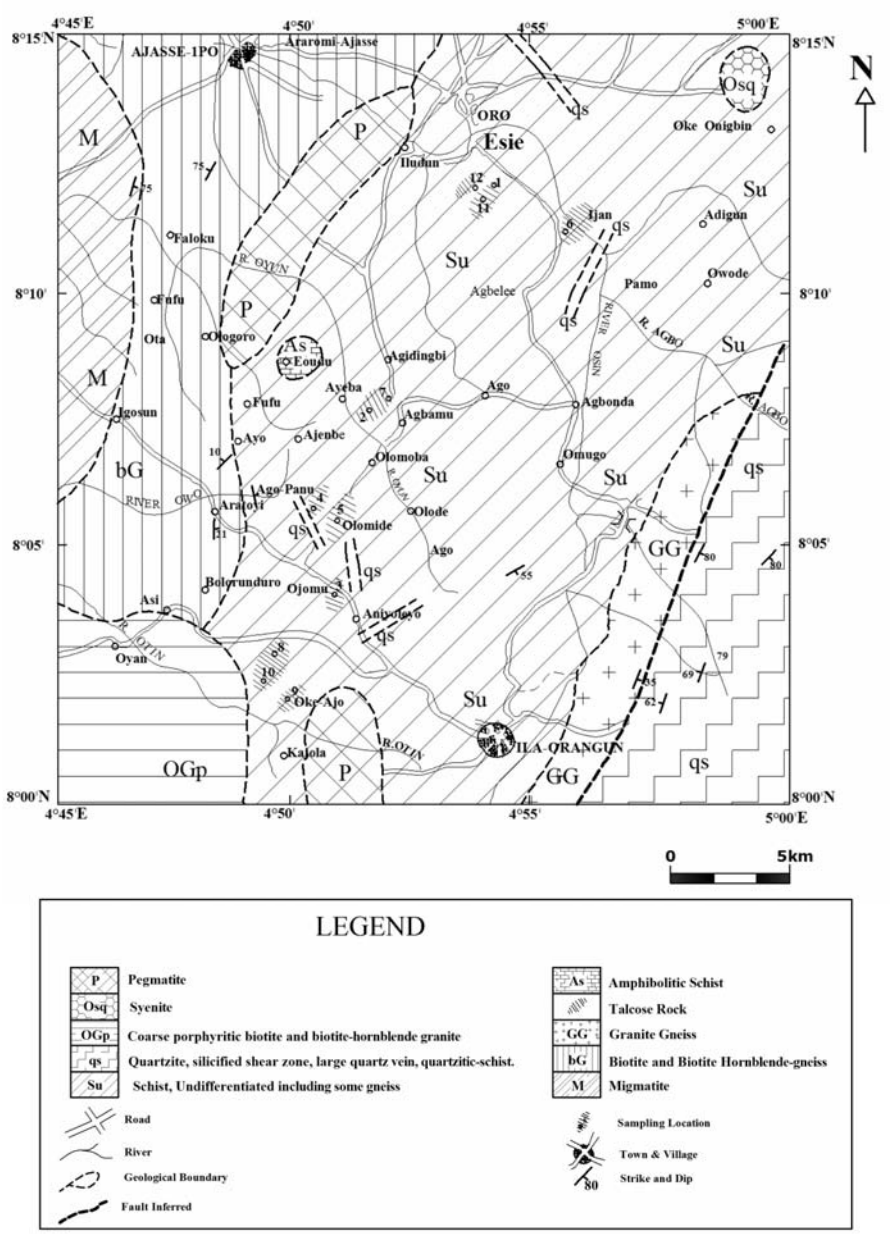

Figure 2. (Modified geological map from Geological Survey of Nigeria, 2004 and Olorunfemi, 2007)

The Esie talcose rock consists of talc as the most common mineral. This occurs together with varying amounts of chlorite, anthophyllite, and or tremolite. Primary silicate minerals are not preserved in this assemblage. The results of the X-ray diffraction analysis of powdered samples of the rock show conspicuous peaks of talc, anthophyllite and chlorite. Other minor peaks include mainly those of spinel, (Figures 3 and 4). Two petrographic varieties of this rock unit were distinguished being different in colour: talc-anthophyllite-schist and talc-chlorite-anthophyllite-schist.

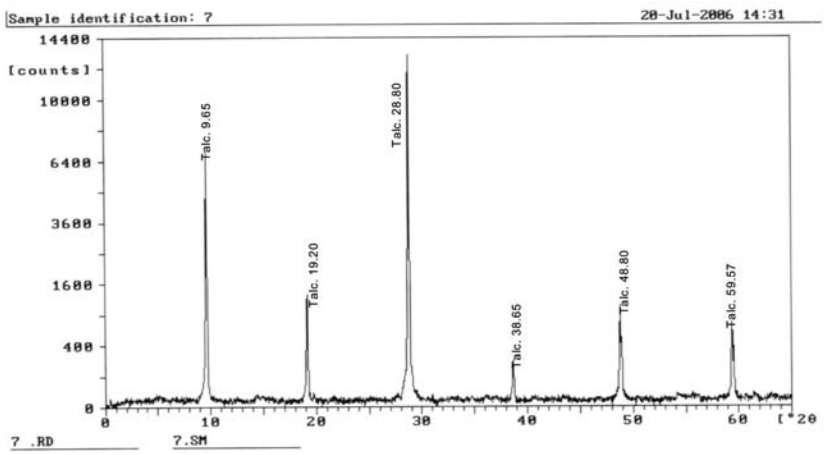

Figure 3. X-ray diffraction chart of talcose rock sample

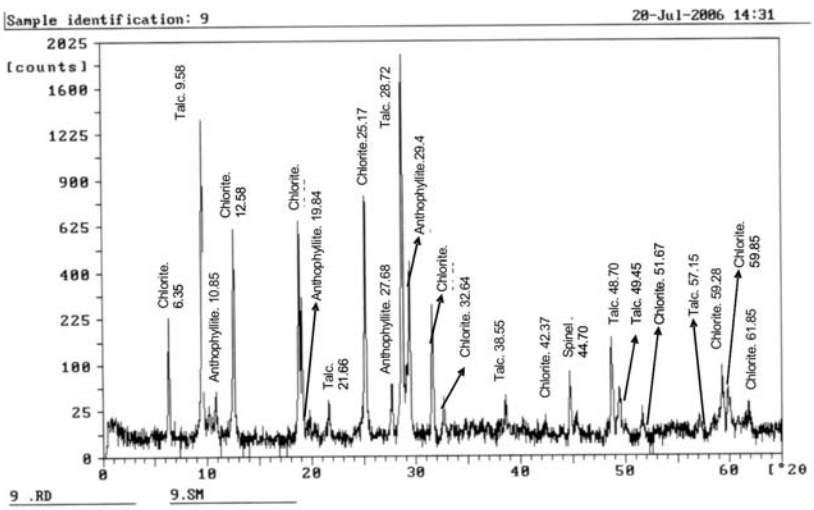

Figure 4. X-ray diffraction chart of the talcose rock sample with chlorite and anthophyllite

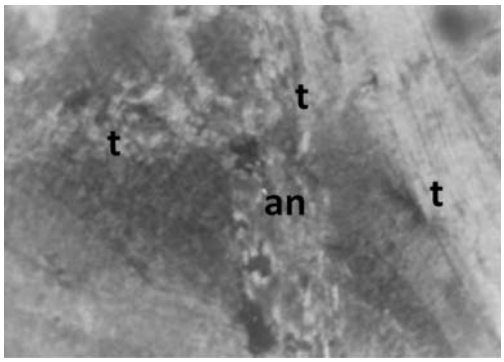

Figure 5a. Photomicrograph of Esie talcose rocks showing alteration of anthophyllite (an) within talc (t) matrix (x100). XPL= crossed polarized light

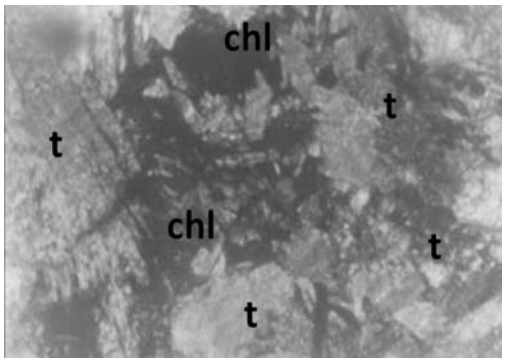

Figure 5b. Photomicrograph of Esie talcose rocks showing chlorite (chl) filling the interstices of the platy talc (t) (×100). XPL= crossed polarized light.

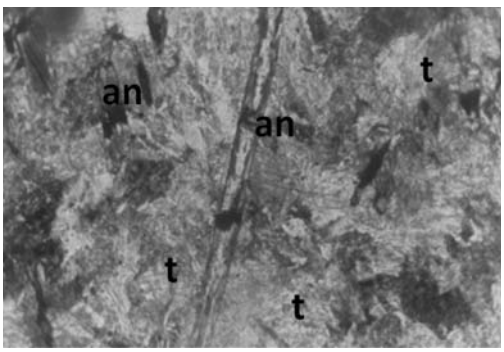

Figure 5c. Photomicrograph of Esie talcose rocks showing decussate arrangement of short and a long prismatic anthophyllite (an) within talc (t) matrix (×100). XPL= crossed polarized ligh

Talc-anthophyllite-schist consists of a large foliated mass of fine platy to fibrous aggregate of talc and traces of altered anthophyllite (Figure 5a). The rock varies in colour from buff white to light greyish green. Talc-chlorite-anthophyllite-schist consists of fine platy or fibrous aggregates of talc as well. Besides, radiating crystals of chlorites cluster in the talc matrix (Figure 5b), while anthophyllite forms long and short prismatic crystals. Some of them exhibit decussate arrangement and show spinifex texture (Figure 5c). The rock colour varies from buff-white to green depending on the relative proportion of the constituent minerals. When anthophyllite is dominant, the rock has a buff-white colour and a greenish one when chlorite prevails. Talc has been assessed to be between 70 % and 80 % (Figures, 3, 4, and 5). The proportion of anthophyllite and chlorite vary considerably while tremolite and opaque occurs in trace amounts.

For figs 5a-c, lower edge of the photo is 2mm

Talc in thin sections occurs as foliated mass, coarse to fine platy or fibrous

aggregates with parallel arrangement (Figure 5a). Anthophyllite is found as long or short prismatic crystals and exhibits a parallel extinction. It forms a radiating texture with decussate like arrangement radiating within the matrix of talc (Figure 5). Alteration of anthophyllite to talc is visible in some samples (Figure 5a). Chlorite is seen as net-like crystals within talc matrix (Figure 5b). It is greenish in colour and is strongly pleochroic in shades of green and brown.

Geochemical results and discussion

Tables 1a, 1b and 1c show the results of major, trace and rare earth element compositions of the Esie talcose rocks. All the samples from Esie show high MgO with mass fractions *w*/% (26.09–31.35 %) and low Al_2O_3 (0.50–5.54 %), K_2O (0.01–0.12 %), P_2O_5 (0.01–0.03 %), MnO (0.03–0.178 %) and TiO_2 (0.008–0.126 %) (Table 1a). The SiO_2 content of all the samples is generally in excess of 50 %. Values of SiO_2 greater than 45 % are generally regarded as upper limit for ultramafic igneous rocks. Considering the above, and in comparison with rocks of similar compositional characteristics, the overall major element chemical composition of the rocks is distinctly similar to rocks of komatiitic series and peridotitic affinity (Brooks & Hart, 1974; Arndt et al., 1977; Elueze, 1982). However, the seemingly high SiO_2 content may suggest possible syntectonic metamorphic silicification of the rock.

The concentrations of the transitional trace elements Ni (637–1870 μg/g) and Cr (1330–3440 μg/g) in the rock samples are also similar to those of peridotites (Divakara Rao et al., 1975). This feature indicates a parental magma derived from a mantle peridotite source (Rollinson, 1993). High Ni, Cr and MgO content in the samples coupled with a seemingly positive relationship (Table 1a, b). Suggests original magmatic partitioning and points to the existence of a high Ni-phase, presumably olivine in the parent rocks (Hawkesworth & O'nion 1977). Co and Ni are often thought to have similar geochemical behavior, although the distribution coefficient of Co in olivine/liquid is in general lower than of Ni (Duke, 1976; Leeman, 1974). By the same argument, the high Cr-phase may be spinel or Cr-rich orthopyroxene. Arndt (1976) has shown that the liquidus phases in a melt with MgO > 20 % are olivine and chromite; if MgO is between 2.0 % to 12 %, olivine + pyroxene; and with MgO < 12 %, pyroxene + plagioclase.

The talcose rock samples have variable contents of V, Cu and Zn. The low V and Cu contents compared to all other elements possibly reflects the primitive nature of these rocks. The Cu and Zn contents are highly variable in the samples with the sample being generally poorer in Cu but elevated values of Zn (Table 1b). This behavior may be as a result of the high mobility of Zn during weathering processes. The Rb and Hf contents of

Table 1a. Major elements data (*w*/%) of Esie talcose rocks and data from typical examples of ultramafic rocks of komatiitic affinity (*w*/%)

Oxides	1	2	3	4	5	6	7	8	9	10	11	12	Mean 13	S834	Gt
SiO_2	55.41	58.18	57.99	52.87	58.30	57.97	58.19	57.10	50.48	55.32	55.38	57.38	56.21	43.61	50.16
Al_2O_3	2.45	0.64	0.55	2.76	0.95	0.85	0.53	1.12	5.54	1.77	2.11	0.5	1.66	7.71	4.46
Fe_2O_3T	6.93	5.74	6.73	7.51	5.23	6.49	5.61	7.6	7.09	7.31	10.63	6.03	6.90	10.45	2.54
MnO	0.072	0.069	0.121	0.178	0.088	0.106	0.072	0.139	0.096	0.134	0.206	0.03	0.10	0.16	0.22
MgO	28.68	30.56	29.81	31.35	30.44	29.76	30.08	29.18	29.91	30.26	26.09	30.47	29.71	25.32	23.86
CaO	0.04	0.01	0.12	0.31	0.04	0.01	0.01	0.03	0.17	0.21	0.37	0.01	0.16	6.86	4.79
Na_2O	0.17	0.16	0.16	0.16	0.25	0.18	0.15	0.15	0.12	0.18	0.20	0.09	0.16	0.20	0.3
K_2O	0.03	0.01	0.01	0.04	0.01	0.01	0.01	0.01	0.05	0.07	0.12	0.01	0.03	0.10	0.01
TiO_2	0.053	0.017	0.008	0.073	0.034	0.028	0.008	0.038	0.126	0.044	0.061	0.056	0.05	0.33	0.45
P_2O_5	0.02	0.01	0.03	0.03	0.01	0.03	0.01	0.02	0.01	0.01	0.01	0.01	0.02	0.06	0.1
LOI	5.16	4.6	3.9	4.23	4.49	4.24	4.68	4.67	6.07	4.22	4.57	4.76	4.63	6.15	2.03
Total	99.01	99.96	99.59	99.73	99.79	99.75	99.36	99.78	99.65	99.53	99.75	99.91	99.65	100.41	99.97
CaO/Al_2O_3	0.02	0.02	0.21	0.11	0.04	0.01	0.01	0.03	0.03	0.19	0.18	0.02	0.10		
**FeO	6.23	5.16	6.05	6.75	4.70	5.84	5.04	6.83	6.38	6.57	9.56	5.42			

- = not detected

1–12 = Samples from Esie (talc-anthophyllite-chlorite) (This Study)

13 = Mean values of samples 1–12

S834 = Komatiite from Suomussalmi, Finland (Jahn et.al., 1980)

Gt = Ife meta-ultramafite: anthophyllite- talc/tremolite-chlorite (trace) - magnetite-(trace). Ige & Asubiojo, 1991.

** FeO = Fe_2O_3/1.112

Table 1b. Trace elements data (µg/g) of Esie talcose rock and data from typical examples of ultramafic rocks of komatiitic affinity (µg/g)

Elements	1	2	3	4	5	6	7	8	9	10	11	12	Mean	S834	Gt
Sc	6	4	3	7	3	2	3	2	4	4	26	2	5.5	-	10
V	5	9	<5	16	<5	<5	<5	<5	18	16	32	27	10.7	150	-
Cr	2690	1450	3440	1520	1330	1880	1520	2130	1780	1490	2760	1640	1969	3004	1978
Co	67	57	70	70	76	79	75	78	81	72	76	42	70.25	100	57
Ni	1100	1380	1290	1460	1590	1870	1620	1620	1480	1510	637	888	1370.4	1171	4465
Zn	161	123	182	95	125	140	11	140	71	86	145	66	120.4	-	159
Cu	14	29	3	3	5	6	8	3	4	4	4	4.2	10.4	-	-
As	<5	<5	<5	<5	<5	<5	<5	<5	<5	<5	<5	<5	<5	-	-
Rb	6	<2	2	2	<2	<2	<2	<2	<2	<2	<3	<2	<2	1	1.4
Sr	2	<2	5	2	2	<2	<2	<2	2	,2	.3	<2	<2	29	-
Zr	<4	<4	<4	7	<4	<4	<4	<4	4	<4	8	<4	<4	7	-
Ba	14	<3	170	49	42	17	63	110	10	50	32	3	46.7	-	92

- = not detected

1–12 = Samples from Esie (talc-anthophyllite-chlorite) (This Study)

13 = Mean values of samples 1–12

S834 = Komatiite from Suomussalmi, Finland (Jahn et.al., 1980)

Gt = Ife meta-ultramafite: anthophyllite- talc/tremolite-chlorite (trace)-magnetite-(trace). Ige & Asubiojo, 1991.

Table 1c. Rare earth elements data (μg/g) of Esie talcose rocks and data from typical examples of ultramafic rocks of komatiitic affinity (μg/g)

Elements	1	2	3	4	5	6	7	8	9	10	11	12	Mean	S834	Gt
La	1.4	0.5	6.5	3.6	1.7	1.6	1.6	1.8	1.4	1.0	2.0	2.5	2.13	0.634	3.0
Ce	4.7	0.7	9.4	17	39.8	48.6	70.3	46.9	30.3	2.8	17.7	3.6	24.31	2.292	7.9
Pr	0.37	0.16	1.48	1.04	0.66	0.48	0.6	0.53	0.34	0.26	0.69	0.86	0.62		
Nd	1.4	0.6	5.2	3.6	2.7	1.7	2.2	1.8	1.1	1.0	2.6	3.1	2.25	2.11	1.8
Sm	0.3	0.2	0.8	0.7	0.7	0.3	0.5	0.5	0.2	0.2	0.7	0.6	0.48	0.742	0.7
Eu	0.06	<0.05	0.17	0.14	0.18	0.08	0.12	0.07	0.05	0.06	0.15	0.13	0.10	0.266	0.5
Gd	0.2	0.1	0.6	0.7	<0.7	<0.1	<0.1	<0.1	<0.1	0.3	0.5	0.7	0.32	1.026	
Tb	<0.1	<0.1	<0.1	<0.1	<0.1	<0.1	<0.1	<0.1	<0.1	<0.1	<0.1	<0.1	<0.1		0.3
Dy	0.2	0.2	0.4	0.9	0.6	0.2	0.3	0.3	0.2	0.2	0.5	0.3	0.36	1.271	
Ho	<0.1	<0.1	<0.1	0.2	<0.1	<0.1	<0.1	<0.1	<0.1	<0.1	<0.1	<0.1	<0.1		0.2
Er	0.1	<0.1	0.2	0.7	0.3	0.1	0.2	0.2	0.1	0.2	0.3	0.2	0.23	0.823	
Tm	<0.05	<0.05	<0.05	0.11	<0.05	<0.05	<0.05	<0.05	<0.05	<0.05	<0.05	<0.05	<0.05		
Yb	0.01	<0.1	0.2	0.7	0.3	0.1	0.2	0.2	0.2	0.2	0.3	0.2	0.23	0.862	0.7
Lu	<0.04	<0.04	<0.04	0.12	0.05	<0.04	<0.04	<0.04	<0.04	<0.04	<0.04	<0.04	<0.04	0.135	0.3
Total	9.03	3.00	25.25	29.51	47.94	53.25	76.41	52.69	34.28	6.51	25.73	12.48	31.23		

1–12 = Samples from Esie (talc-anthophyllite-chlorite) (This Study)
13 = Mean values of samples 1–12
S834 = Komatiite from Suomussalmi, Finland (Jahn et.al., 1980)
Gt = Ife- meta-ultramafite: anthophyllite-talc/tremolite-chlorite (trace)-magnetite-(trace). IGE & ASUBIOJO, 1991.

the talcose rocks are generally within the range of values for the ultramafic rocks of komatiitic affinity. The large ionic radii of these elements results in their exclusion from almost all mineral phases crystallizing during metamorphism. The Esie rocks are however depleted in Zr and Sr content relative to the ultramafic rock of komatiitic affinity.This may be due to the absence of a mineralogical phase to carry this element in the rock as a result of polymetamorphic reconstitution and alteration.

This petrogenetic affinity is also demonstrated in the plots of TiO_2 against Al_2O_3 and TiO_2 versus SiO_2. The talcose rock samples plot below 1.0 % TiO_2 value in both cases (Figure 6a & 6b), which is similar to the samples of Munro Township, Canada (ARNDT et.al, 1977). The plots of Al_2O_3 vs. FeO/(FeO + MgO) and Al_2O_3, MgO and FeO+TiO_2 further confirms the komatiitic petrogenetic affinity of this rock unit (Figure 7a & 7b). On the tholeiitic-komatiite classification scheme of NALDRETT & CABRI (1976) and the classification of volcanic rocks after JENSON (1976), the Esie rock samples plot predominantly in the fields of komatiite and peridotitic komatiite respectively.

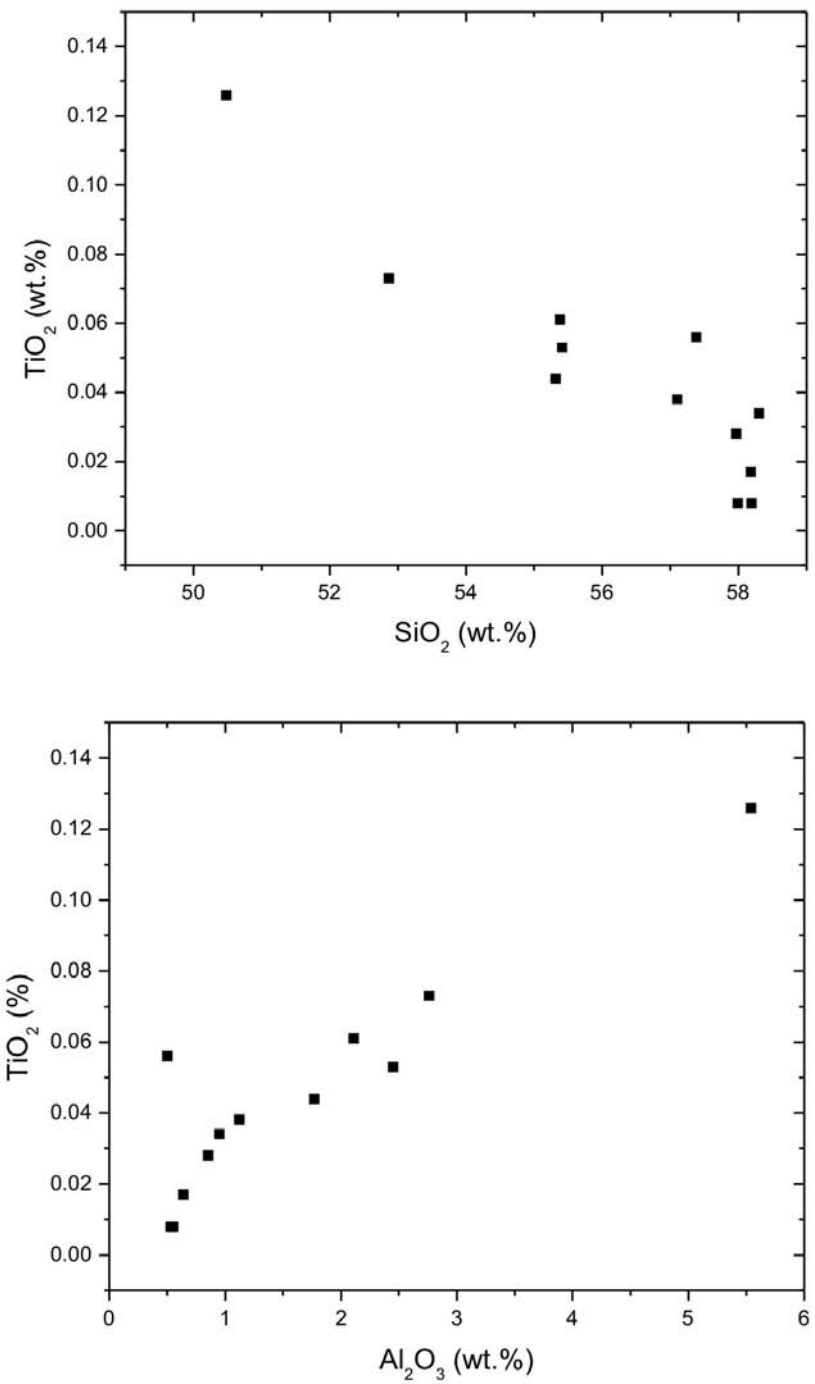

Figures 6a, b. Variation of TiO_2 with SiO_2 and Al_2O_3 (*w*/%)

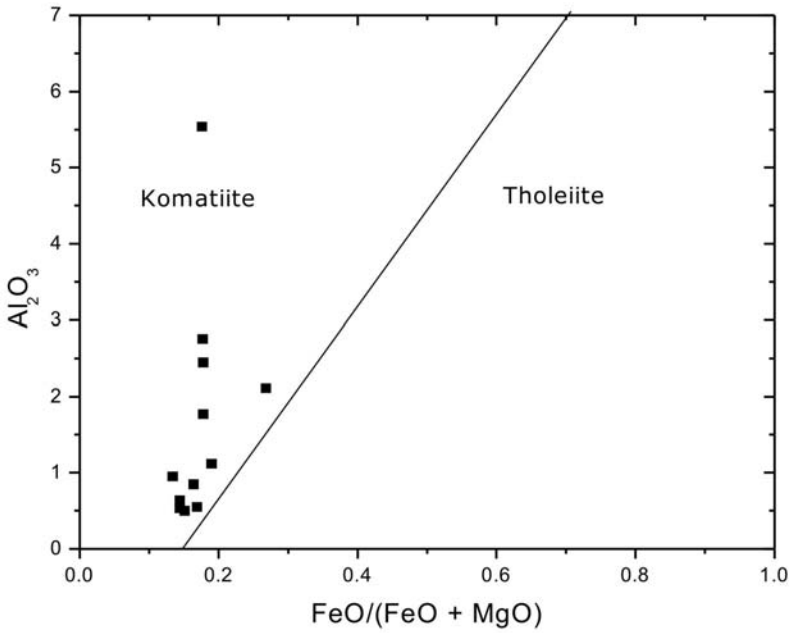

Figure 7a. Variation of Al_2O_3 with *w*(FeO/(FeO + MgO))/% ratio in Esie talcose rocks (NALDRETT & CABRI, 1976). Samples plot in the komatiite field.

PK: Peridotitic komatiite,
BK: Basaltic komatiite,
HFT: High-Fe tholeiite basalt
HMT: High-Mg tholeiite basalt,
HMT: High-Mg tholeiite basalt,
TA: Tholeiitic andesite
TD: Tholeiitic dacite,
TR: Tholeiitic rhyolite,
CB: Calc – alkali basalt,
CA: Calc-alkali andesite,
CD: Calc-alkali dacite,
CR: Calc-alkali rhyolite

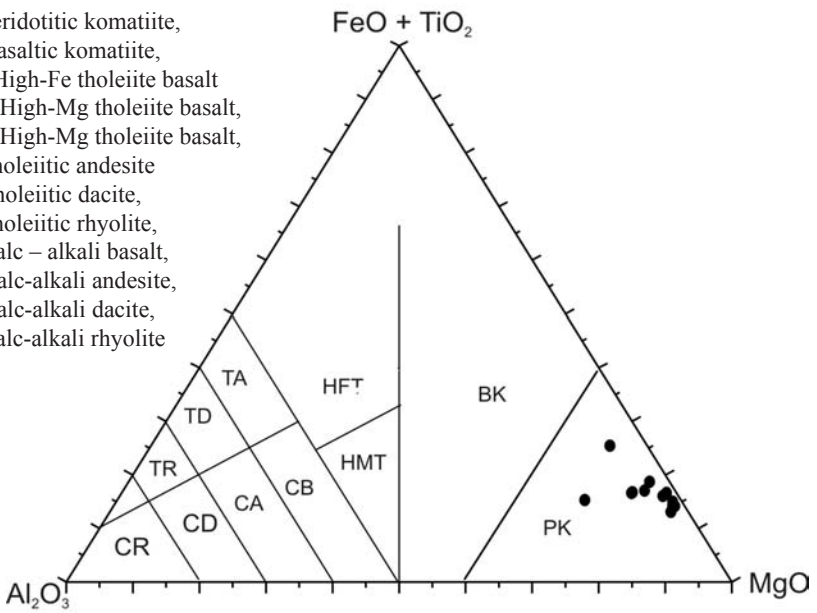

Figure 7b. Classification of volcanic rocks after JENSON (1976). On the diagram, Esie talcose rocks plot in the field of peridotitic komatiite.

Due to their coherent geochemical behaviour, REE are considered as resistant to post magmatic alterations and metamorphism. Therefore, they have been used in this study to present petrogenetic and petrotectonic interpretations. Although, ambiguity may sometimes emerge when a detailed comparison is made between different rock units, yet, they are still fairly good indicators (Jahn & Sun, 1979). Rare earth elements features as shown in the chondrite-normalized REE patterns for these rocks (Figure 8a and 8b) reveal that almost all the samples are high in total REE abundance. The values range from about 3.00 to 76.41 µg/g with an average value of 31.23 µg/g (Tables 1c, and 2).This indicates that this rock unit is distinctly different from those of ophhiolite from an orogen, but rather close to those of the ultramafic melanocratic rock series.(Wang Yuwang et. al., 2004) The talcose rock is enriched in LREE with $(Ce/Sm)_n$ ranging from 0.83 to 39.07 and moderate fractionation of source magma as shown by $(La/Yb)_n$ ratios (3.37–21.96).

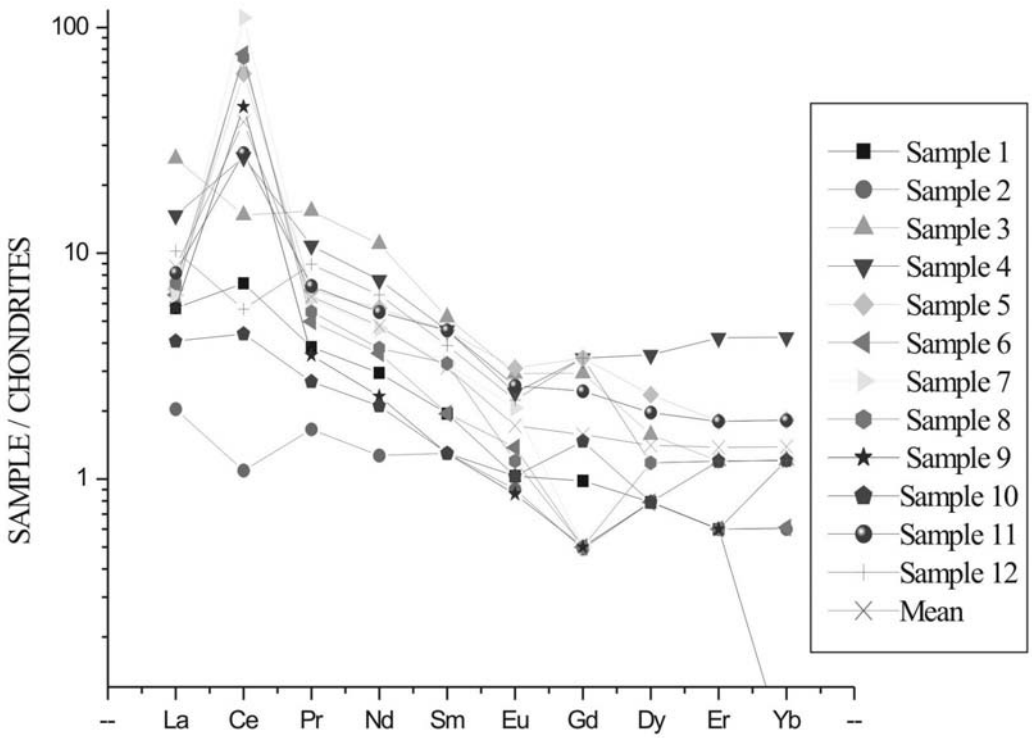

Figure 8a. Chondrite-normalised REE patterns for Esie talcose rocks

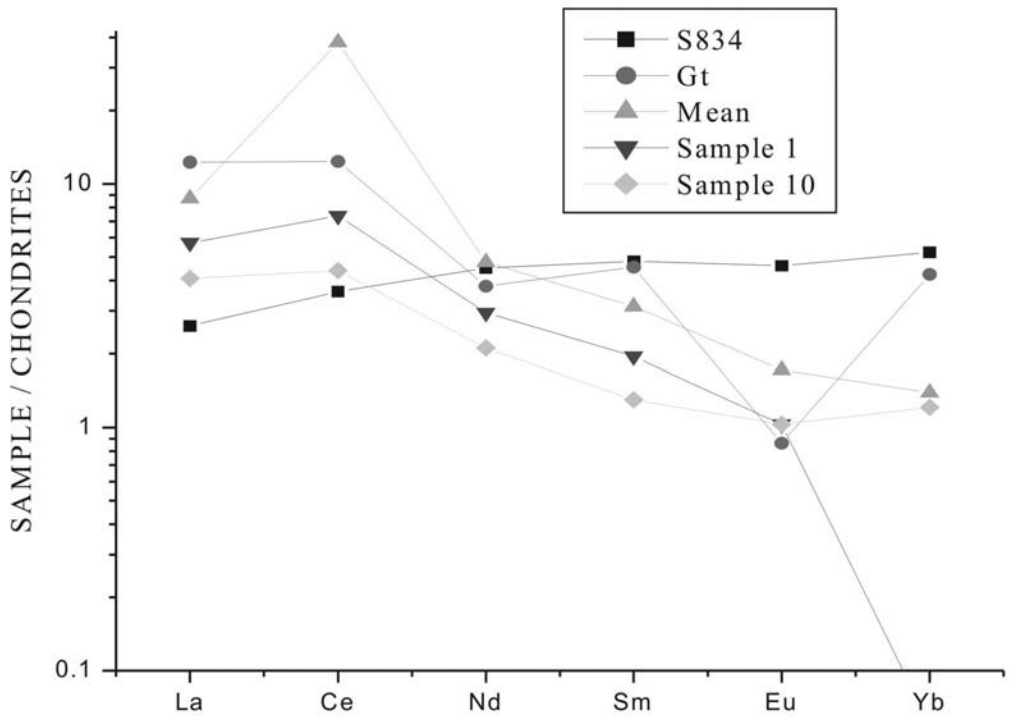

S834= Komatiite from Suomussalmi, Finland (Jahn et.al., 1980).
Gt = Ife meta-ultramafite: anthophyllite- talc/tremolite-chlorite (trace) - magnetite-(trace) (IGE & ASUBIOJO, 1991).

Figure 8b. Chondrite-normalised REE patterns of the Esie talcose rocks in comparison with data from typical ultramafic rocks of komatiitic affinity.

Most of the REE patterns have no significant detectable Eu anomalies but show significantly positive Ce anomalies. In contrast, a few samples show detectable Ce depletion. This may be due to the change in oxidation state of the Ce ion from trivalent to tetravalent as a consequence of metamorphic redistribution. (IGE & ASUBIOJO 1991) Positive anomalous Ce abundances have been known to occur in komatiitic rocks that have undergone weathering and burial metamorphism (FRYER, 1977).

Samples of the talcose rock with significant quantity of anthophyllite blasts/ grains show least modification, while the most evolved samples are enriched in talc (OLORUNFEMI, 2007). Their patterns show enriched LREE and almost flat HREE (Figure 8a & 8b). Judging from the complex REE patterns in Ar-

Table 2. The REE chondrite-normalised value of the Esie talcose rocks
** Chondrite values obtained from Evensen et. al (1978)

	1	2	3	4	5	6	7	8	9	10	11	12	Mean	S834	Gt	**
La	5.72	2.04	26.27	14.71	6.95	6.54	6.54	7.36	5.72	4.08	8.18	10.22	8.7	2.5919	12.26	0.2446
Ce	7.37	1.09	14.74	26.64	62.39	76.19	110.2	73.52	44.5	4.39	27.75	5.64	38.11	3.593	12.36	0.6379
Pr	3.84	1.66	15.36	10.79	6.85	4.98	6.23	5.5	3.53	2.7	7.16	8.92	6.43	--	--	0.09637
Nd	2.95	1.27	10.98	7.6	5.7	3.6	4.64	3.8	2.32	2.11	5.49	6.54	4.75	4.453	3.79	0.4738
Sm	1.95	1.3	5.19	4.55	4.55	1.95	3.25	3.25	1.3	1.3	4.55	3.9	3.12	4.818	4.54	0.154
Eu	1.03	0.9	2.93	2.41	3.1	1.38	2.06	1.2	0.86	1.03	2.59	2.24	1.72	4.584	0.8617	0.05802
Gd	0.98	0.49	2.94	3.43	3.43	0.5	0.5	0.5	0.5	1.47	2.45	3.43	1.57	--	--	0.2043
Dy	0.79	0.79	1.57	3.54	2.36	0.79	1.18	1.18	0.79	0.79	1.97	1.18	1.41	--	--	0.2541
Er	0.6	0.6	1.2	4.22	1.8	0.6	1.2	1.2	0.6	1.2	1.8	1.2	1.38	--	--	0.166
Yb	0.06	0.6	1.21	4.24	1.82	0.61	1.21	1.21	1.21	1.21	1.82	1.21	1.39	5.221	4.239	0.1651
Total	**25.29**	**10.74**	**82.39**	**82.13**	**98.95**	**97.14**	**137.01**	**98.72**	**61.33**	**20.28**	**63.76**	**44.48**				
La/Yb_n	95.3	3.4	21.96	3.46	3.82	10.72	5.4	6.08	4.72	3.37	4.49	8.45	6.26			
Ce/Sm_n	3.78	0.83	2.84	5.85	13.71	39.07	33.9	22.62	34.23	3.38	6.09	1.45	12.21			
Ce/Yb_n	122.83	1.817	12.18	6.28	34.28	124.91	91.07	6.56	36.78	3.62	8.38	4.66	27.42			
La/Sm_n	2.93	1.57	5.06	3.23	1.53	3.35	2.01	2.26	4.4	3.1	1.8	2.62	2.79			

chean komatiitic rocks, Sun & Nesbitt (1978) proposed that the sources of spinifex textured komatiite must have originated from a depth greater than 400 km in the mantle. Early melts of low degree of partial melting may have concentrated more LREE and LIL. When these melts are separated, the residual mantle source would probably be depleted in LREE. There is no discernible trend in the variation of LREE and HFSE elements such as Ti and Sc, in the Esie talcose rocks. For example, when Ti is plotted against La, Sc and Yb (Figure 9a, 9b & 9c) there is no consistency in all the variations. Thus, if La, Ti, Yb, and Sc abundances are controlled by partial melting or simple fractional crystallization process, a consistent co-variation or conformity should be observed in the three elements. However, if the LREE results from a complex melting process no consistent variation would be observed. The REE have been known to be immobile elements and are expected to reflect the primary petrogenetic characteristics of fresh and unaltered igneous rocks. Some certain trace elements like Ti, Y, Nb, Zr (Menzies, 1976) are in general considered to be immobile during rock alteration. However, the investigations of basaltic rock samples by some workers (Wood et al., 1976, Ludden & Humphris, 1978; Ludden & Thompson, 1978, 1979) have shown that in certain situations, especially during rock alterations, the REE are mobile. Hellman & Henderson (1977) have also suggested that the LREE may be mobile also during rock alteration. Hellman et al., (1979) identified the principal types of REE enrichment and discovered that to an extent, the most important problem is LREE or HREE group mobility or selective mobility, mainly of La, Ce and most likely Eu especially during rock alteration or fractionation. The Esie talcose rocks in almost all cases show extensive enrichment $(La : Sm)_n = 1.53–5.06$, $(La : Yb)_n = 3.37–21.96$ relative to chondrite. Arth et. al. (1977) formulated a unified petrogenetic model where the tholeiitic and the komatiitic series were thought to be genetically related simply because of their intimate spatial relationship. They believe that the tholeiitic melts, having $(La/Sm)_n$ and $(Gd/Yb)_n$ ratios >1.0, might be the early melts extracted from a mantle source, characterized by a flat chondritic REE pattern. The extraction leads to LREE-depleted nature in the residue which in turn serves as the source for some LREE-depleted komatiites. This could be a plausible mechanism for LREE depletion, at least in some of the Esie rock samples.

The extent of LREE mobility can also be shown by the ratios of $(La : Sm)_n$, $(Ce : Sm)_n$, $(Ce : Yb)_n$ and $(La : Yb)_n$. The ratios are given in Table 4. The $(Ce : Sm)_n$ ratios vary widely, indicating the Ce mobility. The $(La : Sm)_n$ ratios are fairly constant, regardless of the differ-

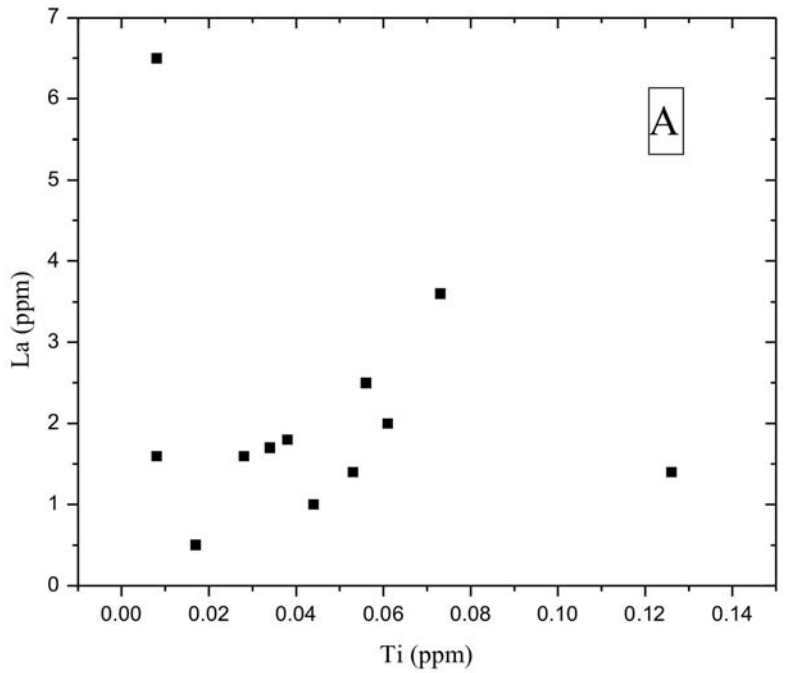
A
La (ppm)
Ti (ppm)
0
1
2
3
4
5
6
7
0.00
0.02
0.04
0.06
0.08
0.10
0.12
0.14

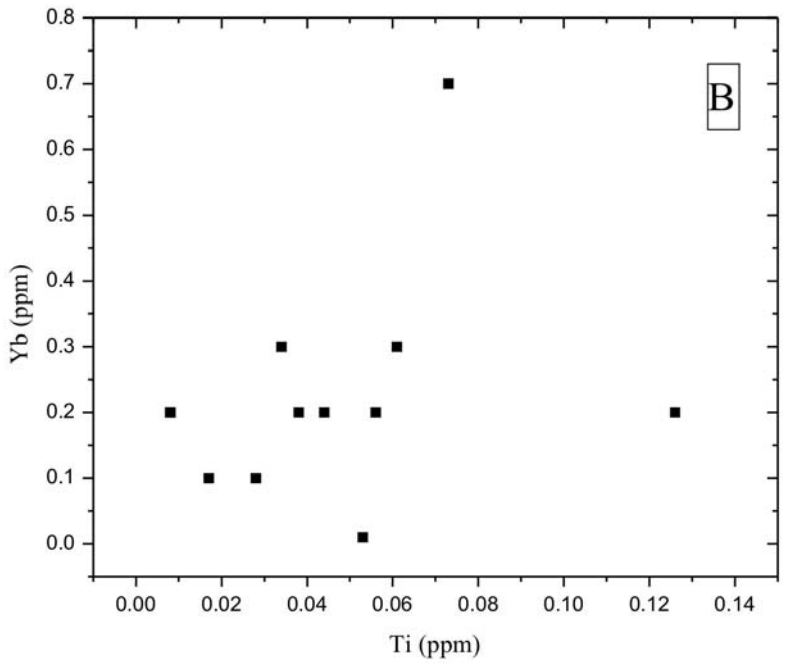
B
Yb (ppm)
Ti (ppm)
0.0
0.1
0.2
0.3
0.4
0.5
0.6
0.7
0.8
0.00
0.02
0.04
0.06
0.08
0.10
0.12
0.14

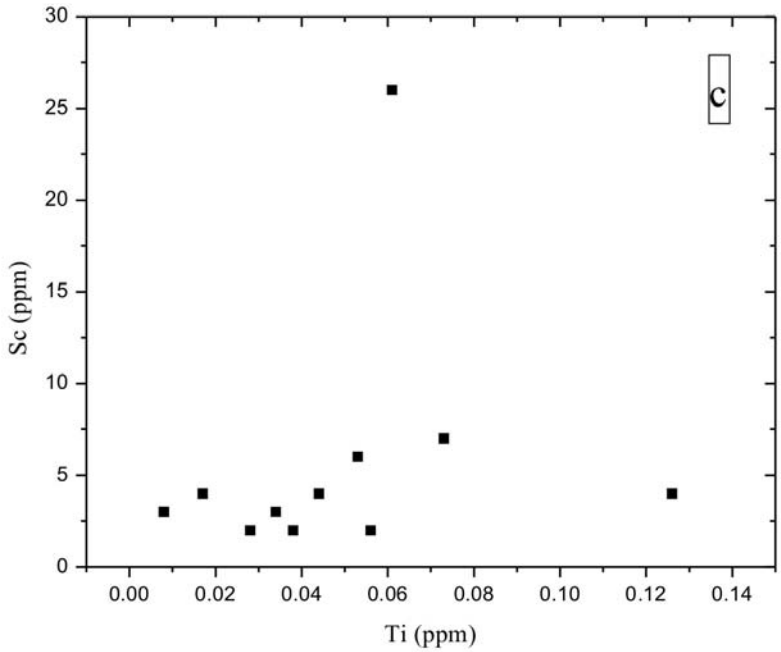

Figures 9a, b&c. Ti, La, Yb and Sc variation for the Esie talcose rocks

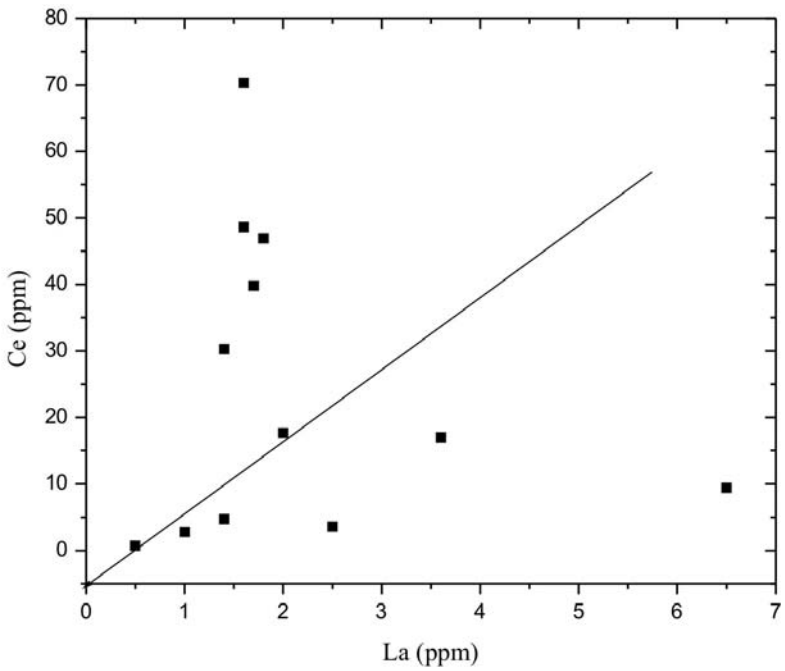

Figure 10. Ce-La variation in Esie talcose rocks

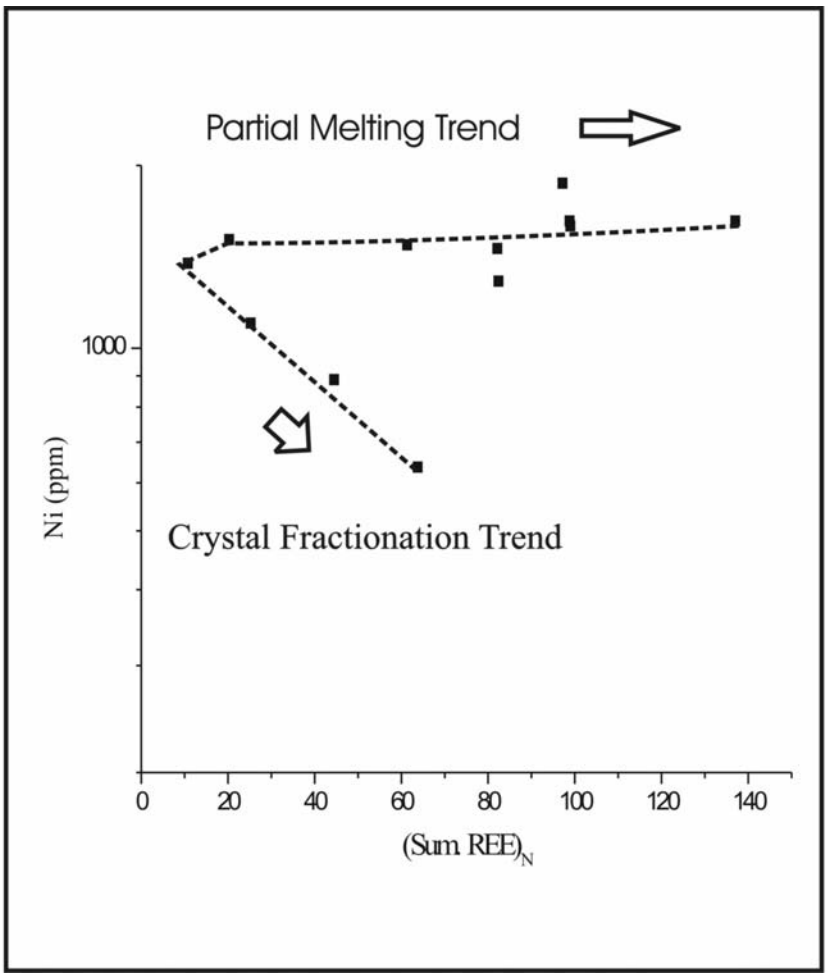

Figure 11. Experiment by Ringwood (1975) on the evolutionary trends of Ni against REE abundances. On the diagram, Esie talcose rocks plot in both trends

ent states of the talcose rock, whether altered or not. From a closer look, the data may imply that, apart from Ce, metamorphism itself has not thoroughly altered the REE patterns of the rocks. Similarities in $(La : Sm)_n$ ratios and the fact that the bodies are within the same area, could suggest that various talcose bodies originate from the same magmatic chamber and that possibly the LREE character is inherited from the parent rocks.

Although there is evidence of extensive modification, still some samples that are enriched in talc have suffered the least

alteration effect and their patterns move closer to those recorded for well known ultramafic komatiites (Figure 8b).

Apart from the weathering processes, the Esie talcose rocks must have undergone polymetamorphic reconstitution. This can be shown by the plot of La against Ce (Figure 10). If the La enrichment is a primary petrogenetic effect, La and Ce should show a consistent variation. (since La is known to be slightly more compatible than Ce in the mafic system) As shown in Figure 10, there is no real consistent relationship between the two elements. This inconsistency may suggest the komatiitic nature of the source of the parent magma and also some Ce mobility.

Conclusions

Mineralogical and geochemical evidence show the Esie talcose rock is ultramafic and have undergone series of alteration in which the original mineralogy has not been preserved. Intensive weathering and poly metamorphic reconstitution are evident.

Chemical data of the rock indicate peridotitic komatiitic composition of its parental melt. The MgO content of the rock is in conformity with similar greenstone rock units from Isanlu-Egbe and parts of the ife Ilesha schist belt, central Nigeria. The high MgO content of the Esie rocks is attributed to both olivine and orthopyroxene. The highly enriched REE could pertain to the same minerals.

Most probably, the rock evolved from a complex and partial melting of upper mantle. Evidence of minor crustal contamination and fractional crystallization are evidently noticeable.

Acknowledgements

Thanks are due to Dr. A. F. Abimbola of the University of Ibadan, Nigeria for facilitating the geochemical analyses at the Activation Laboratories Canada. Mr. T. A. Adesiyan, of Obafemi Awolowo University, Ile Ife, Nigeria is acknowledged for assisting in the XRD determinations of the talcose rock.

References

Ajayi, T. R. (1981): On the geochemistry and origin of the amphibolites in Ife-Ilesa area, S.W. Nigeria. J. Min. Geol., 17: 179–195.

Ajibade, A. C., Rahaman, M. A. & Woakes, M. (1987): Proterozoic crustal Development in the Pan-African regime of Nigeria. In: Proterozoic Lithospheric Evolution (Kroner, A., Ed.), Amer. Geophy. Union, 17, 259–271.

Annor, A. E. (1981): The geology of the area around Okene, South West-

ern Nigeria. Unpubl. Ph. D Thesis, University of Wales.

Arndt, N. T. (1976): Melting relations of ultramafic lavas (komatiite) at 1 atm and high pressure. Yb. Carnegie Instn. Wash. 75, 555–62.

Arndt, N. T., Naldrett, A. J. & Pyke, D. R. (1977): Komatiitic and iron rich theoliitic lavas of Munro Township, Northeast Ontario. J.of Petrol, 18, 319–369.

Arth, J. G., Arndt, N. T. & Naldrett, A. J. (1977): Genesis of Archean komatiites from Munro Township, Ontario: trace-element evidence. Geology, 5, 590–4.

Brooks, S. C. & Hart, S. R. (1974): On the significance of Komatiite. Geology, 5, 107–110.

Divakara Rao. V., Satyanarayana, K., Navovi, S. M. & Haussain, S. M. (1975): Geochemistry of Dharwar ultramafics and the Archean mantle. Lithos, 8, 77–91.

Duke, J. M. (1976): Distribution of the period four transition elements among olivine Calcic clinopyroxene and mafic silicate liquid: experimental results. J. Petrology, 17,499–521.

Elueze, A. A. (1981): Geochemistry and petrotectonic setting of metasedimetary rocksofthe schist belts of Ilesa area south western Nigeria. Nigerian Journal of Mining and Geol 18, 198–202.

Elueze, A. A. (1982): Mineralogy and chemical nature of metaultramafites in Nigerian schist belts. J. Min. Geol., 19 (2), 21–29.

Evensen, N. M., Hamilton, P. J. & O'Nions, R. K. (1978): "Rare-earth abundances. In chondritic meteorites" Geochim. Cosmochim. Acta 42, 1199–1212.

Fryer, B. J. (1977): Rare evidence in iron formations for changing Precambrian Oxidation states. Geochim. Cosmochim. Acta, 41: 361–367.

Green, D. H. (1975): Genesis of Archean peridotite magmas and constrains on Archean geothermal gradients and tectonics. Geology, 3, 15–18.

Hawkesworth, C. J. & R O'Nious, K. (1977): The petrogenesis of Archean Volcanic rocks from South Africa. J. Petrol., 18, 487–520.

Hellman, P. L. & Henderson, P. (1977): Are rare earth elements mobile during spilitisation? Nature vol. 267, 38–40.

Hellman, P. L., SMITH, R. E. & Henderson, P. (1979): The mobility of the rare earth elements: evidence and implications from selected terrains affected by burial metamorphism. Contrib. Mineral. Petrol., 71: 22–44.

Ige, O. A. & Asubiojo, O. I. (1991): Trace element geochemistry and petrogenesis of some metaultramafites in Apomu and Ife-Ilesha area of southwestern Nigeria.Chemical Geology 91, 19–32.

Ige, O. A. & Onabajo, O. (2005): Mineralogy and raw material characterization of Esie stone sculpture. Ife Journal of Science vol 7, no. 1, 113–118.

Jahn, B. M. & Sun, S. S. (1979): Trace element distribution and isotopic composition of Archaean Green-

stones. In: AHRENS, L. H. (ed.), Origin and Distribution of Elements, Second Symposium, Paris. Phys. Chem. Earth, 11, 597–618.

Jahn, B. M., Uuray, B., blais, S., Capdevilla, R., Cornichet, J., Vidal, P. & Hameurt, J (1980): Trace element geochemistry and petrogenesis of Finnish greenstone belts. J. Petrol., 21: 201–244.

Kayode, A. A. (1981): Komatiitic components in Ife-Ilesha amphibolite complex. 17th Ann. Con. Nig. Min. Geosci. Society, Calarbar Abstract, 37–38

Kennedy, W. O. (1964): The structural differentiation of Africa in the Pan African (500m.y) tectonic episode: 8th Ann. Resp. Inst. Afr.Geol. Univer. Leeds, 48–49.

Klemm, D. D., Scheider, W. & Wagner, B. (1983): The Precambrian metavolcano- Sedimentary Sequence eats of Ile and Ilesha S.E. Nigeria. A Nigerian greenstone belt? J. Afr. Earth Sci., 2 (2): 161–176.

Klemm, D. D., Scheider, W. & Wagner, B. (1984): The Precambrian metavolcano-Sedimentary sequence east of Ife and Ilesha southwest Nigeria"a Nigerian Greenstone belt"? J. Afr. Earth Sci., 2(2), 161–176.

Leeman, W. P. (1974): Experimental determination of partitioning of divalent cations between olivine and basaltic liquid. Ph. D. Thesis, University of Oregon.

Ludden, J. N. & Humphris, S. E. (1978): Are the rare earth elements mobile during alteration processes? Geol. Soc. Am. Abst. Prog., 10 447.

Ludden, J. N. & Thompson, G. (1978): Behaviour of rare earth elements during submarine weathering of tholeiitic basalts. Nature, 247: 147–149.

Ludden, J. N. & Thompson, G. (1979): An evaluation of rare earth elements during weathering of sea floor basalt. Earth Planet. Sci. Lett., 43: 85–92.

McCurry, P. (1976): The geology of the Precambrian to Lower Paleozoic rocks of Northern Nigeria-A review. In Kogbe C. A. (ed) Geology of Nigeria, Elizabethan pub. Co. (Lagos) Nigeria, 15–39.

Menzies, M. A. (1976): Rare earth geochemistry of fused alpine and ophiolitic Lherzolites, Othris, Lanzo and Troodos. Geochim. Cosmochim. Act., vol. 40, 645–656.

Naldrett, A.J. & Cabri, L. J. (1976): Ultramafic and related mafic rocks: their classificationand gensis with special reference to the concentration of nickel sulphides and platinum-group elements. Econ. Geol., 71, 113–115.

Ogezi, A. E. O. (1977): Geochemistry and geochronology of the basement rocks from the north western Nigeria. Ph. D. thesis, University of Leeds, 259.

Olabaniyi, S. O., Olarewaju, V. O., & Onabajo, O. O. (1989): PIXE analysis of Museum soap stone sculpture from Esie, south west Nigeria. International Centre for Theoreti-

cal Physic (ICTP).

Olade, M. A. & Elueze, A. A. (1979): Petrochemistry of Ilesa amphibolites and Precambrian crustal evolution in the Pan African domain of S.W. Nigeria. Precam. Res., 88: 308–318.

Olorunfemi, A. O. (2007): Mineralogical, geochemical and industrial application of talc deposits in Esie and environs, southwestern Nigeria. M. Sc. Thesis, Obafemi Awolowo University, Ile-Ife, 119.

Olorunfemi, A. O., Olarewaju, V. O., Okunlola,O. A. & Adesiyan, T. A. (2009): Compositional features industrial appraisal of talcose rock occurrence around Esie Southwestern Nigeria. Mineral Wealth 150/2009, 33–42.

Rahaman, M. A. (1976): Review of the basement complex of Nigeria in: Kogbe, C. A. (ed) Geology of Nigeria. Elizabethan publishing Lagos, Nigeria, 514.

Ringwood, A. E. (1975): Composition and Petrology of the Earth's Mantle. New York: McGraw-Hill.

Rollinson, H. R. (1993): Using geochemical data. Longman, New York, 343.

Sun, S. S. & Nesbitt, R. W. (1978): Petrogenesis of Archaean ultrabasic and basic volcanic: Evidence from the rare earth elements. Contrib. Mineral. Petrol., 65: 301–325.

Truswell, J. F. & Cope, R. N. (1963): The geology of parts of Niger and Zaria provinces, Northern Nigeria Bulletin Geological Survey of Nigeria, 29.

Wang, Y., Wang, J., Wang, L., Wang, Y. & Tu, C.(2004) REE Characteristics of the kalatongke Cu-NI deposit, Xinjiang,China. Journal of the Geological Society of China. Vol. 78, No 2.

Wood, D. A., Gilson, L. I. & Thompson, R. N. (1976): Elemental mobility during zeolite facies metamorphism of the tertiary basalts of eastern Iceland. Contrib. Mineral. Petrol.

The Cenkova tunnel construction with intermediate reinforced concrete wall

Gradnja predora Cenkova z vmesno armiranobetonsko steno

Jakob Likar[1, *]

[1]University of Ljubljana, Faculty of Natural Sciences and Engineering, Aškerčeva cesta 12, SI-1000 Ljubljana, Slovenia

*Corresponding author. E-mail: jakob.likar@ntf.uni-lj.si

Received: June 8, 2010 **Accepted:** September 8, 2010

Abstract: Basic design of the twin road tunnel with two traffic lanes with central reinforced concrete wall is a consequence of the short length of the tunnel and existing geological and geotechnical conditions, which build surrounding area and available space for motorway construction. The ground space, where tunnel was built, mainly consists of soil layers with clayey sands, silts and clays with different consistence. Besides the construction was carried out in difficult ground, the built of tunnel done step by step, included different construction phases. At the same time, permanent adaptation of excavation process and primary lining installing were adjusting to real geotechnical conditions. The central gallery with reinforced concrete wall was constructed first. Design of the construction is relatively stiff, because primary lining which was made by reinforced shotcrete at the both sides of the central reinforced concrete wall and connected with it. All construction elements were proved by numerical analyses which were carried out with 3D Finite Difference Method included space effect. The results of the geological observation and geotechnical measurements during construction of the central gallery and both tunnel tubes had shown that static resistant of the construction is adequate to all existing loads. During construction, the measurement on the surface had shown minimal movements which mean that method of construction was adequate.

Original scientific paper

Izvleček: Zasnova gradnje dvocevnega dvopasovnega predora z vmesno armirano betonsko steno je posledica kratke dolžine objekta, geološko-geotehničnih značilnosti hribin tega območja ter velikosti prostora, ki je na voljo za avtocestno povezavo. V pretežni meri se gradi na območju, ki je na nekaterih predelih plazovito ali pogojno stabilno, z zemljinskimi materiali, kot so zaglinjeni peski, melji in gline v različnih konsistentnih stanjih. Čeprav je gradnja potekala v zahtevnih hribinskih razmerah, je bila faznost gradnje upoštevana ob stalnem prilagajanju načina izkopa in primarnega podpiranja v dejanskih razmerah. Najprej je bil zgrajen vmesni rov z armirano betonsko steno, ki se je obenem uporabljal kot raziskovalni rov, kar je omogočilo natančno geološko in geotehnično spremljavo z namenom, da se ugotovijo dejanske geotehnične razmere gradnje. Konstrukcijska zasnova objekta je toga, saj sta obe primarni oblogi v bočnem in talnem delu na obeh straneh spojeni z vmesnim AB-stebrom. Vsi konstrukcijski elementi predora so bili predhodno statično preverjeni z uporabo metode končnih diferenc v prostoru (3D), tako da je bil upoštevan t. i. prostorski učinek. Geološko-geotehnična spremljava je pokazala, da je v statičnem pogledu načrtovana predorska konstrukcija zadoščala obtežbam, ki so bile posledica prerazporeditve napetostnih stanj med samo gradnjo. Prav tako so bili izmerjeni vplivi na površino nad predorom minimalni, kar pomeni, da je bil način gradnje ustrezen v danih hribinskih razmerah in kakovosten.

Key words: twin two lance road tunnel, reinforced concrete wall, tunneling in soil ground, geostatic 3D analysis, geotechnical measurement

Ključne besede: cestni dvocevni dvopasovni predor, gradnja predora v zemljinskih tleh, vmesna armiranobetonska stena, geostatične 3D-analize, geotehnične meritve

INTRODUCTION

Tunnel Cenkova is part of a motorway section between Maribor and the Hungarian border, subsection Sp. Senarska–Cogetinci. The distance between the tunnel axes is only 12 m, so for the first time in Slovenia, the structure of a tunnel with a middle pillar was designed. The length of the right tunnel tube is 370 m and length of the left tube is 363.80 m. The area above the tunnel is inhabited, so a number of analyses were carried out during the design. Figure 1 shows the tunnel layout.

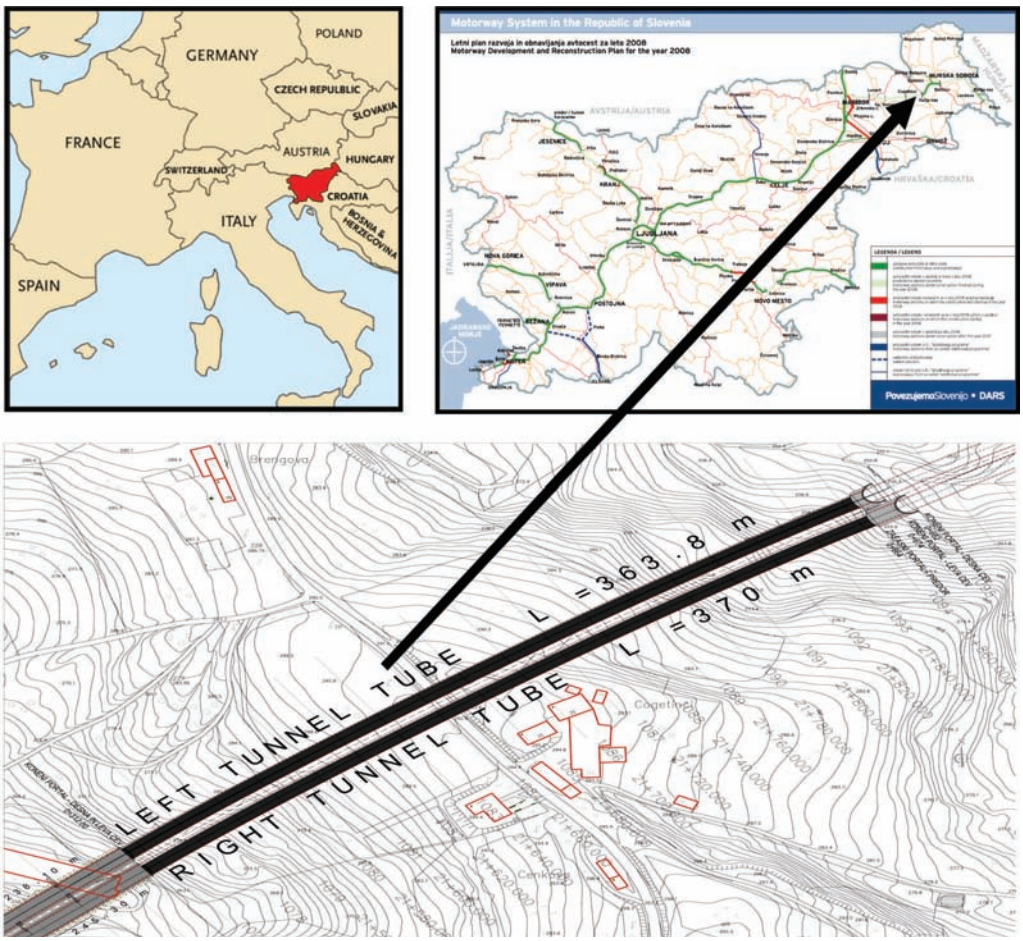

Figure 1. Layout of the tunnel Cenkova

Geological conditions in the tunnel foreseen in the tender

Upper Miocene clay, silt, sand, gravel and poorly lithified sandy marl were foreseen in the tunnel alignment (Tender, 2006). On the surface a few meters thick Plio-Quaternary layer of sandy clay, sand and gravel was foreseen (Figure 2). This region tectonically belongs to Slovenske gorice with fractures of direction NW-SE. Geotechnical characteristics of the sediment material from the tender are presented in Table 1.

Construction remarks

The small distance between the tunnel axis dictates that first a middle pillar

Table 1. Geotechnical properties of the sediment material foreseen in the TENDER (2006)

Chainage	Volume weight γ/(kN/m^3)	Uniaxial Compressive Strength q_u/kPa	Young Mod. E/MPa	Cohesion c'/kPa	Angle of friction φ'/°
21866-21750 (eastern portal)	19	200	110	2	19
21750-21545 tunnel	19	400	250	18	27
21545-21512 (western portal)	19	200	105	2	18

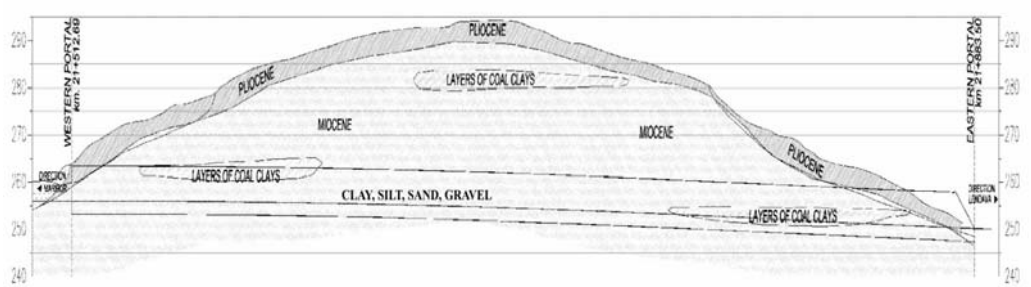

Figure 2. Tender geological longitudinal profile in the tunnel Cenkova (TENDER, 2006)

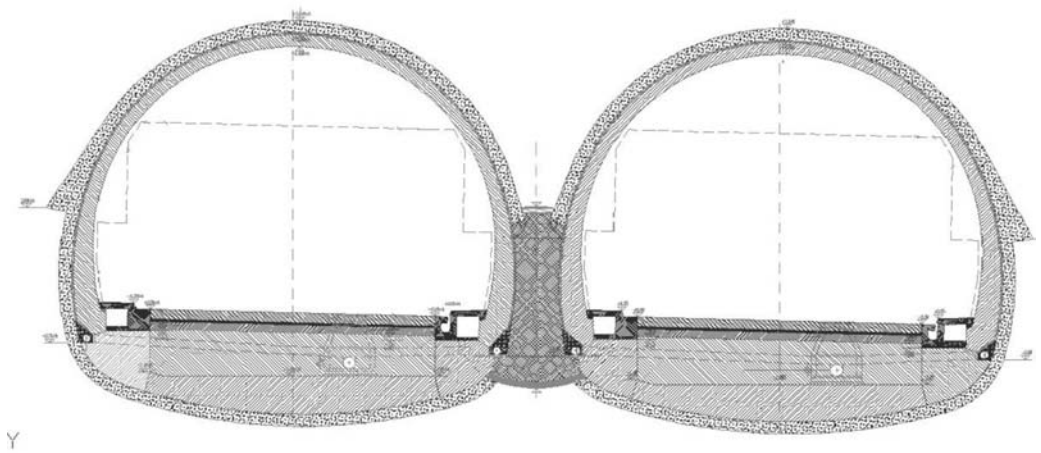

Figure 3. Characteristic cross-section of the tunnel Cenkova

must be constructed to insure the stability of the structure during the excavation phases and later during the exploitation. The pillar dimensions were defined according to the expected loads and available space for the construction. Height of the middle pillar is 3.50 m and the minimum width is 1.05 m. The ex-

cavation profile of the middle gallery, where the middle pillar is constructed, is about 16 m^2. Figure 3 shows the typical profile of the tunnel Cenkova.

To ensure the stability of the structure during the excavation phase and provide primary support, the shotcrete, installed during the top heading excavation, was placed on the top of the middle pillar in the left and right tubes. During the phase of the invert excavation, the shotcrete invert made a closure of the primary structure. Especially important are joints between top heading shotcrete and the top of the middle pillar and the joints of the abutment of the middle pillar and the tunnel shotcrete invert. The geometry of the structure is set to transfer the load from the left and right tubes, through shotcrete primary lining, to the middle pillar as a way to prevent overturning of the middle pillar in case of eccentric loading (excavation of one tube at the time) and the concentration of the stress in the middle pillar, which would cause the overloading of the structure.

Construction phases

First a middle gallery was constructed from the east portal to approximately half of the length of the tunnel. After that, the excavation of the middle gallery started from the west side and from the current face of the middle gallery toward the east abutment for the pillar and the middle pillar was constructed. Next the excavation of the top heading of the left and right tubes was carried out, with 16–32 m delay between excavation faces of the top heading in the left and right tubes. In this way the structure remained stable and the middle pillar was eccentrically loaded for the period not exceeding 14 days. The design provided the bench and invert excavation after finishing the top heading excavation in the left and right tubes.

Figure 4 shows the excavation phases as follows:

- Phase 1: Excavation of the middle gallery
- Phase 2: Abutment and middle pillar installation
- Phase 3: Excavation of the top heading in the left tube and support installation
- Phase 4: Excavation of the top heading in the right tube and support installation
- Phase 5: Excavation of the bench and invert in the left tube and support installation
- Phase 6: Excavation of the bench and invert in the right tube and support installation
- Phase 7: Inner lining and abutment installation
- Phase 8: Final construction of the tunnel

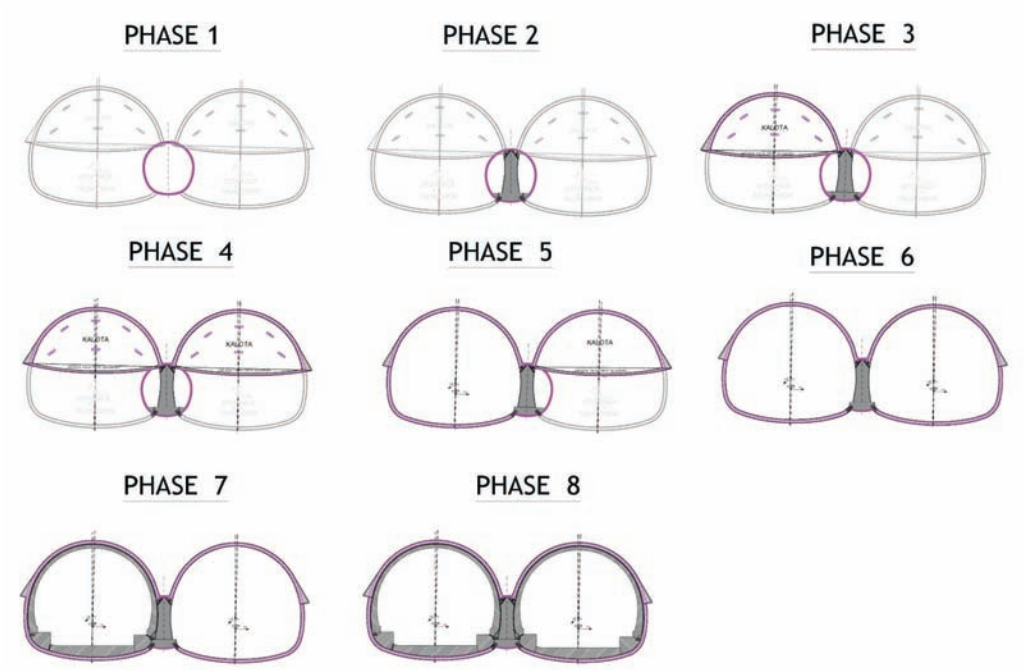

Figure 4. Phases of the tunnel construction

SUPPORT MEASURES

For the primary support in the main tunnel tubes a 30 cm thick and in the middle gallery a 20 cm thick reinforced shotcrete layer was foreseen in the Tender with steel arches and two layers of wire mesh, but actually the quantity of the shotcrete for the primary tunnel lining was increased by a factor 2.1 in some sections, due to unavoidable geological overbreaks. For the excavation of face support, the IBO anchors were installed, if required. To prevent overbreaks of sandy - silty sediments, installation of steel bars instead of steel laggings, was provided. Because the excavation phases in the top heading and the invert were at a reasonable distance, temporary shotcrete invert arch was provided in some sections to stabilize the top heading until the excavation of bench and invert.

NUMERICAL ANALYSIS

During the design phase, a number of analyses were carried out to determine the behavior of the structure and the influence of the tunnel excavation on the surface objects. Because 3D effect of the tunnel excavation should be important, one of the analyses was carried out using *FLAC*^{3D} (Itasca 2006).

The *FLAC*^{3D} analyses should provide the following parameters:

1 Expected deformation and loading of the support elements.
2 The effect of the tunnel excavation on the surface objects.
3 Loads in the middle pillar in case of eccentric loading (only one tube excavated at the time) and final loading.

Mesh geometry

The stability of this type of structure highly depends on the details like excavation phases, support installation and joints between the shotcrete and the middle pillar. As a result, detailed mesh geometry around the tunnel structure area is required. The mesh must allow the surface settlement calculation so the mesh must be created to the top of the surface in such way that boundary conditions don't affect surface deformation results in the objects area.

To take these requirements into account, mesh of the area between chainages 0+460 and 0+535 e.c. 75 m long was created. Figure 5 shows the mesh geometry of the tunnel structure. Note that the surface of the mesh matches surface geometry. The mesh is then 75 m long, approximately 75 m high and 150 m wide. To set the number of elements to allow relatively fast calculation, a 5 m long excavation step is chosen. The model consists of approximately 50,000 elements. The geometry allows the simulation of construction phases 1 to 6.

Support considered for the numerical analysis

For the support, only the shotcrete has been taken into account as shown in Figure 6. The shotcrete has been simulated using shell elements, with properties and dimensions shown in Table 2.

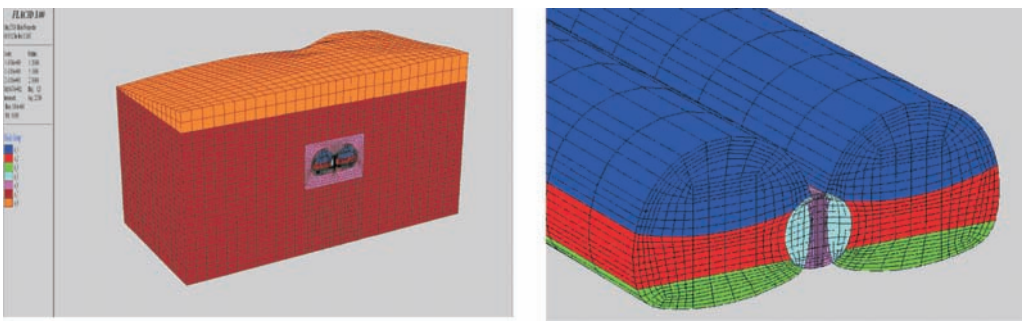

Figure 5. Input geometry

Table 2. Properties of the tunnel support used in the numerical simulation of tunnel construction.

Object	Type	Elastic modulus (MPa)	Thickness (m)
Middle gallery	Shell elements	3000	0.2
Left & right top heading, bench & invert	Shell elements	3000	0.3
Temporary invert in top heading, left & right tube	Shell elements	3000	0.2

Table 3. Simulation of the tunnel construction sequences

Object	Task	Steps	Comment
Middle gallery	Excavation & support	15	Support (shell elements) is installed 1 step (5 m) behind the excavation face.
Middle pillar & abutment	Installation	1	Middle pillar and abutment consist of finite difference elements.
Excavation & support of the left top heading	Excavation & support	15	Support (shell elements) is installed 1 step (5 m) behind the excavation face. Support consists of shells in top heading and temporary invert. Shells, installed as the middle gallery support, are deleted at area of middle pillar-top heading support joints.
Excavation & support of the right top heading	Excavation & support	15	The construction sequence is the same as in the previous sequence. Support (shell elements) is installed 1 step (5 m) behind the excavation face. Support consists of shells in top heading and temporary invert. Shells, installed as the middle gallery support, are deleted at area of middle pillar-top heading support joints.
Excavation & support of the left bench and invert	Excavation & support	15	Support (shell elements) is installed 1 step (5 m) behind the excavation face. Support consists of shells in bench and invert. Shells, installed as the middle gallery support, are deleted at area of middle pillar-invert support joints.
Excavation & support of the right bench	Excavation & support	15	The construction sequence is the same as in the previous sequence. Support (shell elements) is installed 1 step (5 m) behind the excavation face. Support consists of shells in bench and invert. Shells, installed as the middle gallery support, are deleted at area of middle pillar-invert support joints.

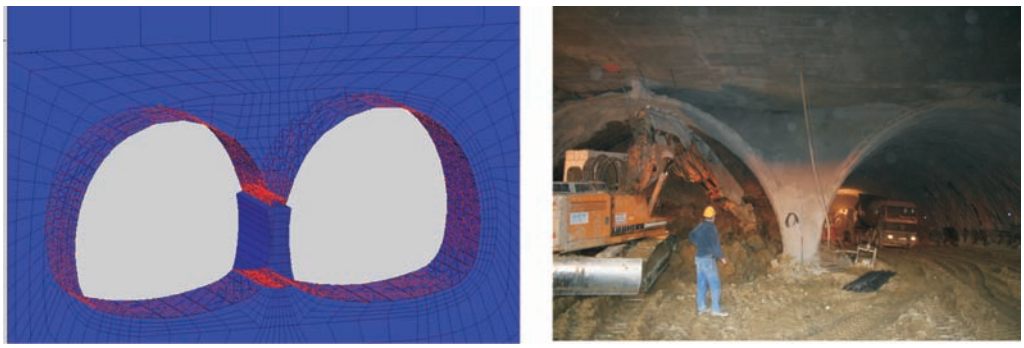

Figure 6. Support of the tunnel (shell element)

Simulation of the tunnel construction sequences

Simulation steps generally follow the tunnel construction phases from 1 to 6. The excavation sequences are presented in Table 3. All together 76 steps were carried out. At each step the prescribed unbalance force was reached.

Results of the numerical analyses

Calculated tunnel deformation and ground loading of the support

Deformations occurring after the middle gallery excavation, reached values of approximately 1.5 cm in the middle gallery top heading. The surface deformations were minor. Deformations after excavation of the left tube top heading reached values of approximately 4 cm. A similar level of deformations was measured after the right tube top heading excavation and the increase of the deformation in the left tube because of the right tube excavation was not considerable.

Excavation of the bench and the invert in both tubes caused the deformation of several centimeters in the invert, but it did not significantly affect the deformations in the top heading. The deformation contours around the tunnel structure are presented in Figure 7.

Moments, axial and shear forces did not exceed the limit values, except at the joint between shotcrete and the middle pillar. Thus reinforcement was provided in that area.

Calculated Surface deformation

Surface deformations after the middle gallery excavation were negligible. The final calculated surface deformation reached a value between 3–4 cm above the middle gallery axis. Under the objects, the deformations reached values of about 1.5 cm. Most of these deformations were consequences of

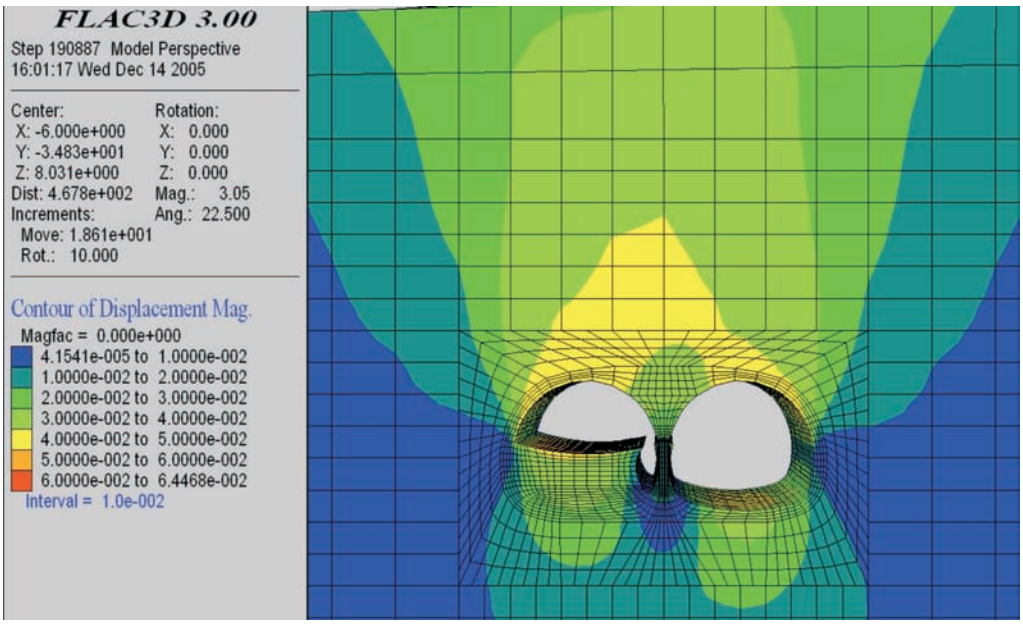

Figure 7. Deformations around the tunnel (after left tunnel tube top heading excavation finished)

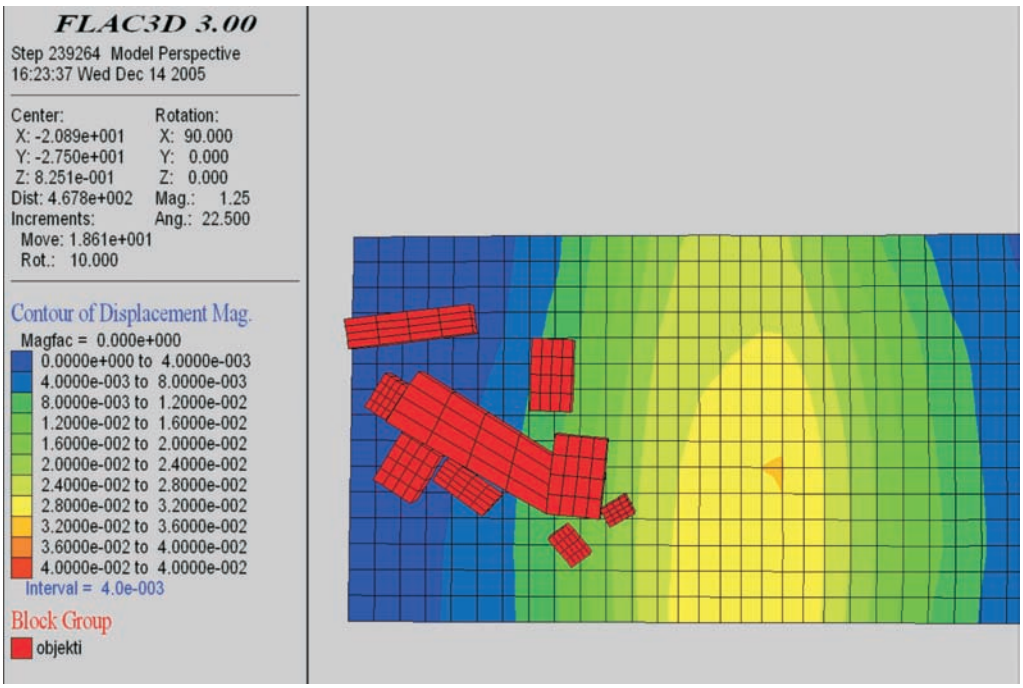

Figure 8. Calculated surface displacement

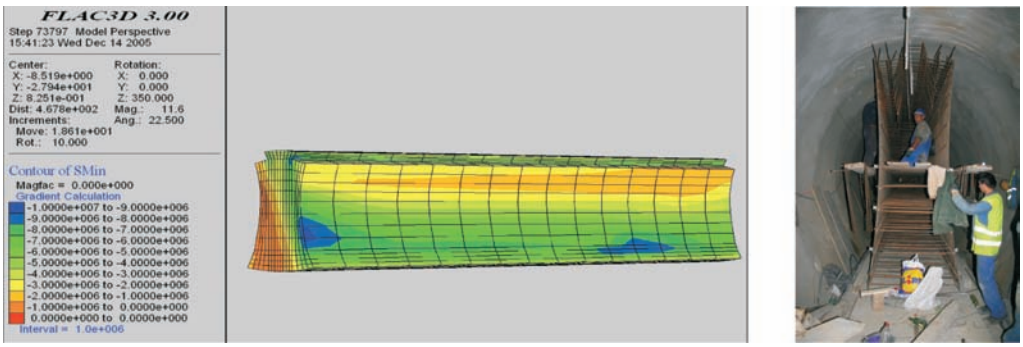

Figure 9. Contours of stresses SMin (excavated one tube only)

top heading excavation of the left and right tubes.

The deformations reached the objects when the excavation face was approximately 30 m away. The deformation field on the surface is shown in Figure 8. Note that elements which show the objects position are not a part of the simulation.

Simulation of the middle pillar loading

Figure 9 shows the stress state in the middle reinforced concrete wall after eccentric loading (excavation of only left tunnel tube). Maximum compressive stress in the pillar is approximately 10 MPa. About 1/3 of the middle pillar on other side is practically unloaded. Maximum tension stress in the middle pillar reaches values of about 0.5 MPa. The maximum stress reached values approximately 15 MPa after the tunnel was fully constructed. All values were below the limit values.

Geological conditions observed during the tunnel excavation

Miocene sediments in the tunnel alignment were composed of sand, silty sand, clayey sand, silt, sandy silt, clay and clayey silt. Figure 10 shows a section of interpreted geological longitudinal profile of the left tunnel tube on the chainages between 21740 and 21780. In clayey – silty layers also thin layers (up to 0.5 m thick) of black lignitified organic material were found too. General inclination of the layers was SE; 140/10. Normal gravitational fractures were found mainly in the region of both portals, which were formed due to the creeping soil slope. Two main groups of cracks were found with inclinations: SWW; 200–260/60–80 and SES; 120–170/55–65. Occasionally also cracks with inclinations: NW; 300–340/45–85 and NE; 22–72/80 occurred.

One possibility of overbreak occurrences was in the connection excava-

tion with water filled layers of sand and in similar cases. Actually, the water was present locally only in the form of water drops where water did not exceed 0.05 l/s.

Two main geotechnical behavior types (BT) of sediments were found during the excavation of unsupported ground (Elea-iC, 2008). Behavior type BT3 (Figure 11b) indicates the regions where shallow shear overbreaks due to the burden, in combination with overbreaks due to the gravity and due to the discontinuities could occurred, while BT8 (Figure 11a) indicates the regions where a flow of sediment material with no cohesion or very low cohesion value could

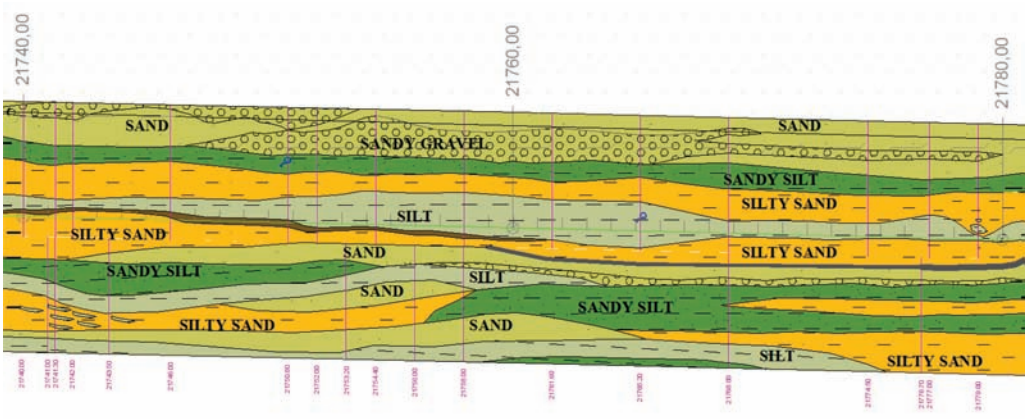

Figure 10. Actual geological longitudinal profile of the left tunnel tube on the chainages between 21740 and 21780 (Elea iC 2008)

Figure 11. Flow of sand from the ceiling of the top heading (BT8) in the right tube at the ch. 21672 (a) and the top heading in the right tube at the ch. 21659 (b), which indicates consequences of shallow shear overbreak due to discontinuities (BT3) on the right side of the excavation face.

occurred. Regions with behavior types in the middle gallery, left and right tunnel tubes are presented in Figure 12.

Very low cohesion of the sand layers and intensity of secondary stress states around tunnel tubes were caused several geological overbreaks of volume 4–60 m^3 occurred during the excavation of the eastern part of the middle gallery and both main tunnel tubes in the area of the portal.

These overbreaks occurred in spite that the primary tunnel lining was installed on time. Unavoidable overbreaks sometimes continued also during the shotcrete installation, in the phase before the shotcrete got adequate compressive strength. The fact is, that foreseen cohesion values of the sediments on the 60 % length of the tunnel (chainages between 21545 and 21750 in the Table 1) were substantial higher (c' = 18 kPa, φ' = 27°) than those measured in the laboratory in the sediment samples from this part of the tunnel (c' = 0–10 kPa, φ' = 35°–38°), which means that in these parts unpredictable physical conditions were encountered. For this reason, the excavation methods and the primary tunnel lining were adjusted to the actual geotechnical conditions. Therefore, the tunnel excavation

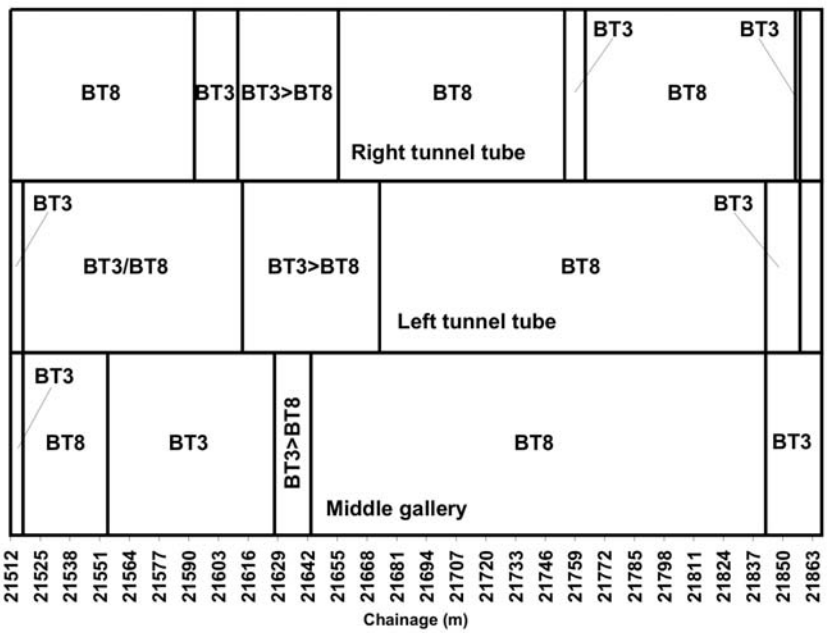

Figure 12. Behavior types (BT) in the middle gallery, in the left and right tunnel tube. BT3 > BT8 indicates that the main type is BT3, subordinated by BT8. BT3/BT8 means BT3 mixed with BT8 (Elea iC 2008)

was performed in several phases. In spite that overbreaks occurred during the tunnel excavation, actual displacements in the tunnel did not exceed foreseen deformation tolerance.

MEASURED DISPLACEMENTS IN THE TUNNEL CONSTRUCTION

Method of measuring displacement of the measuring points installed in the primary

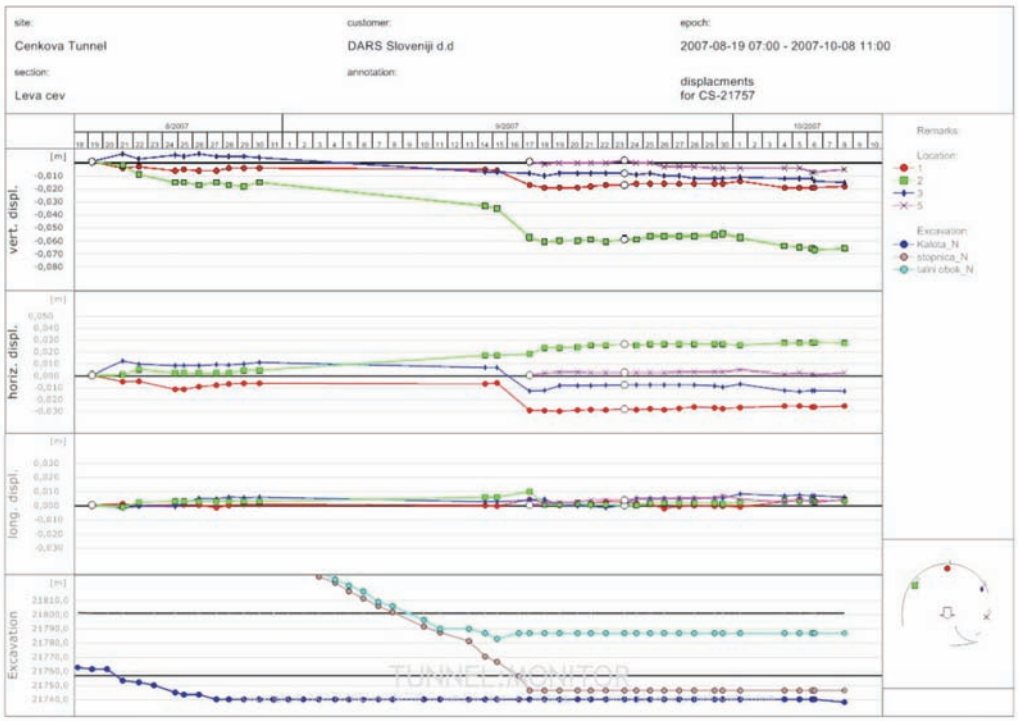

Figure 13. Diagram of measured displacements in the left tunnel tube at the chainage 21757 (Elea iC, 2008)

Figure 14. Tunnel Cenkova in phase of construction and after it on operation

lining based on geodetic instruction used special automatic theodolite. In different location in the tunnel tubes including central gallery, the measures were taken. Maximal vertical displacements in the top heading of the middle gallery was measured up to 4.6 cm. Maximal horizontal movements did not exceed 2.2 cm.

Average value of maximal vertical displacements in the top heading of the left tunnel tube was 4 cm. In the Figure 13 diagram of displacements versus time is shown for the left tunnel tube on the chainage 21757.

Average value of maximal vertical displacements in the top heading of the right tunnel tube was about 4 cm. Maximal vertical displacements in the top heading of the right tunnel tube of up to 13.3 cm were measured on the chainages 21520. Maximal horizontal displacements in the top heading of the right tunnel tube of up to 5.9 cm were measured on the chainage 21532 In spite that many geological overbreaks occurred during the tunnel excavation, actual maximal displacements in the tunnel did not exceed foreseen deformation tolerance, which indicates that the method of construction was adequate.

Comparison between calculated and actual deformations

The measured values of deformations in the tunnel did not exceed the calculated values. The typical deformation level after tunnel excavation was from 4 cm to 6 cm, which is a good fit to the calculated results. Surface deformation was also below calculated results based on 3D model. During the tunnel construction and after it, no deformation on the houses on the surface, caused by tunnel construction, have not been detected.

Conclusion

- Tunnel Cenkova is the first tunnel in Slovenia constructed as a two-tube tunnel with a middle pillar as part of the structure in the soft soil ground (Figure 14).
- The geological and geotechnical conditions with sediment layers are relatively demanding. The tunnel is constructed in an inhabited area, which needs special attention and continued control of deformations in the tunnel and on the ground surface.
- Because of this, during the design some additional calculations and analysis were carried out, including *FLAC*^{3D} numerical analyses, which answered questions about the middle pillar loading. The level of possible deformations in the tunnel structure and on the surface was calculated as well. These numerical analyses indicate that calculated deformations are in good agreement with measured deformations in the tunnel.

- In spite that many geological overbreaks occurred during the tunnel excavation, actual maximal displacements in the tunnel did not exceed foreseen deformation tolerance, which indicates that the method of construction was adequate.

Acknowledgement

Author would like to give many thanks to client DARS, d. d., for their financial support for realization of the tunnel project and also many thanks to main contractor SCT, d. d., for correct collaboration during tunnel construction.

References

KARAKUS, M. (2006): Appraising the methods accounting for 3D tunnelling effects in 2D plain strain FE analysis, Tunnelling and Underground Space Technology, Elsevier, pp.10.

KIM, H. J., EISENSTEIN, Z. (1998): Prediction of lining loads from case histories. World Tunnel Congress'98, Sao Paolo, Brazil, pp. 299–304.

VIŽINTIN, GORAN, VESELIČ, MIRAN, BOMBAČ, ANDREJ, DERVARIČ, EVGEN, LIKAR, JAKOB, VUKELIČ, ŽELJKO (2009a): The development of a "drive-in" filters dewatering system in the Velenje coal mine using finite-element modelling. *Acta geotech. Slov.*, 2009a, Vol. 6, 1, p. 50–63.

VIŽINTIN, GORAN, SOUVENT, PETRA, VESELIČ, MIRAN, ČENČUR CURK, BARBARA (2009B): Determination of urban groundwater pollution in alluvial aquifer using linked process models considering urban water cycle. J. Hydrol. (Amst.). [Print ed.], 2009b, issues 3–4, vol. 377, str. 261–273.

WHITTAKER, B. N., FRITH, R. C. (1990): Tunnelling-Design, Stability and Construction. The Institution of Mining and Metallurgy, London.

WITTKE, W. (2000): Stability Analysis for Tunnels. Fundamentals.Verlag Glückauf GmbH. Essen.

WITTKE, W. (2002): Statik und Konstruktion der Spritzbetonbauweise. Verlag Glückauf GmbH. Essen.

Itasca Consulting Group, Inc. (2006) *FLAC^{3D} – Fast Lagrangian Analysis of Continua in 3 Dimensions, Ver. 3.1, User's Manual*. Minneapolis: Itasca

Building Permission Design, (2005–2006): Geoportal, d. o. o., Ljubljana, Slovenia.

Excavation Design, (2006–2007): Geoportal, d. o. o., Ljubljana, Slovenia.

Tender for the tunnel Cenkova, Sp. Senarska – Cogetinci motorway (2006): DARS, d. d., Ljubljana, Slovenia

Construction diary for the tunnel Cenkova (2007–2008), SCT, d. d.

Geological – geotechnical reports for the tunnel Cenkova construction,(2007–2008) Elea – iC.

Final geological – geotechnical report for the tunnel Cenkova (2008) Elea – iC.

Use of electronic initiation systems in mining industry

Uporaba elektronskih inicialnih sistemov v rudarstvu

Jože Kortnik[1, *], Julijan Bratun[2]

[1]University of Ljubljana, Faculty of Natural Sciences and Engineering, Department of Geotechnology and Mining, Aškerčeva 12, SI-1000 Ljubljana, Slovenia
[2]ECONO d. o. o., Dimičeva ulica 16, SI-1000 Ljubljana, Slovenia

*Corresponding author. E-mail: joze.kortnik@ntf.uni-lj.si

Received: June 8, 2010 **Accepted:** June 16, 2010

Abstract: The use of explosives for minerals extraction has always been a highly contentious area. The associated environmental impact is frequently an issue that curtails the sustainable development of many quarrying operations. However blasting is quite often the only economic means of mineral extraction. It is therefore vital for the industry to do all that it can to reduce the vibration levels experienced at adjacent properties due to quarry blasting without imperilling the financial viability of the enterprise. Over the past twenty years we haven't seen any major development in initiation technology, with the last major development being the release of the Nonel detonation system in 1973. By more accurately controlling timing delays, electronic initiation detonator systems can increase rock fragmentation, lower vibration levels, reduce oversize; lessen the potential fly-rock. This translates into faster excavation times and improves downstream processing costs for the mining operation by increasing throughput, reducing crusher wear and lowering power consumption and maintenance costs. The purpose of this paper was to examine the use of Electronic Detonators and their relevance in to the Slovenian mining industry.

Povzetek: Uporaba minsko razstrelilnih sredstev pri pridobivanju mineralnih surovin je imela vedno poseben dvorezen pomen/vlogo. S tem povezan negativni vpliv na okolje je bil zato pogosto predmet zmanjševanja njihove uporabe v rudarskih pridobivalnih de-

Original scientific paper

lih v smislu trajnostnega razvoja. Kakor koli že, uporaba metode razstreljevanja omogoča velike ekonomske učinke pri pridobivanju mineralnih surovin in je zato zelo zaželena. Prav tako ima poseben pomen tudi za preostalo industrijo, še posebej zaradi možnosti zmanjševanja današnjih seizmičnih vplivov pri miniranjih v kamnolomih brez posebnih finančnih učinkov na poslovanje. V preteklih dvajsetih letih ni bil opazen znaten napredek na področju inicialnih tehnologij, kjer je bil zadnji večji razvoj zaznan z odkritjem neelektričnega inicialnega sistema Nonel leta 1973. Z bolj natančnim nadzorom časa zakasnitve detonacije lahko z uporabo elektronskih inicialnih sistemov dosežemo izboljšanje fragmentacije/granulacije materiala po razstreljevanju, nižji nivo seizmičnih valov, zmanjšanje prevelikih kosov in zmanjšanje potencialne nevarnosti razmeta materiala. To posledično omogoča učinkovitejši čas pridobivanja in s tem zniževanje stroškov pridobivanja, drobljenja in mletja zaradi manjše obrabe strojih delov, porabe energije in vzdrževanja. Namen članka je predstaviti elektronske detonatorje in pomen uporabe za slovensko rudarsko industrijo.

Key words: electronic detonator, electronic initiation system
Ključne besede: elektronski detonator, elektronski inicialni sistem

INTRODUCTION

The mining and explosive industries rapidly embracing new technologies, in order to improve overall performance, efficiency and cost-effectiveness in various types of blasting and also to mitigate its adverse effects. Most recently, technology that is developed to improve techno-economics and reduction of most of adverse effects in usage of explosive and blasting is »Precise and Accurate Delay Timing - Digital or Electronic Detonator« system.[3]

Broadly speaking, accurate and flexible timing allows blasters to make small hole-to-hole and row-to-row changes to account for drilling inaccuracies. Adjusting the blast design to actual conditions can improve safety and fragmentation, which can cut costs by optimizing the loading and hauling cycle, increasing crusher throughput, and reducing the amount of oversize handling and secondary breaking. In addition, precise and variable delay timing manipulations have enhanced highwall stability and bench crest preserva-

tion, resulting in safer mines operations and also for reduction of blast induced ground vibration. These improvements allow for more accurate placement of boreholes for succeeding blasts. Thus, the precision in delay timing has advantages such as:

- Better ground vibration control,
- Better control of rock movement and muck profile,
- Better fragmentation,
- Enhancement in productivity by optimizing utilization of explosive energy.

Mining activities remain a time and cost-intensive business therefore, accurate planning, cost efficiency have been the important factor in excavation operations. In a move to improve overall cost-efficiency in large mining and construction operations operator are adopting the use of Electronic Detonation blasting technology. The accuracy and flexibility of the programmable detonator have provided the mining industry with options, previously not available to improve timing designs for increased benefit in the areas of ground control and better fragmentation. The industry's whole approach to blast timing design can now be focused on greater safety, increased productivity and blast performance, rather than being restricted by the limited interval selections and inaccuracies the conventional pyrotechnics timing systems offer. The growing popularity of high-accuracy electronic detonators means the potential for an expansion of a quarry blasting program's capabilities and improved safety as well.

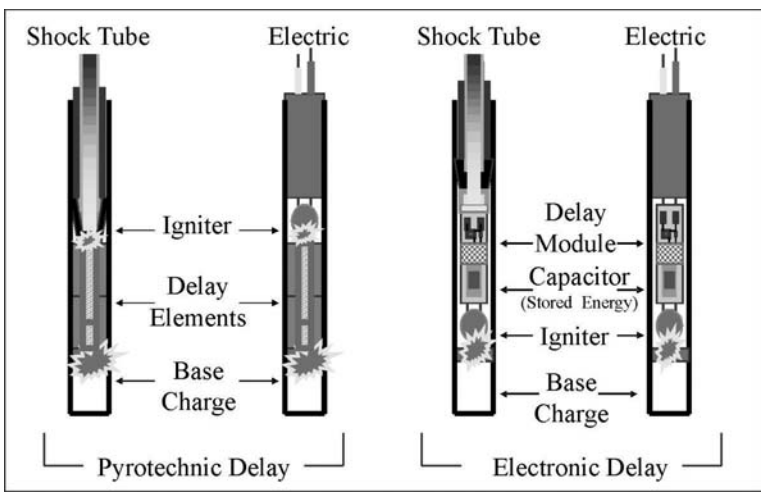

Figure 1. Pyrotechnic and Electronic delay initiation system[9]

UNDERSTANDING ELECTRONIC DELAY INITIATION SYSTEM

In order to understand the Electronic delay initiation system, we compare Pyrotechnic system and Electronic delay initiation system. There are several types of electronic systems being tested and used in the mining industry, all of which utilize some type of stored energy device to provide energy for their timing and firing circuits. All Electronic Detonators has a system to store electrical energy inside the detonator as a means of providing delay timing and initiation energy.

Fundamental Construction Differences[3]:

- Basic differences in Electronic Delay with Pyrotechnic system of delay is in location of Ignitor/Fuse head,
- In Electronic Detonator Ignitor/ Fuse head is located below delay (timing) module,
- In Pyrotechnic system (Shock Tube and Electronic Detonator) Ignitor/ Fuse head is located ahead of Delay elements.

One of the basic differences in electronic delay with pyrotechnic system of delay lies in the location of Igniter. In electronic detonator the Igniter is located below the delay (timing) module, whereas both shock tube and electric detonator (Figure 1) utilizes the igniter ahead of delay element (shock tube function as igniter in the shock tube device). Other basic difference in design of electronic detonator is the use of some type of stored electrical energy device, typically capacitor, is used

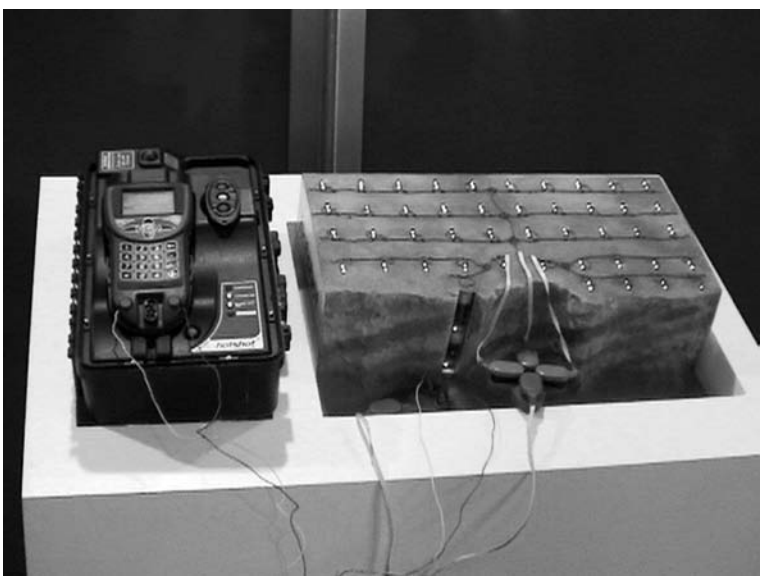

Figure 2. Electronic blasting system (DynoNobel HotShot)

in the delay module. The construction and design of electronic detonator varies from manufacturer to manufacturer.

In case of electronic detonator which utilizes standard shock tube lead as the input signal, it transforms into electrical pulse through the use of a small explosive charge (booster) coupled to a highly efficient piezo ceramic element (generator) and (electrical energy storage cell (capacitor). Upon receipt of a thermal signal from shock tube the small explosive charge in the booster detonator fires. This activates the piezo ceramic device, which in turn causes current to flow through the steering diode to charge storage capacitor. A voltage regulator provides a sustantially constant voltage source to oscillator to control the frequency (Example of this kind of system is DIGIDET™ or Ensign-Bickford, USA)

The Programmable electronic detonator (Figure 3) utilizes standard lead as the input signal, which is transformed into electrical pulse through the use of principal component. Upon receipt of an electric signal causes current to flow through the steering diode to charge storage capacitor. A voltage regulator provides a substantially constant voltage source to oscillator to control the frequency. A "power on reset" circuit preloads the counter upon the initial application of the input voltage. Once the voltage on the storage capacitor has increased beyond a threshold setting the counter begin decrementing upon each input pulse from oscillator. As the counter digitally decrement past zero, the output to the firing switch activate and all remaining energy in the storage capacitor flows to the igniter. The end result is an electronic delay detonator.

Electronic detonator

There are several types of electronics systems, all of which utilize some type of stored electrical energy device (e.g. capacitor) to provide energy for their firing or timing/firing circuits. Their differences include detonator construction, timing precision, communication protocol, blasting machines, tie-in, connectors, etc. Although they are each uniquely different from one another, there are certain design features that are common to all. It is essential that users become fully educated on the products, procedures and recommended practices prior to use.

Electronic detonator systems are grouped into two basic categories:

- Factory Programmed Systems (fixed delay) and
- Field Programmed Systems (variable delay).

Factory Programmed Systems, in most cases, have a close resemblance to the conventional hardware and compo-

nents found with standard electric detonators. In some cases, the user may even have a difficult time differentiating a wired electronic detonator from a wired electric detonator. Even though these units may not appear to be different, electronic detonators generally cannot be fired or shot using conventional blasting machines or firing devices. Each system can have a unique firing code or communication protocol used to fire the detonators in the blast.

Factory Programmed Systems can be further grouped into specific types or styles. There are Electrically Wired Systems, where each manufacturer has a specific wiring style or methodology; and Factory Programmed Systems that utilize shock tube technology to energize an electronic timing circuit within the detonator.

Factory Programmed Systems

Factory Programmed Systems utilize "fixed" delay periods for the blast design. Holes are generally loaded and hooked up in the same manner as standard electric or shock tube systems. Depending on the manufacturer, some type of surface connector may be utilized for ease of wiring, or maintenance of correct electrical polarity. With some systems, correct polarity must be observed when electronic detonators are attached to the firing circuit, otherwise a misfire may occur. In all cases though, users of these systems should always consult the manufacturer for specific application information and instructions.

Field Programmed Systems

Field Programmed Systems utilize electronic technology to program delay times at the blast site. Each system is manufactured for, or with, unique system architectures, styles, hardware and communication protocol. There are no fixed delay times associated with these detonators. These systems rely on direct communication with the detonator (either prior to loading, after loading, or just prior to firing) for the proper delay time and subsequent blast design. In general, these systems will utilize some type of electronic memory, which allows them to be reprogrammed at any time up until the fire command is given.

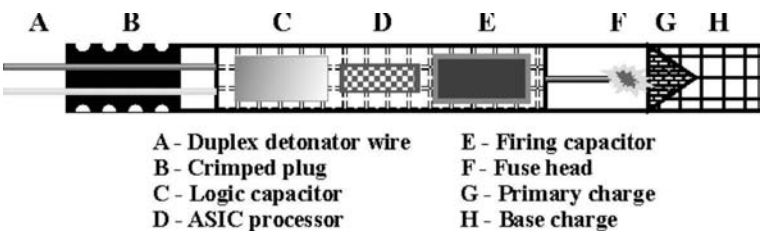

Figure 3. Cross section of Programmable Electronic Detonator

Significance of accuracy of delay timing

The pyrotechnic detonator design is such that the average scatter of delayed firing is ±10 %. This implies that for a blast-hole that should fire at 25 ms from initiation, might fire at 22.5 ms or 27.5 ms. This may not seem like a huge variance, but the resultant effect is. The scatter on a 500 ms delay detonator will cause it to fire anytime from 450 ms to 550 ms i.e. a range of 100 ms. If taken into account that inter-hole delays of 10 ms are used on a blast, out of sequence hole firing is almost guaranteed.

In general, accurate and flexible timing allows blasters to make small hole-to-hole and row-to-row changes to account for drilling inaccuracies. Adjusting the blast design to actual conditions can improve safety and fragmentation, which can cut costs by optimizing the loading and hauling cycle, increasing crusher throughout and reducing the amount of oversize handling and secondary breaking. In addition, precise and variable delay timing manipulations enhances high-wall stability and bench crest preservation resulting in safer mines operations and also for reduction of blast induced ground vibration. These improvements allow for more accurate placement of boreholes for succeeding blasts. Optimization of the blast design to take greater advantage of the electronic detonator's precision expands the blast pattern and reduces the explosive consumption without negatively affecting production. Electronic detonators generally are programmable in 1ms increments and have delay accuracy (scattering) as small as ±0.5 ms.

The control of blast vibrations is an increasingly important factor within the rock blasting industry. Much research work has looked at optimising the inter-hole delay period to minimize vibration. The most commonly used technique utilising inter-hole delays is Linear Superposition. This is a method whereby a vibration signal from a single-hole shot is combined with the firing times to simulate the vibration signal generated by a full-scale production blast. The simulation can be run many times with varying delay times to find the optimum value which will produce the minimum vibration level. Reamer et al. [10] give a very good description of this technique.

The successful implementation of Linear Superposition relies on two very important assumptions:

- The firing time of each hole can be accurately controlled.
- The single-hole vibration signal is a good representation of the vibration produced by each hole in a production blast.

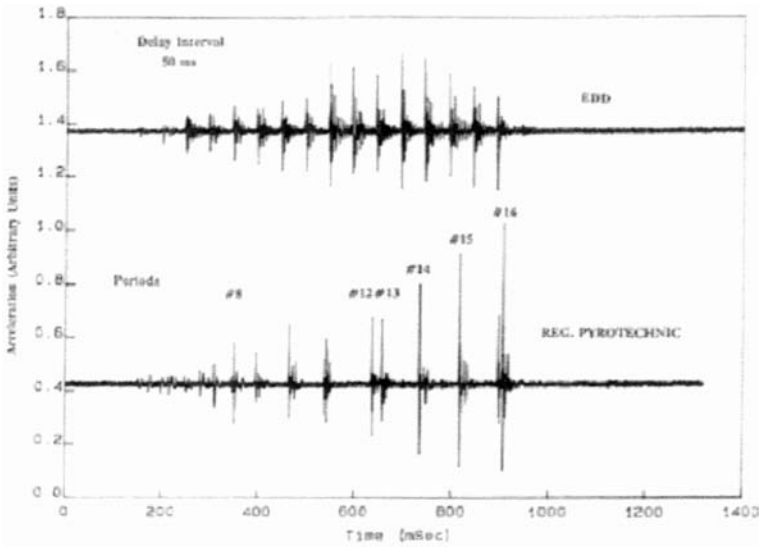

Figure 4. Comparison of firing times between electronic delays (ED) an the regular pyrotechnic delays (SP) for the same 50 ms delay interval in quarry blasts (three holes/delay in an echelon design)[6]

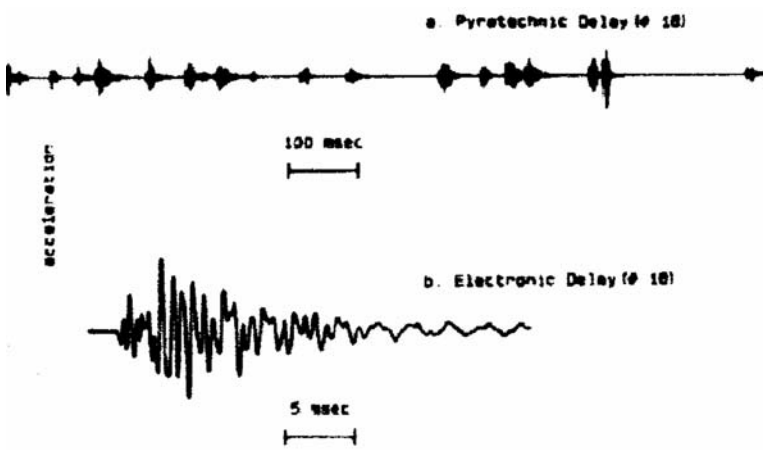

Figure 5. Comparison of hole firing times for regular pyrotechnic and electronic delay for the sixteen perimeter holes connected to the same delay[6]

Initiation timing can now be accurately controlled with the advent of electronically delayed detonators and accurately determined by using very high speed solid state data loggers to record "Velocity of Detonation" (VOD) information.

The assumption that the single-hole test shot provides a vibration signal that is representative of all the holes in a production shot is more problematic.

Yuill & Farnfield[7] found that, whilst vibration signals from a series of single-hole shots are consistent in shape despite variations in the hole design and explosive type, the amplitude of the vibrations was variable. They went on to state that the instantaneous charge weight; free faces and burden controlled the amplitude of these vibrations.

Whittaker, Chiappetta & Stump[8] found that in the near field, vibration amplitudes and dominant frequencies were significantly affected by using decked charges over full column charges, for a given explosive. They also showed that the results are very site specific and only apply to the near field, once a critical distance is exceeded no significant differences are found regarding the dominant frequencies or vibration amplitudes.

Birch & Hosein[2] indicated that different holes in any given small blast perform a slightly different function that will inevitably have an effect in the final vibration signal produced. They also demonstrated it was possible to deconstruct the blast signals in such a way as to show that the timing times did have an effect on the wave shape of the vibration and that the different timings did produce differing amplitudes of vibration.

To provide comparison between the different blasts a measurement termed the 'Scaled Distance – SD' was used. This is a value which represents the distance of the seismograph from the centre of the blast while taking into account the maximum instantaneous charge detonated therefore providing a comparable situation. The formula used for the calculation of scaled distance was taken as is shown below as it is the standard used in many publications.[1]

$$SD = \frac{D}{MIC^a} \tag{1}$$

$$PPV = H \cdot (SD)^b \tag{2}$$

where;
SD – scaled distance (m/kg^a)
D – distance to the centre of the blast (m)
MIC – maximum instantaneous charge (kg)
a – charge weight exponent
PPV – peak particle velocities (mm/s)
H – particle velocity intercept.
b – slope factor exponent

The empirically determined values in equations for H, a, and b for each of the three components of motion longitudinal, vertical, and transverse. Charge weight and distance are the principal factors that affect vibrations and are subject to control. The values of a, b and H are dependent on rock type, rock density, rock bedding, slope of beds, thickness of over burden, nature of terrain, blasthole conditions, presence or absence of water.[11] They also affect the transmission of vibrations, but are beyond control. The values of $a = 0.5$ and $b = -1.6$ are generally accepted as workable first approximations until applicable data indicate a change. The value of $H = 438$, however, is highly variable and is influenced by varying factors.

Figure 6. illustrates five resultant traces (two Non-electric and three Electronic) recorded at the same monitoring location. The peak resultant values for the non-electric traces appear close to the begining of the signal traces with the levels reached being unmatched through out the rest of the traces. In comparison the peak resultant values for the electronic traces are more randomly distributed throughout the entire duration of their signal traces. All the peaks throughout the electronic traces appear to be more regularly distributed than the non-electric with the actual peak values appearing to be only slightly higher than what could be considered to be the average peak values for a given blast.[4]

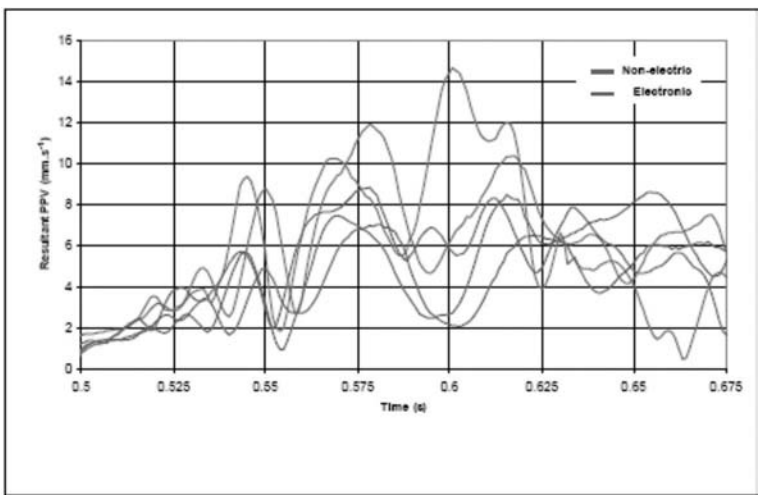

Figure 6. Comparison of hole firing times for two Non-electric and three Electronic traces (PPV - peak particle velocities measured in millimetres per second)[4]

Conclusions and plans for future work

The indication from the literature is that Electronic Initiation Systems will offer benefits in ground vibration control, fragmentation control, muck pile contours, reduction in fly rock incidents, increase possible round sizes and presents an opportunities to develop new blasting methods. Of course with all new technology the benefits are offset to some extent by the drawbacks and electronic initiation is no exception.

Electronic initiations have problems in that they can be very complex systems, which require lengthy training and are much more expensive than Nonel Detonators, also the complexity of the systems increases the possible sources of risk of malfunction. As most of these systems are still being developed and proven there is still room to address these issues, the first two are economic which is a site-specific decision where as the third is an issue of safety. Safety is not site specific and should be inherent in any new technology that it has a higher level of safety than the superseded technology.

The conclusion was that technically and operationally the electronic systems seem vary proficient and from the results of the various tests and case studies that have been carried out they have a great deal of benefit to offer the Slovenian mining industry.

References

[1] Bolinger, G. A. (1971): Blast vibration analysis, Illinois, US: Southern Illinois University Press, pp. 95–96, 26.

[2] Birch, W. J. & Hosein, S. (2004): *The* Application of Electronic Detonators in Controlling Blast Vibrations – A Trial Study, Proceedings of the Thirteenth Extractive Industry Geology Conference, The University of Leeds, 2004.

[3] Sharma, P. D. (2009): Electronic detonators – Results in substantial techno-economic benefits for large mining operations, Mining Engineers Journal, India, February 2009. http://miningandblasting.wordpress.com/

[4] MIST (2006): Full Scale Quarry Blasting Project into the use of Electronic Detonators to Control Vibration from Blasting, Final report MA/4/2/003, University of Leeds, Department of Mining, Quarry and Mineral Engineering, p. 109.

[5] Company DynoNobel, http:// www.dynonobel.com/

[6] Mohanty, B., Wong, H. Y. (2004): Prediction Delay Detonators: A Decade of Progress, Department of Civil Engineering, University of Toronto. http://www.scribd.com/doc/24721763/Education-Drilling-Blasting-Docs122.

[7] Yuill, G., Farnfield, R. A. (2001): Variations in Vibration Signals from Single Hole Quarry Blasts,

Proceedings of the 27th Annual Symposium of Explosives and Blasting Technique, International Society of Explosives Engineers, Cleveland, Ohio, USA, pp. 309–317.

[8] WHITAKER, K., CHIAPPETTA, F. R. & STUMP, B. (2001): Effects of VOD, Explosive Column Length and Type of Explosive on Ground Vibration Characteristics Over Distance, Proc. BAI 10th High-Tech Seminar on state of art blasting technology, instrumentation and explosives, Nashville, Tennessee, USA, pp. u3–u66.

[9] WATSON, J. T. (2000): Developments with Electronic Detonators. http://www.dynonobel.com/NR/rdonlyres/A0AB000B-AA62-4E2E-9891-815BA2BACA1C/0/ElectronicDetonators.pdf

[10] REAMER, S. K., HINZER, K. G., & SIFRE, Y. (1993): Case Studies in The Application of Firing Time Optimisation, Proceedings of the Nineteenth Annual Conference of Explosives and BlastingTechniques, San Diego, Los Angles, 1993 International Society of Explosives Engineers, pp. 281–293.

[11] SYED, T. T. (): Comparative Study of Calculated and Measured Particle Velocities, Pakistan Engineering Congress, 69th Annual Session Proceedings, pp. 425–433.

Analysis of the failured pinion from the drive of a cement mill

Analiza poškodovanega pastorka iz pogona mlina za cement

Borut Kosec[1,*], Gorazd Kosec[2], Igor Budak[3], Aleš Nagode[1], Aco Antić[3]

[1]University of Ljubljana, Faculty of Natural Sciences and Engineering, Aškerčeva c. 12, 1000 Ljubljana, Slovenia
[2]ACRONI, C. B. Kidriča 44, 4270 Jesenice, Slovenia
[3]University of Novi Sad, Faculty of Technical Sciences, Trg D. Obradovića 6, 21000 Novi Sad, Serbia

*Corresponding author. E-mail: borut.kosec@omm.ntf.uni-lj.si

Received: July 2, 2010 **Accepted:** September 8, 2010

Abstract: The pinion from the drive of the cement mill was failure. The teeth ruptured and peeling occurred on the sides of some teeth. The failure was only located on one side of the pinion. This type of failure is common with surface-hardened gears.
We have found that the failure of the pinion is a direct consequence of the incorrect geometry of the surface hardened layer. The lifespan of the pinion could have been extended if the whole surface of the faces and roots of the teeth had been hardened and if the hardening had been deeper.

Povzetek: Na pastorku iz pogona mlina za cement so nastale poškodbe v obliki prelomov in luščenja na bokih nekaterih zob. Poškodbe so bile locirane le na eni strani pastorka. V okviru izvedene analize smo ugotovili, da so poškodbe pastorka posledica neustrezne geometrije površinsko kaljene plasti. Trajnostno dobo pastorka bi zanesljivo podaljšali, če bi bili boki in koreni zob kaljeni v celoti in če bi bila površina globlje kaljena.

Key words: cement mill, pinion, failure analysis, surface hardening
Ključne besede: mlin za cement, pogonski zobnik, analiza poškodb, površinsko kaljenje

Professional Paper

Introduction

In our work we describe a relatively common example of the rupture of gear teeth of a relatively large module of large dimensions that - built into reduction gears of large machinery and devices in process industries (e.g. cement mill) - also endures large loads, forces and torques.[1, 2]

When manufacturing gears for large modules, wear of the gear teeth faces is often prevented by surface hardening. [3, 4] Little attention is usually paid to the resistance of gears against fatigue. When it comes to gear fatigue, the division, signs and amount of internal stresses acquired specifically through surface hardening are very important. The incorrect geometry of the hardened surface is the cause of improper internal stress distribution and inadequate structural strength.[5]

With gears, the hardened surface area of the teeth faces often ends near the root of the teeth. Consequently, this hardened area is where positive (tensile) internal stresses occur. This is normally also the area of the largest changes of external tensile (positive) stresses. The superposition of positive stresses from both sources, in connection with additional eventual geometric stress concentrators, contributes to the formation and spread of fatigue cracks. However, since the gears frequently rotate in both directions, cracks appear in both roots of a tooth, of which one crack is usually longer.

The failure of the pinion of the cement mill drive (No. 354881, teeth 28, module 36, diameter 1640 mm, width 1800 mm) occurred in the form of fatigue cracks and the peeling of steel on the faces of several teeth. The failure was only located on one side of the pinion (Figure 1). The teeth breakage began with ruptures, which typically started at the roots of the teeth faces and spread outwards. The breakage resulted in transverse ruptures along the height of the teeth.

The other failure that occurred was the peeling of the steel on the faces of the teeth. Such failure is caused by excessive Hertzian pressure applied to the faces, or is a consequence of the lack of compressive strength of the steel at a critical depth of the teeth surface. In this way, the unbroken teeth are also failured, but the extent of this type of damage was significantly smaller in our case.

Failure analysis

Visible lines formed on both side faces of the individual teeth and their roots. They are a consequence of the thermal effects of surface hardening.[6] These lines were wider and more distinctive

Figure 1. Failure of the pinion: part of the broken off tooth, and the peeling of steel on the faces of the teeth

Figure 2. A broken tooth and two unbroken teeth with a fatigue crack (left). Two failured teeth: the lines indicating the heated surface (right).

Table 1. Chemical composition of steel pinion [12]

Element	C	Si	Mn	P	S	Cr	Mo	Ni
(mass fraction, *w*/%)	0.40	0.34	0.69	0.01	0.03	1.16	0.27	0.28

at the undamaged side of the gear.[7, 8] The hardened areas were along the faces and at the roots (Figure 2), and were interrupted at the top of the teeth.

The teeth faces on the failured side were macroscopically etched.[9] This revealed the surface hardened layer, the macroscopic average thickness of

which is approximately 1 mm, which generally starts at the top of the tooth and ends approximately 10 mm above its root. The macroscopic profile of the teeth's surface hardened layer is not satisfactory. It has two disadvantages: it only covers a part of the teeth faces, and it is very thin. The entire surface of the faces and roots should have been hardened; it is not necessary to harden the surface at the top of the teeth. The macroscopic characteristics of the surface areas of the ruptures show that the ruptures are a consequence of the fatigue of the steel.[10, 11]

The chemical composition of the steel of the pinion is shown in Table 1. According to its chemical composition, the steel of the pinion corresponds to the high-strength steel used for improving VCMo140 of the Slovene steel manufacturer Metal Ravne.[12]

The microstructure of the pinion steel reveals that the pinion was previously strengthened and its surface was hardened (Figure 3).

The microstructure of the steel at the core of the tooth consists of tempered bainite and ferrite. On the faces of the teeth, where the steel surface is hardened, the microstructure consists of martensite (Figure 4). The martensitic microstructure of the hardened surface transforms through a binary microstructure consisting of martensite and areas of tempered bainite and ferrite into the microstructure of the core. The hardened surfaces and the area of transition to the core have a normal microstructure.

The constant hardness (approximately 650 HV) is characteristic of the hardened surface of the pinion, and gradually decreases over a transition zone to the hardness at the tooth core (approximately 275 HV) (Figure 5).

Cause of failure

The initial teeth ruptures started at the point of transition from the faces to the roots of the teeth. There, the changing loads are large enough to initiate the start and spread of fatigue cracks. A contributing factor is the relatively low strength (tangential stress) of the steel in the area (approximately the same hardness and strength as at the core of the teeth), and internal stresses that are – due to the incorrect geometry of the hardened surface – unfavourable in the area (positive, tensile) and increase the overall level of stress applied.[13]

In the hardened surface there are typically internal tangential stresses, and in its proximity also tensile stresses. This generally has a beneficial effect on the sustained dynamic strength, or fatigue resistance. For the given example,

we can only estimate that the internal stresses in the area where the fatigue cracks first appeared were positive, and that they were unfavourably added to the external, operating stress.

The geometry of the hardened surface does not contribute to the improvement of the permanent dynamic strength of the teeth, but rather diminishes it. The correct geometry of the hardened surface is such that the whole area at the faces and roots of the teeth is hardened (without discontinuities). The areas of the heated surface at the faces of the pinion teeth

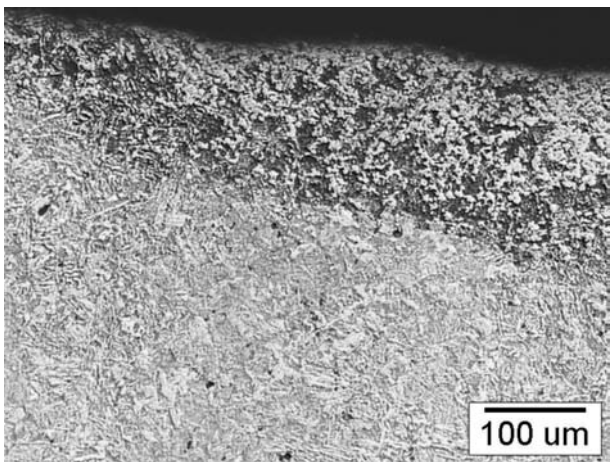

Figure 3. The area where the hardened surface of the tooth ends (OM)

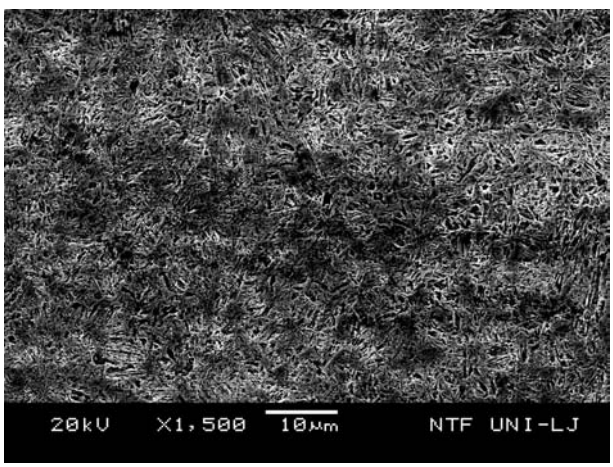

Figure 4. Microstructure of the steel at the hardened surface: martensite (SEM)

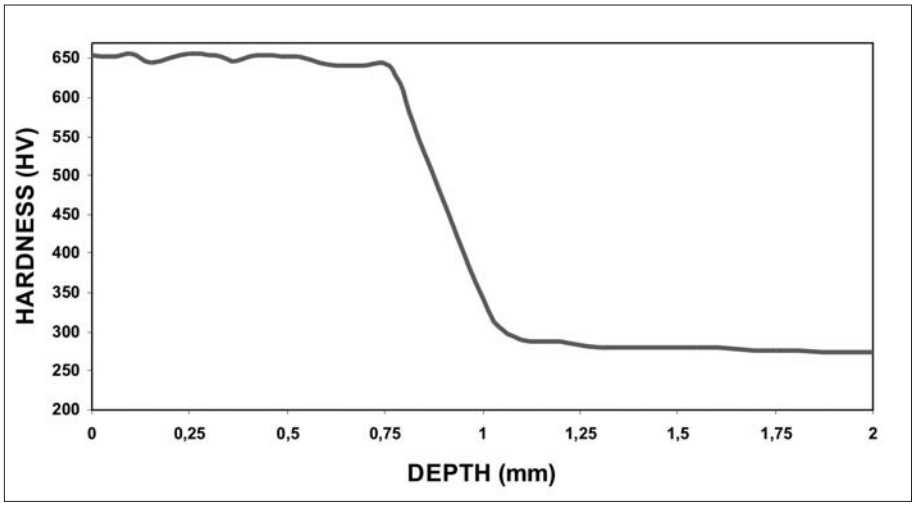

Figure 5. Microhardness in the hardened surface and transition to the core

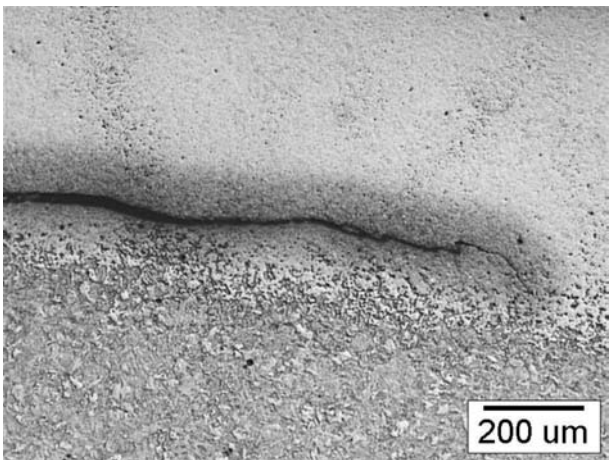

Figure 6. Crack at the point of transition from the hardened surface to the core (OM)

show that the planner and performer of the surface hardening knew this fact, but failed to strengthen the gear teeth correctly. The incorrect geometry of the hardened surface is the cause of fatigue breakage of the pinion's teeth.

The peeling of the steel on the teeth faces is a consequence of excessive Hertzian pressures, which exceed the compressive strength of the steel. The critical area where the cracks and peeling first occurred is at the point of transition between the hardened surface

(martensite) and the core of the tooth, where the mechanical properties of steel (strength) begin to decrease rapidly (Figure 6).

Conclusions

The failure of the pinion (fatigue ruptures of the teeth and the peeling of steel on the faces of the teeth) are a consequence of the incorrect geometry of the surface hardened layer.

The teeth broke off due to fatigue. The ruptures first appeared at the bottom part of the faces at the root and spread outwards, while the breakage resulted in a cross-break along the height of the teeth. The other failure that occurred was the peeling of the steel at the faces of the teeth. Thus, in addition to the ruptured teeth, the remaining teeth were also failured. However, the extent of these failure was smaller. We could therefore extend the lifespan of the pinion if the entire faces and roots of the teeth were hardened, and if the surface hardening was deeper.

Acknowledgement

The authors want to thank Prof. Ladislav Kosec and Mrs. Nika Breskvar (University of Ljubljana) for informations, instructions at SEM and OM analysis, and Prof. Mirko Soković (University of Ljubljana) for technical informations and discussions.

References

[1] V. Rudnev, D. Leveless, R. Cook, M. Black: Induction Hardening of gears: a Review, Heat Treatment of Metals, Vol. 4, 97–103, 2003.

[2] B. Kosec, M. Brezigar, G. Kosec, J. Bernetič, M. Bizjak: Heat Treatment of Cold Formed Steel Forgings for the Automotive Industry, Journal of Achievements in Materials and Manufacturing Engineering, Vol. 22, No. 2, 87–90, 2007.

[3] C. R. Brooks: The Metallurgy of Induction Surface Hardening Advanced Materials & Processes, Vol. 5, No. 12, 19–23, 2000.

[4] V. Rudnev: Handbook of Induction Heating, Marcel Dekker, New York - Basel, 2003.

[5] K. H. Decker: Maschinenelemente, Carl Hanser Verlag, Muenchen, 1975. (in German)

[6] G. E. Totten, M. A. H. Howes: Steel Heat Treatment, Marcel Dekker, New York, 1997.

[7] V. Rudnev, D. Leveless, K. Schweigert, E. Rylicki, M. Rugg: Achieving Uniform Temperature through Induction Heating, Metallurgia, Vol. 62, No. 2, 11–12, 2000.

[8] B. Kosec, G. Kosec, M. Soković: Temperature field and failure analysis of die-casting die, Archives in Materials Science and Engineering, Vol. 28, No. 3, 182–187, 2007.

[9] B. Kosec, G. Kovačič, L. Kosec:

Fatigue Cracking of an Aircraft Wheel, Engineering Failure Analysis, Vol. 9, No. 5, 603–609, 2002.

[10] L. C. F. Cannale, R. A. Mesquita, and G. E. Totten: Failure Analysis of Heat Treated Steel Components, ASM International, Materials Park, Ohio, 2008.

[11] Allianz Handbook of Loss Prevention. Allianz Versicherungs AG, Berlin, 1987.

[12] B. Jocić: Steels and Cast Irons, BIOTOP, Dobja vas, 2008.

[13] B. Kosec, L. Kosec, F. Bizjan, P. Škraba: Damage of a Screw in the Seal Coupling. Practical Failure Analysis. Vol. 2, No. 5, 57–60, 2002.

Deveti mednarodni simpozij hrvaškega metalurškega društva SHMD' 2010

Od 20. do 24. junija 2010 se je v idiličnem počitniškem hotelskem naselju Solaris v neposredni bližini dalmatinskega turističnega bisera mesta Šibenika pod delovnim naslovom "Materiali in metalurgija", odvijal že tradicionalni 9. mednarodni simpozij hrvaškega metalurškega društva, kratko SHMD '2010.

Tematika simpozija je obsegala že v njegovem delovnem naslovu navedeni področji materialov in metalurgije. Poseben poudarek pa je bil na eni strani na novih materialih, njihovemu razvoju in aplikaciji ter raziskavah, razvoju in predvsem aplikacijah na področju tradicionalnih kovinskih materialov jekla in aluminija. Pomembni sklopi so bila tudi področja livarstva, fizikalne in procesne metalurgije, plastične predelave kovin in zlitin, področje zagotavljanja kakovosti ter danes izredno aktualni področji energetike in ekologije.

Glavni organizator posvetovanja je bilo Hrvaško metalurško društvo (HMD), glavni pokrovitelji pa Ministrstvo za znanost, izobraževanje in šport RH, Gospodarska zbornica RH in Sisačko-Moslovačka županija ter ESIC (European Steel Institute Confederation) in ESF (European Steel Federation).

Akademik prof. dr. Ilija Mamuzić, predsednik HMD, glavni in odgovorni urednik revije Metalurgija ter predsedujoči SHMD '2010, med˝slovesnostjo odprtja.

Udeleženci slavnostne akademije Hrvatskega metalurškaga društva

Short Paper

Kot soorganizatorji in sponzorji posvetovanja so se tudi letos, tako kot tudi že v preteklih letih, izkazale številne univerze in inštituti, strokovna združenja in industrijski partnerji tako iz Hrvaške, Slovenije ter držav s področja nekdanje skupne države kot tudi iz držav članic Evropske unije, Rusije, Ukrajine in drugih držav bivše Sovjetske zveze, iz Južne in Severne Amerike, Azije in Afrike, katerih skupno število je letos doseglo 46. Poleg aktivnega sodelovanja slovenskih institucij znanja: Naravoslovnotehniške fakultete in Fakultete za strojništvo Univerze v Ljubljani ter Instituta za kovinske materiale in tehnologije, je treba poudariti medijsko prisotnost slovenskih revij RMZ – Materials and Geoenvironment in IRT 3000.

Letošnji simpozij je bil posvečen 150-letnici ustanovitve nemškega Stahlinstituta VDEh, 90-letnici Univerze v Dnepropetrovsku, 70-letnici študija metalurgije na Univerzi v Ljubljani, 60-letnici ustanovitve Metalurškega inštituta v Ljubljani, 55-letnici Instituta za materiale Slovaške akademije znanosti v Košicah ter 20-letnici intenzivnega mednarodnega sodelovanja Hrvaškega metalurškega društva. Pred kratkim praznovani sedemdeseti rojstni dan akademika profesorja Ilije Mamuzića, duše društva in revije Metalurgija ter članu uredniškega odbora naše revije, je dal letošnjemu srečanju še dodatno slavnostno podobo.

V okviru simpozija je bilo predstavljenih osem plenarnih predavanj in v okviru štirih tematskih sekcij več kot 500 posterskih predstavitev. Pod vodstvom akademika prof. dr. Ilije Mamuzića, glavnega in odgovornega urednika revije Metalurgija in predsednika Hrvatskega metalurškega društva (HMD), sta potekala tudi sestanek uredniškega odbora revije ter slavnostna akademija HMD.

Več informacij o posvetovanju, o društvu HMD in reviji Metalurgija, ki je v lanskem letu dosegla tudi že zavidljiv faktor vpliva 0,439, lahko najdete na spletni strani: http://public.carnet.hr/metalurg).

Borut Kosec, Peter Fajfar
foto: Studio Jakov Skugor

Author`s Index, Vol. 57, No. 3

Antić Aco	
Barbič Rok	
Bratun Julijan	julijan.bratun@e-cono.si
Budak Igor	
Čekada Miha	miha.cekada@ijs.si
Fajfar Peter	peter.fajfar@omm.ntf.uni-lj.si
Klančnik Grega	grega.klancnik@omm.ntf.uni-lj.si
Kortnik Jože	joze.kortnik@ntf.uni-lj.si
Kosec Borut	borut.kosec@omm.ntf.uni-lj.si
Kosec Gorazd	
Kozamernik Mitja	
Kramar Sabina	sabina.kramar@rescen.si
Kumar Bhism	
Likar Jakob	jakob.likar@ntf.uni-lj.si
Medved Jožef	jozef.medved@ntf.uni-lj.si
Mirtič Breda	breda.mirtic@guest.arnes.si
Mladenović Ana	
Mrvar Primož	primoz.mrvar@ntf.uni-lj.si
Nagode Aleš	
Okunlola, O. A.	gbengaokunlola@yahoo.co.uk
Olarewaju, V. O.	
Olorunfemi, A. O.	
Panjan Matjaž	matjaz.panjan@ijs.si
Panjan Peter	peter.panjan@ijs.si
Purandara B. K .	
Smolej Anton	anton.smolej@ntf.uni-lj.si
Vončina Maja	maja.voncina@ntf.uni-lj.si
Varadarajan N.	nvarad@yahoo.com

INSTRUCTIONS TO AUTHORS

RMZ-MATERIALS & GEOENVIRONMENT (RMZ- Materiali in geookolje) is a periodical publication with four issues per year (established 1952 and renamed to RMZ-M&G in 1998). The main topics of contents are Mining and Geotechnology, Metallurgy and Materials, Geology and Geoenvironment.

RMZ-M&G publishes original Scientific articles, Review papers, Preliminary notes, Professional papers **in English**. In addition, evaluations of other publications (books, monographs,...), In memoriam, Professional remarks and reviews are welcome. The Title, Abstract and Key words in Slovene will be included by the author(s) or will be provided by the referee or the Editorial Office.

**** Additional information and remarks for Slovenian authors:***
Only Professional papers, Publications notes, Events notes, Discussion of papers and In memoriam, will be exceptionally published in the Slovenian language.

Authorship and originality of the contributions. Authors are responsible for originality of presented data, ideas and conclusions as well as for correct citation of data adopted from other sources. The publication in RMZ-M&G obligate authors that the article will not be published anywhere else in the same form.

Specification of Contributions

RMZ-M&G will publish papers of the following categories:

Full papers (optimal number of pages is 7 to 15, longer articles should be discussed with Editor prior to submission). An abstract is required.

- **Original scientific papers** represent unpublished results of original research.
- **Review papers** summarize previously published scientific, research and/or expertise articles on the new scientific level and can contain also other cited sources, which are not mainly result of author(s).

- **Preliminary notes** represent preliminary research findings, which should be published rapidly.
- **Professional paper**s are the result of technological research achievements, application research results and information about achievements in practice and industry.

Short papers (the number of pages is limited to 1 for Discussion of papers and 2 pages for Publication note, Event note and In Memoriam). No abstract is required for short papers.

- **Publication notes** contain author's opinion on new published books, monographs, textbooks, or other published material. A figure of cover page is expected.
- **Event notes** in which descriptions of a scientific or professional event are given.
- **Discussion of papers (Comments)** where only professional disagreements can be discussed. Normally the source author(s) reply the remarks in the same issue.
- **In memoriam** (a photo is expected).

Supervision and review of manuscripts. All manuscripts will be supervised. The referees evaluate manuscripts and can ask authors to change particular segments, and propose to the Editor the acceptability of submitted articles. Authors can suggest the referee but Editor has a right to choose another. **The name of the referee remains anonymous.** The technical corrections will be done too and authors can be asked to correct missing items. The final decision whether the manuscript will be published is made by the Editor in Chief.

The Form of the Manuscript

The manuscript should be submitted as a complete hard copy including figures and tables. The figures should also be enclosed separately, both charts and photos in the original version. In addition, all material should also be provided in electronic form on a diskette or a CD. The necessary information can conveniently also be delivered by E-mail.

Composition of manuscript is defined in the attached Template

The original file of Template is available on RMZ-Materials and Geoenvironment Home page address:

http://www.rmz-mg.com

References - can be arranged in two ways:
- first possibility: alphabetic arrangement of first authors - in text: (Borgne, 1955), or
- second possibility: [1] numerated in the same order as cited in the text: example[1]

Format of papers in journals:

LE BORGNE, E. (1955): Susceptibilite magnetic anomale du sol superficiel. *Annales de Geophysique*, 11, pp. 399–419.

Format of books:

ROBERTS, J. L. (1989): Geological structures, *MacMillan*, *London*, 250 p.

Text on the hard print copy can be prepared with any text-processor. The electronic version on the diskette, CD or E-mail transfer should be in MS Word or ASCII format.
Captions of figures and tables should be enclosed separately.
Figures (graphs and photos) and tables should be original and sent separately in addition to text. They can be prepared on paper or computer designed (MSExcel, Corel, Acad).
Format. Electronic figures are recommended to be in CDR, Al, EPS, TIF or JPG formats. Resolution of bitmap graphics (TIF, JPG) should be at least 300 dpi. Text in vector graphics (CDR, Al, EPS) must be in MSWord Times typography or converted in curves.
Color prints. Authors will be charged for color prints of figures and photos.
Labeling of the additionally provided material for the manuscript should be very clear and must contain at least the lead author's name, address, the beginning of the title and the date of delivery of the manuscript. In case of an E-mail transfer the exact message with above asked data must accompany the attachment with the file containing the manuscript.

Information about RMZ-M&G:
Editor in Chief prof. dr. Peter Fajfar (phone: ++386 1 4250-316) or
Secretary Barbara Bohar Bobnar, univ. dipl. ing. geol. (phone: ++386 1 4704-630),
Aškerčeva 12, 1000 Ljubljana, Slovenia
or at E-mail addresses:
peter.fajfar@ntf.uni-lj.si,
barbara.bohar@ntf.uni-lj.si

Sending of manuscripts. Manuscripts can be sent by mail to the **Editorial Office** address:

- RMZ-Materials & Geoenvironment
  Aškerčeva 12,
  1000 Ljubljana, Slovenia

or delivered to:

- **Reception** of the Faculty of Natural Science and Engineering (for RMZ-M&G)
  Aškerčeva 12,
  1000 Ljubljana, Slovenia
- E-mail - addresses of Editor and Secretary
- You can also contact them on their phone numbers.

These instructions are valid from August 2009

NAVODILA AVTORJEM

RMZ-MATERIALS AND GEOENVIRONMENT (RMZ- Materiali in geookolje) – kratica RMZ-M&G - je revija (ustanovljena kot zbornik 1952 in preimenovana v revijo RMZ-M&G 1998), ki izhaja vsako leto v štirih zvezkih. V reviji objavljamo prispevke s področja rudarstva, geotehnologije, materialov, metalurgije, geologije in geookolja.

RMZ- M&G objavlja izvirne znanstvene, pregledne in strokovne članke ter predhodne objave samo v angleškem jeziku. Strokovni članki so lahko izjemoma napisani v slovenskem jeziku. Kot dodatek so zaželene recenzije drugih publikacij (knjig, monografij …), nekrologi In Memoriam, predstavitve znanstvenih in strokovnih dogodkov, kratke objave in strokovne replike na članke objavljene v RMZ-M&G v slovenskem ali angleškem jeziku. Prispevki naj bodo kratki in jasni.

Avtorstvo in izvirnost prispevkov. Avtorji so odgovorni za izvirnost podatkov, idej in sklepov v predloženem prispevku oziroma za pravilno citiranje privzetih podatkov. Z objavo v RMZ-M&G se tudi obvežejo, da ne bodo nikjer drugje objavili enakega prispevka.

Vrste prispevkov

Optimalno število strani je 7 do 15, za daljše članke je potrebno soglasje glavnega urednika.

Izvirni znanstveni članki opisujejo še neobjavljene rezultate lastnih raziskav.

Pregledni članki povzemajo že objavljene znanstvene, raziskovalne ali strokovne dosežke na novem znanstvenem nivoju in lahko vsebujejo tudi druge (citirane) vire, ki niso večinsko rezultat dela avtorjev.

Predhodna objava povzema izsledke raziskave, ki je v teku in zahteva hitro objavo.

Strokovni članki vsebujejo rezultate tehnoloških dosežkov, razvojnih projektov in druge informacije iz prakse.

Recenzije publikacij zajemajo ocene novih knjig, monografij, učbenikov, razstav …(do dve strani; zaželena slika naslovnice in kratka navedba osnovnih podatkov - izkaznica).

In memoriam (do dve strani, zaželena slika).
Strokovne pripombe na objavljene članke ne smejo presegati ene strani in opozarjajo izključno na strokovne nedoslednosti objavljenih člankov v prejšnjih številkah RMZ-M&G. Praviloma že v isti številki avtorji prvotnega članka napišejo odgovor na pripombe.
Poljudni članki, ki povzemajo znanstvene in strokovne dogodke (do dve strani).

Recenzije. Vsi prispevki bodo predloženi v recenzijo. Recenzent oceni primernost prispevka za objavo in lahko predlaga kot pogoj za objavo dopolnilo k prispevku. Recenzenta izbere Uredništvo med strokovnjaki, ki so dejavni na sorodnih področjih, kot jih obravnava prispevek. Avtorji lahko sami predlagajo recenzenta, vendar si uredništvo pridržuje pravico, da izbere drugega recenzenta. **Recenzent ostane anonimen**. Prispevki bodo tudi tehnično ocenjeni in avtorji so dolžni popraviti pomanjkljivosti. Končno odločitev za objavo da glavni in odgovorni urednik.

Oblika prispevka

Prispevek predložite v tiskanem oštevilčenem izvodu (po možnosti z vključenimi slikami in tabelami) ter na disketi ali CD, lahko pa ga pošljete tudi prek E-maila. Slike in grafe je možno poslati tudi risane na papirju, fotografije naj bodo originalne.

Razčlenitev prispevka:

Predloga za pisanje članka se nahaja na spletni strani:

http://www.rmz-mg.com/predloga.htm

Seznam literature je lahko urejen na dva načina:
-po abecednem zaporedju prvih avtorjev ali
-po [1]vrstnem zaporedju citiranosti v prispevku.

Oblika je za oba načina enaka:
Članki:

> Le Borgne, E. (1955): Susceptibilite magnetic anomale du sol superficiel. *Annales de Geophysique*; Vol. 11, pp. 399–419.

Knjige:

ROBERTS, J. L. (1989): Geological structures, *MacMillan*, *London*, 250 p.

Tekst izpisanega izvoda je lahko pripravljen v kateremkoli urejevalniku. Na disketi, CD ali v elektronskem prenosu pa mora biti v MS Word ali v ASCII obliki.

Naslovi slik in tabel naj bodo priloženi posebej. Naslove slik, tabel in celotno besedilo, ki se pojavlja na slikah in tabelah, je potrebno navesti v angleškem in slovenskem jeziku.

Slike (ilustracije in fotografije) in tabele morajo biti izvirne in priložene posebej. Njihov položaj v besedilu mora biti jasen iz priloženega kompletnega izvoda. Narejene so lahko na papirju ali pa v računalniški obliki (MS Excel, Corel, Acad).

Format elektronskih slik naj bo v EPS, TIF ali JPG obliki z ločljivostjo okrog 300 dpi. Tekst v grafiki naj bo v Times tipografiji.

Barvne slike. Objavo barvnih slik sofinancirajo avtorji

Označenost poslanega materiala. Izpisan izvod, disketa ali CD morajo biti jasno označeni – vsaj z imenom prvega avtorja, začetkom naslova in datumom izročitve uredništvu RMZ-M&G. Elektronski prenos mora biti pospremljen z jasnim sporočilom in z enakimi podatki kot velja za ostale načine posredovanja.

Informacije o RMZ-M&G: urednik prof. dr. Peter Fajfar, univ. dipl. ing. metal. (tel. ++386 1 4250316) ali tajnica Barbara Bohar Bobnar, univ. dipl. ing. geol. (tel. ++386 1 4704630), Aškerčeva 12, 1000 Ljubljana
ali na E-mail naslovih:
peter.fajfar@ntf.uni-lj.si
barbara.bohar@ntf.uni-lj.si

Pošiljanje prispevkov. Prispevke pošljite priporočeno na naslov **Uredništva:**

- RMZ-Materials and Geoenvironment
  Aškerčeva 12,
  1000 Ljubljana, Slovenija

oziroma jih oddajte v

- **Recepciji** Naravoslovnotehniške fakultete (pritličje) (za RMZ-M&G)
  Aškerčeva 12,
  1000 Ljubljana, Slovenija
- Možna je tudi oddaja pri uredniku oziroma pri tajnici.

Navodila veljajo od avgusta 2009.

TEMPLATE

The title of the manuscript should be written in bold letters (Times New Roman, 14, Center)

Naslov članka (Times New Roman, 14, Center)

Name Surname[1], …. , & Name Surname[X] (Times New Roman, 12, Center)

[x] University of ..., Faculty of ..., Address…, Country ... (Times New Roman, 11, Center)

*Corresponding author. E-mail: ... (Times New Roman, 11, Center)

Abstract (Times New Roman, Normal, 11): The abstract should be concise and should present the aim of the work, essential results and conclusion. It should be typed in font size 11, single-spaced. Except for the first line, the text should be indented from the left margin by 10 mm. The length should not exceed fifteen (15) lines (10 are recommended).

Izvleček (Times New Roman, navadno, 11): Kratek izvleček namena članka ter ključnih rezultatov in ugotovitev. Razen prve vrstice naj bo tekst zamaknjen z levega roba za 10 mm. Dolžina naj ne presega petnajst (15) vrstic (10 je priporočeno).

Key words: a list of up to 5 key words (3 to 5) that will be useful for indexing or searching. Use the same styling as for abstract.
Ključne besede: seznam največ 5 ključnih besed (3–5) za pomoč pri indeksiranju ali iskanju. Uporabite enako obliko kot za izvleček.

Introduction (Times New Roman, Bold, 12)

Two lines below the keywords begin the introduction. Use Times New Roman, font size 12, Justify alignment.

There are two (2) admissible methods of citing references in text:

1. by stating the first author and the year of publication of the reference in the parenthesis at the appropriate place in the text and arranging the reference list in the alphabetic order of first authors; e.g.:
   "Detailed information about geohistorical development of this zone can be found in: Antonijević (1957), Grubić (1962), ..."
   "… the method was described previously (Hoefs, 1996)"
2. by consecutive Arabic numerals in square brackets, superscripted at the appropriate place in the text and arranging the reference list at the end of the text in the like manner; e.g.:
   "... while the portal was made in Zope environment. [3]"

Materials and methods (Times New Roman, Bold, 12)

This section describes the available data and procedure of work and therefore provides enough information to allow the interpretation of the results, obtained by the used methods.

Results and discussion (Times New Roman, Bold, 12)

Tables, figures, pictures, and schemes should be incorporated in the text at the appropriate place and should fit on one page. Break larger schemes and tables into smaller parts to prevent extending over more than one page.

Conclusions (Times New Roman, Bold, 12)

This paragraph summarizes the results and draws conclusions.

Acknowledgements (Times New Roman, Bold, 12, Center - optional)

This work was supported by the ****.

References (Times New Roman, Bold, 12)

In regard to the method used in the text, the styling, punctuation and capitalization should conform to the following:

FIRST OPTION - in alphabetical order

Casati, P., Jadoul, F., Nicora, A., Marinelli, M., Fantini-Sestini, N. & Fois, E. (1981): Geologia della Valle del'Anisici e dei gruppi M. Popera - Tre Cime di Lavaredo (Dolomiti Orientali). *Riv. Ital. Paleont.*; Vol. 87, No. 3, pp. 391–400, Milano.

Folk, R. L. (1959): Practical petrographic classification of limestones. *Amer. Ass. Petrol. Geol. Bull.;* Vol. 43, No. 1, pp. 1–38, Tulsa.

SECOND OPTION - in numerical order

[1] Trček, B. (2001): *Solute transport monitoring in the unsaturated zone of the karst aquifer by natural tracers.* Ph. D. Thesis. Ljubljana: University of Ljubljana 2001; 125 p.

[2] Higashitani, K., Iseri, H., Okuhara, K., Hatade, S. (1995): Magnetic Effects on Zeta Potential and Diffusivity of Nonmagnetic Particles. *Journal of Colloid and Interface Science, 172*, pp. 383–388.

Citing the Internet site:

CASREACT-Chemical reactions database [online]. Chemical Abstracts Service, 2000, updated 2. 2. 2000 [cited 3. 2. 2000]. Accessible on Internet: http://www.cas.org/CASFILES/casreact.html.

Texts in Slovene (title, abstract and key words) can be written by the author(s) or will be provided by the referee or by the Editorial Board.

PREDLOGA ZA SLOVENSKE ČLANKE

Naslov članka (Times New Roman, 14, Na sredino)

The title of the manuscript should be written in bold letters (Times New Roman, 14, Center)

Ime Priimek[1], …, Ime Priimek[X] (Times New Roman, 12, Na sredino)

[X]Univerza…, Fakulteta…, Naslov…, Država… (Times New Roman, 11, Center)

*Korespondenčni avtor. E-mail: ... (Times New Roman, 11, Center)

Izvleček (Times New Roman, Navadno, 11): Kratek izvleček namena članka ter ključnih rezultatov in ugotovitev. Razen prve j bo tekst zamaknjen z levega roba za 10 mm. Dolžina naj ne presega petnajst (15) vrstic (10 je priporočeno).

Abstract (Times New Roman, Normal, 11): The abstract should be concise and should present the aim of the work, essential results and conclusion. It should be typed in font size 11, single-spaced. Except for the first line, the text should be indented from the left margin by 10 mm. The length should not exceed fifteen (15) lines (10 are recommended).

Ključne besede: seznam največ 5 ključnih besed (3–5) za pomoč pri indeksiranju ali iskanju. Uporabite enako obliko kot za izvleček.
Key words: a list of up to 5 key words (3 to 5) that will be useful for indexing or searching. Use the same styling as for abstract.

Uvod (Times New Roman, Krepko, 12)

Dve vrstici pod ključnimi besedami se začne Uvod. Uporabite pisavo Times New Roman, velikost črk 12, z obojestransko poravnavo. Naslovi slik in tabel (vključno z besedilom v slikah) morajo biti v slovenskem jeziku.

Slika (Tabela) X. Pripadajoče besedilo k sliki (tabeli)

Obstajata dve sprejemljivi metodi navajanja referenc:

1. z navedbo prvega avtorja in letnice objave reference v oklepaju na ustreznem mestu v tekstu in z ureditvijo seznama referenc po abecednem zaporedju prvih avtorjev; npr.:

"Detailed information about geohistorical development of this zone can be found in: Antonijević (1957), Grubić (1962), ..."

"… the method was described previously (Hoefs, 1996)"

ali

2. z zaporednimi arabskimi številkami v oglatih oklepajih na ustreznem mestu v tekstu in z ureditvijo seznama referenc v številčnem zaporedju navajanja; npr.;

"... while the portal was made in Zope[3] environment."

Materiali in metode (Times New Roman, Krepko, 12)

Ta del opisuje razpoložljive podatke, metode in način dela ter omogoča zadostno količino informacij, da lahko z opisanimi metodami delo ponovimo.

Rezultati in razprava (Times New Roman, Krepko, 12)

Tabele, sheme in slike je treba vnesti (z ukazom Insert, ne Paste) v tekst na ustreznem mestu. Večje sheme in tabele je po treba ločiti na manjše dele, da ne presegajo ene strani.

Sklepi (Times New Roman, Krepko, 12)

Povzetek rezultatov in sklepi.

Zahvale (Times New Roman, Krepko, 12, Na sredino - opcija)

Izvedbo tega dela je omogočilo ……

Viri (Times New Roman, Krepko, 12)

Glede na uporabljeno metodo citiranja referenc v tekstu upoštevajte eno od naslednjih oblik:

PRVA MOŽNOST (priporočena) - v abecednem zaporedju

Casati, P., Jadoul, F., Nicora, A., Marinelli, M., Fantini-Sestini, N. & Fois, E. (1981): Geologia della Valle del'Anisici e dei gruppi M. Popera – Tre Cime di Lavaredo (Dolomiti Orientali). *Riv. Ital. Paleont.*; Vol. 87, No. 3, pp. 391–400, Milano.

Folk, R. L. (1959): Practical petrographic classification of limestones. *Amer. Ass. Petrol. Geol. Bull.;* Vol. 43, No. 1, pp. 1–38, Tulsa.

DRUGA MOŽNOST - v numeričnem zaporedju

[1] Trček, B. (2001): *Solute transport monitoring in the unsaturated zone of the karst aquifer by natural tracers.* Ph. D. Thesis. Ljubljana: University of Ljubljana 2001; 125 p.

[2] Higashitani, K., Iseri, H., Okuhara, K., Hatade, S. (1995): Magnetic Effects on Zeta Potential and Diffusivity of Nonmagnetic Particles. *Journal of Colloid and Interface Science, 172*, pp. 383–388.

Citiranje spletne strani:

CASREACT-Chemical reactions database [online]. Chemical Abstracts Service, 2000, obnovljeno 2. 2. 2000 [citirano 3. 2. 2000]. Dostopno na svetovnem spletu: http://www.cas.org/CASFILES/casreact.html.

Znanstveni, pregledni in strokovni članki ter predhodne objave se objavijo v angleškem jeziku. Izjemoma se strokovni članek objavi v slovenskem jeziku.


RTH

Univerza v Ljubljani, Naravoslovnotehniška fakulteta

Oddelek za materiale in metalurgijo

Aškerčeva cesta 12
1000 Ljubljana

Telefon: (01) 470 46 08,
E-pošta: omm@ntf.uni-lj.si

internetni naslov:
http://www.ntf.uni-lj.si/

Če se premakne, boste izvedeli prvi

Leica Geosystems rešitve za opazovanje premikov

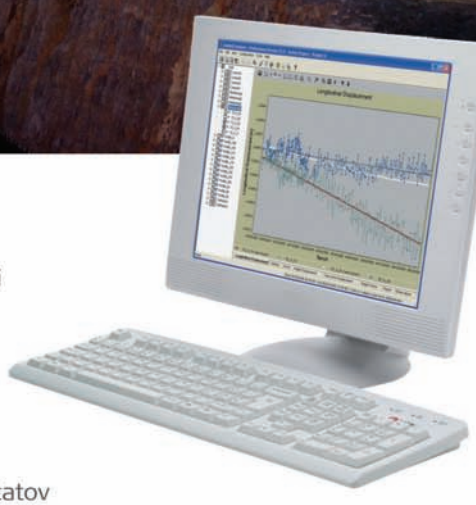

- **Geodetski senzorji**
  samodejni tahimetri, GPS in GNSS senzorji
- **Geotehnični senzorji**
  senzorji nagiba, Campbell datalogger
- **Drugi senzorji**
  meteo, senzorji nivoja
- **Programska oprema**
  za zajem in obdelavo podatkov, analizo opazovanj, alarmiranje, predstavitev rezultatov

geo servis

Geoservis, d.o.o.
Litijska cesta 45, 1000 Ljubljana
t. (01) 586 38 30, i. www.geoservis.si

■ Authorized Leica Geosystems Distributor

- when it has to be **right**

Leica Geosystems